E-665

A Study of the Q^2 Dependence of the QCD Coupling Constant from the Transverse Momentum of Jets in Deep Inelastic Muon Scattering

A thesis presented

by

Janet Marie Conrad

to

The Department of Physics

in partial fulfillment of the requirements
for the degree of
Doctor of Philosophy
in the subject of
Physics
Harvard University
Cambridge, Massachusetts

December, 1992

A Study of the Q^2 Dependence of the QCD Coupling Constant from the Transverse Momentum of Jets in Deep Inelastic Muon Scattering

A thesis presented

by

Janet Marie Conrad

to

The Department of Physics

in partial fulfillment of the requirements
for the degree of
Doctor of Philosophy
in the subject of
Physics
Harvard University
Cambridge, Massachusetts

December, 1992

Abstract

Experiment 665 at Fermilab is the first deep inelastic scattering experiment to obtain data in a kinematic range where jets can be identified on an event-by-event basis. In this thesis, using the average squared transverse momentum of the jets produced in deep inelastic muon scattering, a quantity is calculated which Perturbative QCD predicts to be equal to α_s, the strong coupling constant. The quantity is studied as a function of Q^2, the negative 4-momentum squared of the virtual photon, for $3 < Q^2 < 25\ GeV^2$. The data are shown to be consistent with the predictions of PQCD with $\Lambda_{DIS}^{n_f=4} = 359 \pm 31\ (stat) \pm 149\ (sys)\ MeV$. However this may have a significant theoretical error due to uncalculated higher order corrections. This thesis provides a detailed description of the characteristics of the identified jets. The transverse momentum due to fragmentation is measured to be $\langle P_{T\ frag}^2 \rangle = 0.0820 \pm 0.002 (stat) \pm 0.005 (sys)$. Using naive assumptions about the jets, the intrinsic transverse momentum is measured to be $\langle k_T^2 \rangle = 0.27 \pm 0.01\ (stat) \pm 0.03\ (sys)\ GeV^2$.

for my family
and
in memory of
Professor Francis M. Pipkin

Acknowledgements

I have been fortunate to work with excellent advisors and a terrific collaboration during my years as a graduate student. The E665 collaboration is large and I am indebted to many more people than I can list in these acknowledgements. I hope that all of you know that I am grateful to you.

In January 1992, my advisor, Professor Frank Pipkin, passed away. I had the privilege of working with Frank for eight years as an undergraduate and graduate student. He was my mentor and my friend. He provided many of my opportunities and gave me the intellectual freedom to pursue my interests. I am sorry to have waited until these acknowledgements to thank him.

I thank Professor Richard Wilson for becoming my acting advisor after Frank's death. I have enjoyed working with Dick and the other other members of the "Harvard Group" on E665: Doug Michael, Michael Schmitt, Ashutosh Kotwal, Guang Fang, and especially Richard Nickerson. Also the Harvard electronics shop and the physics department administrative staff have been very helpful.

On this analysis, I have worked closely with Hugh Montgomery. It was Mont who kept my train of thought on track and on time. After reading so many draft versions of this thesis, he probably has memorized it. I have appreciated his guidance.

An advantage of working at Fermilab is that there are many senior physicists who are willing to work closely with the students. I have often turned to Don Geesaman, Heidi Schellman (my almost-cousin), Steve Wolbers, Wolfgang Wittek, Helmut Braun, Andreas Manz, Clive Halliwell, Shuichi Kunori and, especially, Harry Melanson and Jorge Morfin for suggestions. Marj Corcoran and her students asked many good questions. I have had useful discussions with Dirk Graudenz and with the theorists at Fermilab and Moriond '92.

I am indebted to the fifteen Run87 graduate students for their hardware and code. I especially appreciated Doug Jansen's and Anwar Bhatti's encouragement and chocolate. Among the graduate students who saw E665 through all three running periods, I especially want to thank Rob Kennedy (and Liz and Kathy), Mark Baker (and Brenda), and Mathias Wilhelm (and Ulrike). It's been fun. I have appreciated the input of the Run90-91 students, especially Ashutosh Kotwal (who can find pearls in popcorn), Pangiotis Spentzouris, Tim Carroll and Bill Dougherty.

Doug Michael and Doug Jansen were the Orville and Wilbur Wright, and Harry Melanson was the Charles Lindburgh of our "Jet Group" on E665. This thesis could not have been written without their input. Carlos Salgado's insights were helpful. I also want to thank the other members of the group for their suggestions: Harsh Venkatramania, Don Geesaman, Heidi Schellman, and Wolfgang Wittek.

The Level II trigger was a great project for a graduate student and I thank those people who helped me: Hans Kobrak, Richard Nickerson, Vassili Papavassiliou, Mark Baker, Rob Kennedy, the other members of the Trigger Committee, Allen White, and John Oliver.

Certain people keep E665 going. Among them are John Schell (who tried so hard to train me out of all of those bad habits) and Brian Lavoy. The staff of Fermilab have been very good to E665 and to me.

I thank the American Association of University Women for their support.

Finally, I thank my friends and family. When I was really bogged down, Claire Broido reminded me that science is fun. Nancy Carrigan, Morris Binkley, Janet Mackay and the auditorium committee provided welcome diversions from the muon lab. Uncle Bill and Aunt Jean provided a haven on my trips to Cambridge. Alison McLean deserves a lot more than roses, but I can't think of how to begin to thank her. And, most importantly, thanks to: Jeanee, Jennifer, Christine, mom, daddy and $B\alpha\sigma\iota\lambda\eta$.

Contents

page.

List of Figures

List of Tables

Introduction

Quantum Chromodynamics (QCD) is the theory that describes our present understanding of the strong interactions. Along with Quantum Electrodynamics (QED) and the weak interaction model, it forms the foundation of the theory of the non-gravitational interaction of particles. However, compared to the electroweak sector, the understanding of QCD is incomplete. It has only been within the last 15 years that electron-positron and hadron colliders have reached energies where event structures predicted by QCD processes could be clearly observed. Experiment 665, on which this thesis is based, is the first deep inelastic experiment to reach such energies.

This thesis uses deep inelastic scattering to study QCD-predicted event structures, called "jets:" collimated streams of particles. The first evidence for jet structure was observed in e^+e^- production of hadrons in 1975.[1] The events, first observed at SPEAR and later DORIS, with center-of-mass energies $\sqrt{s} = 3-9\ GeV$, had two streams of hadrons in opposite directions in the center-of-mass which could be interpreted as the fragments of more fundamental particles. The first evidence for three hadron jets was observed in PETRA experiments in 1979/1980 at CMS energy $\sqrt{s} = 29\ GeV$.[2,3,4,5] An example of an event observed by the TASSO Collaboration[5] is shown in figure I.1. This was regarded as strong evidence of a QCD-predicted event structure, where, again, each jet was associated with an outgoing underlying fundamental particle. Since that time, clearly separated multi-jet structures, consistent with QCD predictions, have been observed in all types of interactions with CMS energies greater than $\sim 20\ GeV$.[6]

Experiment 665 is the first deep inelastic scattering experiment to reach CMS energies greater than 20 GeV. For the first time, well separated multijet events can be observed in deep inelastic scattering data. An example event, comparable to the type observed at PETRA, is shown in figure I.2. Some events in the E665 data also exhibit two jet events structures similar to those observed at SPEAR. The characteristics of the jets observed in the E665 data will be discussed in detail in chapter 6.

If the jets observed in the E665 data can be associated with underlying QCD events, then the data can be used to perform tests of this theory. In chapter 7, the average squared transverse momentum of the observed jets will be used to study the QCD coupling constant

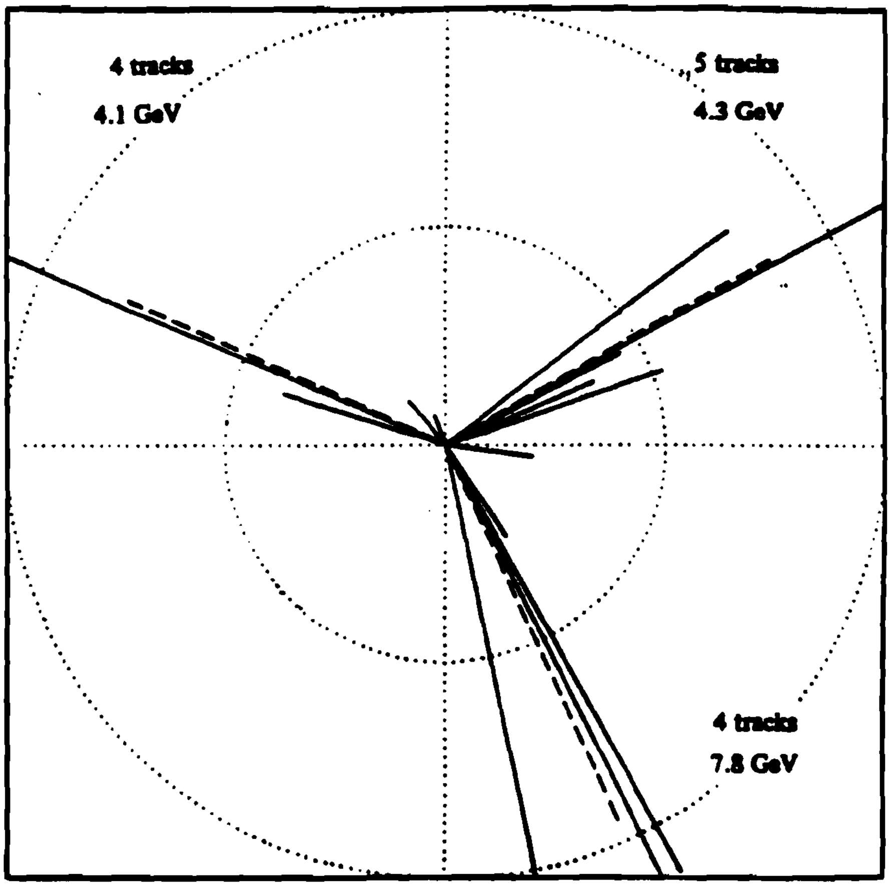

Figure I.1. A three jet event observed at PETRA, e^+e^- at $\sqrt{s} = 29\ GeV$, by the TASSO collaboration (see reference 5).

α_s. Although called a constant, α_s is predicted to vary with the energy scale in the event. This thesis will provide the first evidence for this variation within a single data set and analysis method.

This thesis uses average transverse momentum squared of jets to study the variation of the QCD coupling. Average transverse momentum squared of the jets is expected to be less sensitive to uncertainties in the acceptance correction and to nonperturbative effects than average transverse momentum squared of the individual particles, as discussed in chapter 3. Furthermore, weighting by the transverse momentum squared enhances the contributions from hard QCD events compared to the soft contributions when jets are used. Higher order corrections have been estimated to be small for certain jet algorithms, although the full calculations are not yet available. Note that if more complete calculations indicate large corrections, the conclusions from the analysis of chapter 7 will change but the measurement of the average transverse momentum squared will not.

This is only one of many methods using event topology which may be applied to study the variation of α_s in deep inelastic scattering experiments. For examples of other

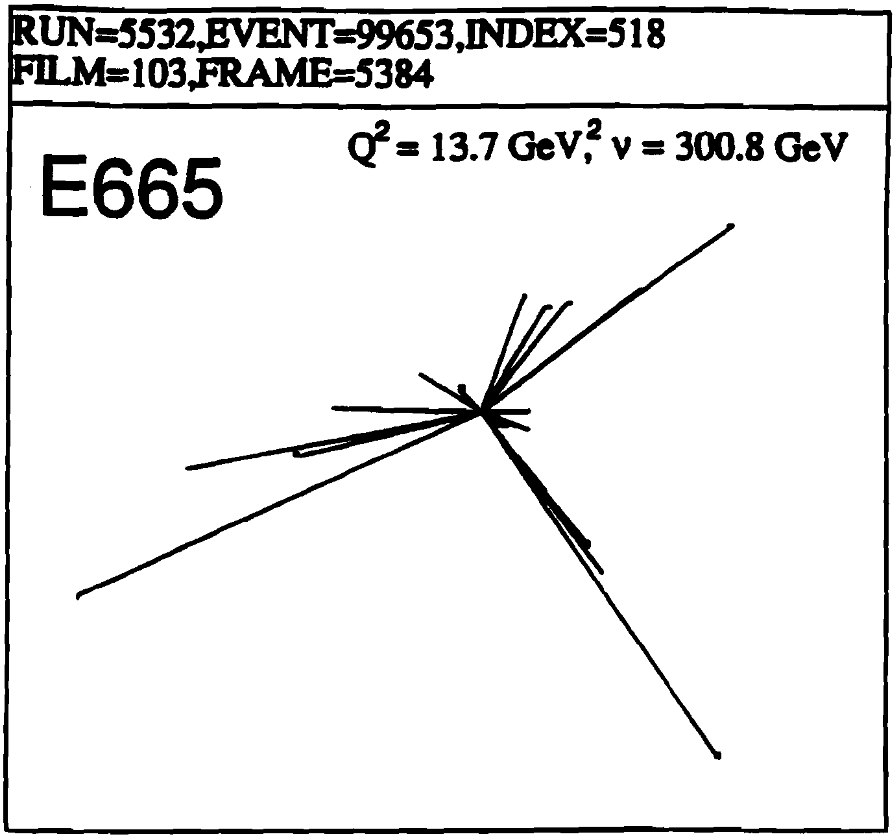

Figure I.2. Example of a three jet event from the E665 data. The display is shown in the virtual photon–proton CMS. The virtual photon–proton direction is along the horizontal axis.

techniques, see references 7 – 11. This thesis builds upon the work of previous transverse momentum analyses of individual particles[12,13,14] and the initial studies of jet production rates[10,13,15] using the E665 Run87 data.

The organization of this thesis is the following:

Chapter 1. Reviews the ideas of deep inelastic scattering, QCD and α_s.

Chapter 2. Examines the predicted average squared transverse momentum at the parton level and its relationship to α_s.

Chapter 3. Discusses the leap from partons to jets of hadrons.

Chapter 4. Introduces Experiment 665, Deep Inelastic Muon scattering at the Tevatron.

Chapter 5. Discusses the detailed characteristics of the data sets used in this analysis.

Chapter 6. Describes the characteristics of the identified jets and provides comparison to parton-level predictions.

Chapter 7. Evaluates the average squared transverse momentum and α_s as a function of momentum transfer squared.

Finally, conclusions, which summarize the measurements and compare the E665 results to those from other experiments, are presented.

Throughout this thesis, many different symbols for kinematic variables will be used. For ease of reference, a table of definitions is provided in Appendix A.

Chapter 1

Deep Inelastic Scattering and QCD

This chapter is the first of a three-chapter discussion providing: a general introduction to the concepts applied in this thesis, a method for measuring α_s at the parton level, and the phenomenology and technology needed to go from the parton-level calculations to the experimentally observable hadrons. In this chapter, the Naive Parton Model for deep inelastic scattering is presented, QCD extensions are discussed, the variation of α_s with momentum transfer is reviewed, and, finally, some important technical details are presented. Section 1.3 is especially important for interpreting the experimental results in chapter 6 and sections 1.6 and 1.9 provide necessary background for the discussion of chapter 2 and analysis of chapter 7.

1.1 The Naive Parton Model

In the Naive Parton Model, the nucleon consists of three point-like, massless, valence quarks, which do not interact. The single photon exchange Feynman diagram for a muon-nucleon interaction is shown in figure 1.1a. A trivial feature of the scattering is that, in the center-of-momentum (CMS) frame of the virtual photon and the nucleon, the outgoing scattered quark and target remnants will move back-to-back with equal energies, resulting in a "2 prong" event structure. Neither the incoming quarks nor the scattered quark nor target remnant have transverse momentum with respect to the virtual photon axis.

The event kinematics are determined entirely by the incoming and outgoing muons. The variables which describe the event are:

$p_\mu \equiv (E_\mu, \vec{p_\mu})$	The 4-vector of the incoming muon in the lab.
$p'_\mu \equiv (E'_\mu \vec{p_\mu}')$	The 4-vector of the outgoing muons in the lab.
$T \equiv (M, \vec{0})$	The 4-vector of the target nucleon in the lab, where M is the mass of the nucleon.
$q \equiv (\nu, \vec{q})$	The 4-vector of the virtual photon in the lab.

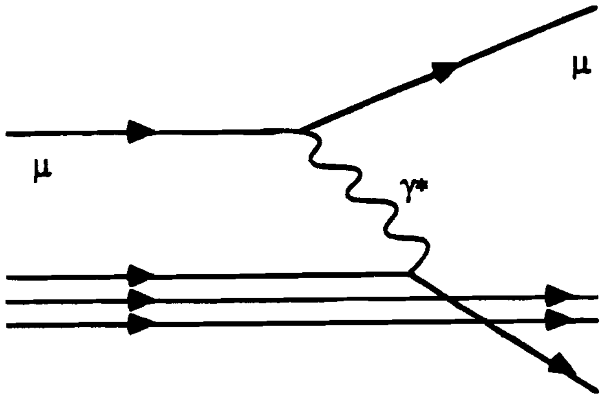

Figure 1.1. Single photon exchange in the simple parton model. The Feynman diagram of the process.

$\vec{q} = \vec{p_\mu} - \vec{p'_\mu}$ is the three vector of the virtual photon in the lab.

$\nu = E - E' = (q \cdot T)/M$ is an invariant and is the energy of the virtual photon in the lab.

Q^2 The negative squared 4-momentum of the virtual photon, $Q^2 = -q^2 = |\vec{q}|^2 - \nu^2 \approx 4E_\mu E'_\mu sin^2\theta/2$.

x_{Bj} $= Q^2/2M\nu = (q \cdot q)/(2q \cdot T)$ is an invariant. In the frame in which the target moves with infinite momentum, x_{Bj} is the fraction of the nucleon's momentum carried by the struck quark.

W^2 The squared invariant mass of the virtual photon – nucleon system, $W^2 = 2M\nu - Q^2 + M^2 = Q^2(1 - x_{Bj})/x_{Bj}$. In the CMS, W is the total energy of the system.

y The fraction of the incoming muon energy which is carried by the virtual photon, $y = \nu/E_\mu$

Note that radiation of a second real or virtual photon by the muon in the event will lead to incorrect measurement of the kinematic variables associated with the virtual photon. Also, in the case of real bremsstrahlung, an extra photon unrelated to the deep inelastic scatter may be included among the detected particles from the event. Examples of real photon bremsstrahlung are shown in figure 1.2. As will be discussed later in chapter 5 of this thesis, the rate of these "radiative" events can be quite high in some kinematic regions of deep inelastic scattering. Cuts on y and on events with real photons in a cone about the incoming muon direction have been chosen to remove most of these events. No cuts on event topology were applied.

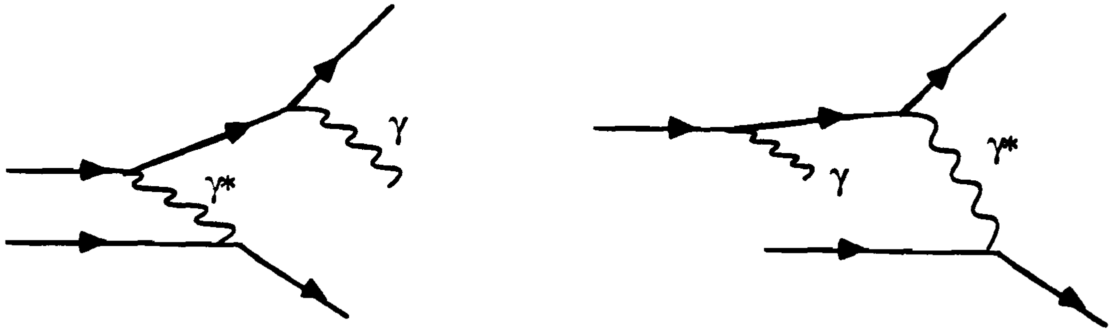

Figure 1.2. Some examples of real photon bremsstrahlung by the muon in a deep inelastic scattering event. In these cases, the kinematic variables determined through measurement of the incoming and outgoing muon do not reflect the true virtual photon kinematics.

1.2 The Experimental Cross Section

The experimental differential cross section for deep inelastic scattering is given by[16]

$$\frac{d\sigma^2}{dxdy} = \frac{2\pi\alpha^2}{Q^2xy}F_2(x,Q^2)[(1+(1-y)^2) - y^2(F_L/F_2)], \tag{1.1}$$

where F_L represents the contribution from the absorption of longitudinally polarized (*helicity* = 0) virtual photons and $F_2 - F_L$ is the contribution from transversly polarized photon absorption. A more familiar expression of the cross section uses F_2 and $R = F_L/(F_2 - F_L)$, the ratio of longitudinal to transverse cross sections:

$$\frac{d\sigma^2}{dxdy} = \frac{2\pi\alpha^2}{Q^2xy}F_2(x,Q^2)[1 - y + \frac{y^2}{2(1+R)}] \tag{1.2}$$

As will be discussed section 1.9, the structure functions are interpreted as charge-weighted sums of the distributions of the particles in the nucleon.

In any model with spin 1/2, massless quarks with no transverse momentum, such as the Naive Parton Model described above, helicity conservation requires $F_L = 0$, or $R = 0$. For integer spin quarks $R = \infty$. Experimental measurement has shown $R \sim 0.1 - 0.3$.[17] The small but nonzero value suggests spin 1/2 quarks with transverse momentum.

Further evidence of a problem with the Naive Parton Model comes from the dependence of the structure functions on Q^2. In the model above, the structure functions would have no Q^2 dependence. However, experimental measurements have demonstrated variation with Q^2.[18] Therefore mechanism in the model is needed which allows the partons to interact and their number to "evolve" with Q^2.

Finally, the deep inelastic scattering data indicated that the charged quarks only carried approximately half of the total momentum of the proton.[18] This implies that particles which carry the missing momentum but do not interact electroweakly, and hence are not observed directly through the structure function measurements, are needed in the model.

In response to these problems, Quantum Chromodynamics, the theory of the strong interaction, was developed.

1.3 DIS within the QCD Framework

The theory describing the strong interaction between the quarks is called Quantum Chromodynamics because the charge states of the strong force are referred to as "colors." In brief, within QCD theory,

- The six flavors of quarks are distinguishable only by their masses.
- The quarks are fermions, carrying electric charge in units of $-1/3$ and $+2/3$.
- Each quark has three color-charged states: red (R), green (G) and blue (B).
- The color neutral combinations of quarks are *color–anticolor* and RGB.
- The sets of quarks which form hadrons are color neutral and have integral electric charge: Mesons are a quark and antiquark ($q\bar{q}$); Baryons are three quarks (qqq).
- The color force is mediated by gluons, which are vector bosons, electrically neutral, and massless.
- The gluons are in color octet states. Hence, they carry the color charge and may self-interact, *eg.* $g(R\overline{B}) \rightarrow g(R\overline{G}) + g(G\overline{B})$. Among the field theories of the nongravitational forces, this self-interaction is unique.
- When a quark radiates a gluon, it changes color. For example, a quark with color charge R may radiate an $R\overline{G}$ gluon, becoming G.

Collectively, quarks and gluons are called partons.

Within QCD, the constituents of the nucleon are valence quarks, sea quarks and gluons. There are three valence quarks, as in the Naive Parton Model. The sea quarks are in $q\bar{q}$ pairs, so the flavor and color quantum numbers cancel. In QCD, sea quarks can be generated from quarks radiating gluons which then split into a $q\bar{q}$ pair. The gluons radiated by quarks in the nucleon also may split into a pair of gluons, resulting in an enhanced gluon sea. The probability of a parton splitting is dependent on Q^2.

The first order QCD processes which occur in deep inelastic scattering events are shown in figure 1.3. In the first column, the Feynman diagrams are given. In the second column, a schematic of the outgoing partons in the CMS is illustrated. Rows a and b

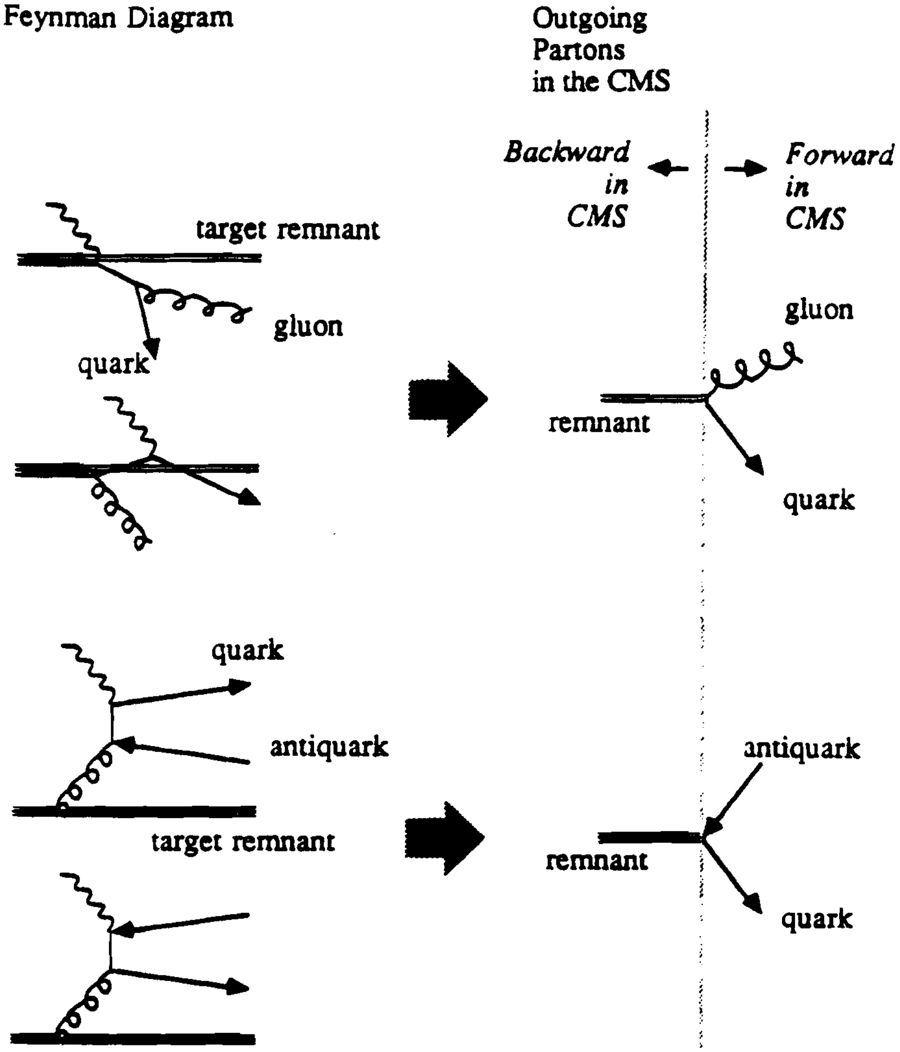

Figure 1.3. QCD processes which occur in deep inelastic scattering. **a)** and **b)** Gluon bremsstrahlung, **c)** and **d)** Photon- gluon fusion

show gluon bremsstrahlung by a valence q or a sea q or $\bar{q}$. This is analogous to the photon bremsstrahlung diagram in QED illustrated in figure 1.2a and b. Rows c and d show interaction with a gluon which splits in to a $q\bar{q}$ pair in the presence of the virtual photon.

The ability to resolve the processes shown in figure 1.3 depends on the Q^2 of the event. In analogy to the de Broglie wavelength, the resolution scale of the scattering process goes as $1/\sqrt{Q^2}$ At low Q^2, the quark constituents of the proton are resolved but QCD processes cannot be observed. It is only when Q^2 is sufficiently large that the processes shown in figure 1.3 become "visible." For a more detailed discussion of this effect, see the report by Reya in reference 19.

Several important points in figure 1.3 should be noted:

- The diagrams which are shown in figure 1.3 represent the full set of contributions to the deep inelastic cross section that are proportional to α_s.
- The partons involved in the interaction have transverse momentum with respect to the virtual photon axis. The magnitude of the transverse momentum of the outgoing partons can be calculated exactly from the kinematics of the event. The following definitions will be used:

  q is the virtual photon 4-vector,
  k is the incident parton 4-vector,
  p, r are the 4-vectors of the outgoing partons, so...
  θ_p, θ_r are the angles between the outgoing partons and the axis formed by $\overrightarrow{q}$.
  $u = k \cdot p / k \cdot (q + k) = k \cdot p / k \cdot q$
  χ is the fraction of the proton momentum carried by the incoming parton
  $z = q \cdot q / 2q \cdot k = x_{Bj}/\chi$, the fraction of the incident parton's momentum which is carried by the parton when it is struck by the virtual photon.

  Rewriting $(q + k) = (p + r)$ as $q + k - p = r$ and taking the dot product of this expression first with q and then with k, results in two equations depending on $|r| cos\theta_r$. Combining so as to eliminate $|r|$ and $cos\theta_r$ leaves an equation for the transverse momentum in terms of p, q, and k. For application of this in the theory discussed in chapter 1, it is convenient to change to the variables Q^2, z and u. Then using $P_T^2 = |r|^2(1 - cos^2\theta_r)$, one finds

  $$P_T^2 = Q^2 \frac{(1 - z)}{z} u(1 - u) \tag{1.3}$$

  Note that the transverse momentum depends on the resolution scale, $\sqrt{Q^2}$, of the event. The magnitudes of the transverse momenta of the two outgoing partons are equal, but the directions are opposite, so the total transverse momentum in the event is zero.
- The transverse momentum causes the events to have a "three-pronged" structure at the partonic level when observed in the CMS.

1.4 Terminology for QCD Calculations

Perturbative QCD (PQCD) is the application of perturbative methods to the theory described above. The cross section is calculated using an expansion in powers of α_s, which can be applied if the coupling constant, α_s, of the interaction is sufficiently small,

$$\hat{\sigma} = \hat{\sigma}_0 \alpha_s^N (1 + \hat{\sigma}\sigma_s + \cdots)$$

The highest power of α_s before the series is truncated is called the "order" of the calculation. The portion of the series which is explicitly kept is called "hard." The truncated terms will be absorbed into the parton distributions, which represent "soft" processes not described by the hard calculation.

In accordance with the nomenclature used in recent theoretical calculations of deep inelastic scattering, a diagram resulting in one current parton and one target remnant will be called a 1−1 parton event. One that results in two current partons and a remnant and will be called a 2+1 parton event.


1+1 LO

1+1 NLO

2+1 LO

Figure 1.4. Diagrams and associated terminology.

For deep inelastic scattering, the leading order (LO) and next-to-leading order (NLO) 1+1 full calculations and the LO calculation for the 2+1 parton events are available. The diagrams are shown with the associated terminology in figure 1.4. This may be written as

$$\hat{\sigma}_{DIS}^{NLO} = \hat{\sigma}_{1+1}^{LO} + \hat{\sigma}_{1+1}^{NLO} + \hat{\sigma}_{2+1}^{LO} \qquad (1.4)$$

This is a complete calculation to NLO for the DIS cross section.

In order to be certain that the series may be truncated at this order, the contributions to the next-to-next-to-leading order deep inelastic cross section must be calculated. The most of terms have been calculated and the contributions are small, permitting truncation of the series. This will be discussed further in section 2.5.

1.5 The Cross Section for 2+1 Parton Events

The LO cross section for the 2+1 processes shown in figure 1.3 ($\hat{\sigma}_{2+1}$) diverges for emission of partons with low momenta or at small angle. The cross sections for gluon bremsstrahlung and photon-gluon fusion are, respectively:[20]

$$\begin{aligned} \frac{d\sigma^{qG}}{dz\,du} &= \alpha_s \frac{1+uz}{(1-u)(1-z)} \\ \frac{d\sigma^{q\bar{q}}}{dz\,du} &= \alpha_s \frac{[u^2+(1-u)^2][z^2+(1-z)^2]}{u(1-u)} \end{aligned} \qquad (1.5)$$

These diverge when $u \to 0$ or u or $z \to 1$.

Recalling equation 1.3, multiplying the above functions by P_T^2 cancels the divergences in the cross sections at this order. This fact was originally exploited by Altarelli and Martinelli[21] to calculate the average squared transverse momentum of 2+1 parton processes. Their calculation is the starting point of the discussion in chapter 2 and of the analysis in chapter 7.

1.6 The QCD Coupling Constant, α_s

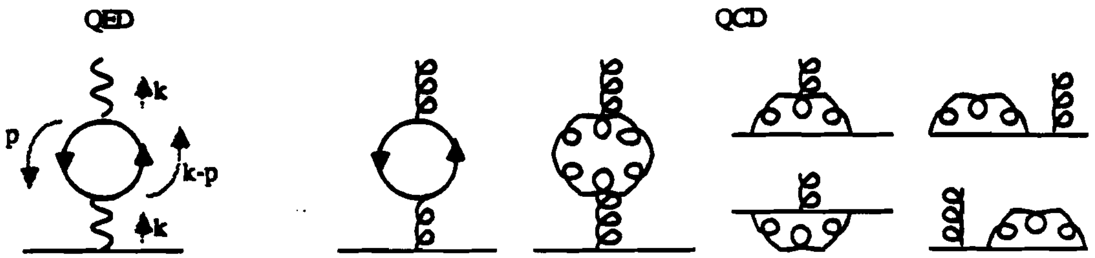

Figure 1.5. Examples of one loop corrections to the propagators of QED and QCD

The coupling constant represents the relative strength, or charge, of the interactions. The word "constant" is a misnomer; in fact, the strength of interactions varies with the resolution scale of the interaction, Q^2.

Qualitatively, the variation of the QCD coupling constant can be understood in terms of two competing effects. For convenience in the illustration in this paragraph, only two charge states will be considered and the bare color charge is taken to be "positive." First, vacuum polarization introduces a negative charge density in the region of the bare charge, reducing the total apparent color charge measured at some distance away. This effect also appears in QED with the electromagnetic charge. Second, the self-interaction of the gluons in QCD produces charge exchange between the bare charge and the field surrounding it. As the bare charge radiates gluons, its color fluctuates. Effectively, the positive charge is spread throughout the gluon cloud, producing a positive charge density surrounding the fluctuating bare charge. This QCD effect has no equivalent in QED.

There is no analogy or simple calculation which indicates the dominant effect. The discussion below presents an overview of the formalism for calculating the variation of the coupling constant with Q^2, drawn largely from the textbooks by Quigg[22] and Halzen & Martin[23]. Quigg provides a step-by-step calculation which fills in many of the gaps omitted in the discussion below. The calculations are performed within the framework of PQCD.

The variation of the coupling constant is calculated from the loop corrections to the propagator. For the QED and PQCD cases, the one loop corrections are shown in figure 1.5. Although the sum of the momentum of the partons in the loop must be equal to the total incoming momentum k, the momentum p is unrestricted. Therefore it is necessary to integrate over all p from 0 to ∞. The resulting cross section diverges logarithmically. The one loop correction to the propagator can be written as

$$I_1(Q^2) = -\left[\frac{\alpha}{4\pi}\beta_0 \ln(\frac{M^2}{k^2})\right]_{M\to\infty}$$

where $\alpha/4\pi$ is the bare coupling strength and β_0 represents factors related to the particles in the loops.

This equation can be re-written as a k^2 dependent, finite term and a k^2-independent, infinite term

$$I_1(Q^2) = -\frac{\alpha}{4\pi}\beta_0\Big(\big[\ln(\frac{M^2}{\mu^2})\big]_{M\to\infty} + \ln(\frac{k^2}{\mu^2})\Big),$$

where μ is some arbitrary scale at which the terms are separated. In analogy with redefining the ground level of a measurement of a potential in electromagnetism, an infinite "counterterm" can be added to the QED or PQCD lagrangian which results in cancellation of the infinite term. In the process, finite pieces of the counterterm are absorbed in a redefinition of the second term, causing α to become dependent on the "renormalization" scale, μ^2. There is a wide variety of renormalization"schemes," however in the one-loop correction with massless particles, μ^2 is scheme-independent.[24] μ^2 is scheme-dependent for higher numbers of loops. An excellent discussion of renormalization is provided in the textbook by Ramond.[24] After renormalization,

$$I_{1\ finite}(k^2) = \frac{\alpha(\mu^2)}{4\pi}\beta_0 \ln(\frac{k^2}{\mu^2})$$

The coupling strength is modified by

$$\alpha(k^2) =$$

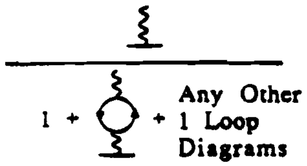

$$= \alpha(\mu^2)\left[\frac{1}{1 + I_{1\ finite}}\right]$$

$$= \frac{\alpha(\mu^2)}{1 + \frac{\alpha(\mu^2)}{4\pi}\beta_0 \ln(\frac{k^2}{\mu^2})}$$

The next step is to evaluate β_0 in order to determine the behavior of the coupling strength for the QED and PQCD theories. In the case of fermion loops,

$$\beta_0 = -\frac{2}{3}n_f$$

where n_f is the number of fermion loop types. In QED, for low Q^2, only e^+e^- pairs form the loops, (see figure 1.5a) so $n_f = 1$. Noting that the definition of the coupling strength in QED differs by a factor of 2 from PQCD, one finds $\beta_{0\ QED} = -(\frac{2}{3})(2) = -\frac{4}{3}$, hence,

$$\alpha_{QED}(k^2) = \frac{\alpha_{QED}(\mu^2)}{1 - \frac{\alpha_{QED}(\mu^2)}{3\pi}\ln(\frac{k^2}{\mu^2})}$$

In PQCD, both fermion and gluon loops contribute. The relative magnitudes of the contributions from diagrams 1.5b-e vary, depending on the gauge in which the calculation is performed, but the magnitude of the total contribution is always the same, large, and positive, resulting in $\beta_0 = 33 - 2n_f/3$. As long as the number of quarks is less than 17, the PQCD coupling will decrease with k^2:

$$\alpha_s(k^2) = \frac{\alpha_s(\mu^2)}{1 + \frac{\alpha_s(\mu^2)}{12\pi}(33 - 2n_f)\ln(\frac{k^2}{\mu^2})}$$

The renormalization mass can be eliminated by evaluating at $\mu = \Lambda$, where $\alpha_s(\Lambda) \rightarrow \infty$:

$$\alpha_s = \frac{12\pi}{(33 - 2n_f)\ln(\frac{k^2}{\Lambda^2})} \tag{1.6}$$

In order to calculate the two loop corrections, the "renormalization group equation" is often employed. This equation requires that any physical observable must be independent of the renormalization constant. Examples of the use of this equation to obtain α_s can be found in a report by Altarelli[25], and in a shorter, experimentally-oriented presentation by Reya.[19]

The renormalization group equation is written as

$$\mu^2 \frac{\partial}{\partial \mu^2} \alpha_s(\mu^2) = \beta(\alpha_s(\mu^2))$$

The function β may expanded in powers of α_s

$$\beta(\alpha_s) = \beta_0 \alpha_s^2 + \beta_1 \alpha_s^3 + \beta_2 \alpha_s^4 + \ldots$$

Solving for β_0 recovers the expression calculated above. β_1 can also be calculated: $\beta_1 = 306 - 38n_f/3$. These first two terms are the same in any scheme, while the remaining terms are renormalization scheme-dependent.[26] Truncating at the first two terms gives

$$\int_{\Lambda^2}^{k^2} \frac{d\mu^2}{\mu^2} = \int_{\alpha_s(\Lambda^2)}^{\alpha_s(k^2)} \frac{d\alpha_s}{\alpha_s^2(\beta_0 + \beta_1 \alpha_s)}$$

To all orders, the solution can be written as[19]

$$\alpha_s(k^2) = \frac{4\pi}{\beta_0 \ln(k^2/\Lambda^2)} \left[1 - \frac{\beta_1 \ln\ln(k^2/\Lambda^2)}{\beta_0^2 \ln(k^2/\Lambda^2)}\right] + [\cdots],$$

where the contribution of the terms beyond the first two are represented by $[\cdots]$. The physical $\alpha_s(k^2)$ to all orders is not renormalization scheme-dependent, while the $[\cdots]$ terms are renormalization scheme-dependent,[26] therefore the explicitly calculated terms above must have an implicit renormalization scheme dependence hidden within Λ. Truncating leads to

$$\alpha_s(k^2) = \frac{4\pi}{\beta_0 \ln(k^2/\Lambda_{rs}^2)} \left[1 - \frac{\beta_1 \ln\ln(k^2/\Lambda_{rs}^2)}{\beta_0^2 \ln(k^2/\Lambda_{rs}^2)}\right],$$

where the subscript rs explicitly notes the renormalization scheme dependence.

The final step is to show that the energy scale, k^2, in the above discussion should be identified with Q^2 for the processes shown in figure 1.3. The classic derivation of $k^2 \equiv Q^2$ in deep inelastic scattering, by Georgi and Politzer,[27] and Gross and Wilczek, [28] and Altarelli and Parisi,[29] comes from calculation of the variation of the parton distributions with Q^2, the PQCD-predicted scaling violations (see ref. 25, ch. 4). This calculation is for an inclusive process, $\mu + p \rightarrow \mu + X$, which has only one observable large energy scale Q^2. This author has not found a mathematical proof of $k^2 \equiv Q^2$ for the exclusive processes shown in figure 1.3, although all of the theoretical calculations for these processes assume this (see, for example, references 25, 21, 20, 31). However, one can show $k^2 \equiv Q^2$ through the following argument. The coupling constant α_s must depend upon some observable large energy scale. The two possibilities for the processes in figure 1.3 are Q^2 and P_T^2. However, from equation 1.3, $P_T^2 \sim Q^2$. Hence, there is actually only one scale, and it may be taken to be Q^2

$$\alpha_s(Q^2) = \frac{12\pi}{(33 - 2n_f)\ln(Q^2/\Lambda_{rs}^2)} \left[1 - \frac{6(153 - 19n_f)\ln\ln(Q^2/\Lambda_{rs}^2)}{(33 - 2n_f)^2 \ln(Q^2/\Lambda_{rs}^2)}\right]. \qquad (1.7)$$

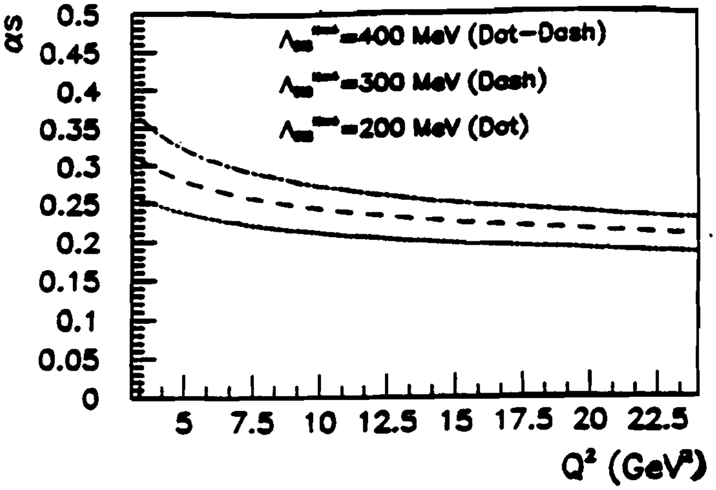

Figure 1.6. α_s for $n_f = 4$, $\Lambda = 200, 300, 400$ MeV

The PQCD couplings for various choices of Λ are shown as a function of Q^2 in figure 1.6. At low values of Q^2, or large distance scales, the PQCD coupling constant becomes stronger. This fact, crucial to the theory of the confinement of partons to the nucleon, was first noted by Gross, Wilczek and Politzer[32]. However, at small distance scales, or high values of Q^2, the coupling constant becomes small, permitting perturbative expansion of calculations in α_s. The perturbative framework may be applied for $Q^2 \gg \Lambda^2$, where Λ is a fundamental parameter of PQCD which must be measured experimentally.

The quantity Λ in equation 1.7 is defined strictly within the context of the choice of n_f. For massless quarks, n_f is fixed, but for massive quarks, n_f changes as a function of Q^2. The decoupling theorem maintains that each heavy quark is decoupled from the cross section until a threshold, Q_i, is crossed.[33] On the other hand, α_s and the parton distributions must be continuous across the boundary and reduce to their familar form between thresholds. Therefore, the discontinuity is absorbed into the definition of Λ. Thus, any statement concerning Λ is meaningless without a quoted n_f. Since $m_{charm}^2 \approx (1.5\ GeV)^2$ and $m_{bottom}^2 \approx (5\ GeV)^2$, for this analysis, where $3 < Q^2 < 25\ GeV^2$, $n_f = 4$ is used.

The variation with Q^2 of a quantity which is expected to be equivalent to α_s, is presented in chapter 7.

1.7 The Factorization Theorem

According to the Factorization Theorem,[34] the physical cross section is a scheme-independent convolution of the probabilities of finding a parent parton for the interaction in the nucleon and the hard scattering cross section calculated with the perturbative methods above. Hence, the cross section, σ, factors into two terms: the parton distribution functions, f, which contain information about the soft processes happening before the event occurs, and the hard parton scattering, $\hat{\sigma}$. Factorization can be mathematically expressed as

$$\sigma = \sum_{partons} f(\chi, Q^2, \Lambda) \otimes \hat{\sigma}(\chi, Q^2, \Lambda),$$

where χ is the momentum of the parent parton in the event. Both f and $\hat{\sigma}$ must be defined to the same order so that scheme dependences will cancel and the physical cross section is scheme-independent.

1.8 The Order of Structure Functions and Parton Distributions

For the analysis of chapter 7, parton distributions are utilized. This section describes the the structure functions F_2 and R in terms of the parton distributions. The truncated soft processes discussed in section 1.4 are parameterized by these distributions. $q_i(x, Q^2)$ represents the probability distribution for partons of flavor i with electric charge e_i^2 with at x and Q^2. $G(x, Q^2)$ represents the probability distribution of the gluons. Because these parton distributions represent the incalculable soft processes, there is no theoretical prediction for these functions. They are extracted from the measured structure functions, which are, in turn, measured from the absolute cross section for deep inelastic Muon scattering. Specifics on the choice of parton distributions and discussion of the error introduced in the analysis of chapter 7 due to uncertainties in these measurements are addressed in chapter 2.

- *Defining F_2 and xG in Leading and Next-to-Leading Order*

The experimental F_2 is a measured quantity which is interpreted as a combination of quark distributions. The way in which the quark distributions are combined depends on the order of the calculation. The quark distributions are then "tuned" to give the measured value of F_2. The quark distributions directly affect xG through the momentum sum requirement:

$$\int_0^1 \left[x_{Bj} \sum_i [q_i(x_{Bj}, Q^2) + \overline{q_i}(x_{Bj}, Q^2)] + x_{Bj} G(x_{Bj}, Q^2)\ \right] dx_{Bj} = 1 \qquad (1.8)$$

The contributions to F_2^{LO} are from muon-quark scattering and from collinear or soft gluon emission or photon gluon fusion. The collinear and soft processes go as $\alpha_s \ln(Q^2) \sim 1$, and are, therefore, of the zeroeth order in α_s.[25] F_2^{LO} is then given by the sum of the parton distributions:

$$F_2^{LO}(x_{Bj}, Q^2) = x_{Bj} \sum_i e_i^2 [q_i(x_{Bj}, Q^2) + \overline{q_i}(x_{Bj}, Q^2)] \qquad (1.9)$$

For this analysis the NLO definitions for the parton distributions are used. At this order,

$$
\begin{aligned}
F_2^{NLO}(x_{Bj},Q^2) = & F_2^{LO}(x_{Bj},Q^2)+ \\
& \frac{C\alpha_s}{2\pi}\int_x^1 \left[f_2^q(x/y)\sum_i e_i^2(q_i(x_{Bj},Q^2)+\overline{q_i}(x_{Bj},Q^2))+\right. \\
& \left. 2N_f f_2^g(x/y)G(x_{Bj},Q^2)\right]
\end{aligned}
\tag{1.10}
$$

At NLO, the parton distributions depend upon the scheme used to renormalize divergences. The scheme defines the point at which a process is considered to be calculable using perturbative methods. This affects the number of partons defined as low momentum, or "soft," within the nucleon. Often, the modified minimal subtraction ($\overline{MS}$) scheme is used to regularize divergences. In this case the C constants and f functions of equation 1.10 are given by reference 35. In this scheme, the hard contributions are explicitly retained, so $f_2^g(x/y)$ has a small, but non-zero, value. Another popular option for defining parton distributions is commonly called DIS. In this scheme, the entire NLO term is absorbed into the definition of the parton distributions.[33] The gluon distribution is then entirely determined by the momentum sum requirement.

The Q^2 dependence of F_2 is governed by the evolution equations, also known as the Gribov-Lipatov-Altarelli-Parisi equations:[25]

$$
\begin{aligned}
\frac{dq_i(x,Q^2)}{d\ln Q^2} &= \frac{\alpha_s(Q^2)}{2\pi}\int_{x_{Bj}}^1 \frac{dy}{y}\left[P_{qq}(x/y)q_i(y,Q^2)+P_{qg}(x/y)G(y,Q^2)\right] \\
\frac{dG(x_{Bj},Q^2)}{d\ln Q^2} &= \frac{\alpha_s(Q^2)}{2\pi}\int_{x_{Bj}}^1 \frac{dy}{y}\left[\sum_j P_{gq}(x/y)q_j(y,Q^2)+P_{gg}(x/y)G(y,Q^2)\right]
\end{aligned}
\tag{1.11}
$$

The P functions describe the probability that a quark will radiate a gluon (P_{qq}), that a gluon will split into a $q\bar{q}$ pair (P_{qg}) or that a gluon will split into a pair of gluons (P_{gg}). The techniques used to derive these equations had their roots in the QED calculations of Weizsäcker and Williams.[36] A useful review of the derivation of these equations, by analogy to QED, is given in chapter 8 of the textbook by Quigg.[22]

The parton distributions are extracted by experimental fits to the measured data within the PQCD framework described above. This is discussed further in chapter 2.

- $R = F_L/(F_2 - F_L)$

Within PQCD, R is given by[21]

$$
R_{QCD} = \frac{\frac{\alpha_s}{2\pi}\int_x^1 \frac{d\chi}{\chi}[\sum_{i=q,\bar{q}} e_i^2 q_i(x)\sigma^L_{q\gamma*}(\frac{x}{\chi}) + \sum_{i=q} e_i^2 G(x)\sigma^L_{G\gamma*}(\frac{x}{\chi})]}{\sum_{i=q,\bar{q}} q_i(x)e_i^2 + \frac{\alpha_s}{2\pi}\int_x^1 \frac{d\chi}{\chi}[\sum_{i=q,\bar{q}} e_i^2 q_i(x)\sigma^T_{q\gamma*}(\frac{x}{\chi}) + \sum_{i=q} e_i^2 G(x)\sigma^T_{G\gamma*}(\frac{x}{\chi})]},
\tag{1.12}
$$

where σ_L and σ_T refer to the longitudinal and transverse components of the cross section and $q\gamma*$ and $G\gamma*$ refer to gluon bremsstrahlung and photon–gluon fusion. This formula is used to calculate R_{QCD} throughout this analysis. The effect of using R_{QCD} rather than the experimental parameterization of R is discussed in chapter 2.

1.9 Order and Scheme in the Thesis

Order (assumes O(n+1) is Calc'd to be small)	Terminology	Largest Power of QCD Coupling Constant in the Perturbative Expansion	Parton Distribution Functions	QCD Coupling definition
0th	LO	0	1-loop (LO PDF's)	1 loop
1st	NLO	1	2-loop (NLO PDF's)	2 loop
2nd	NNLO	2	3-loop (NNLO PDF's)	3 loop

Table 1.1. Consistent use of Order when calculating the physical cross section.[37]

In this chapter, the formalism for calculating PQCD effects in deep inelastic scattering has been introduced. As has been shown, the calculations of the hard scattering processes have a residual scheme and order dependence which must be properly cancelled in order the obtain the physical cross section. Therefore, consistent use of order and scheme is important. Table 1.1 reviews the consistent use of order when calculating the physical cross sections.[37]

This analysis makes use of the deep inelastic cross section defined to next-to-leading order. Accordingly, the NLO structure functions in the DIS scheme and equation 1.7 for α_s with $\Lambda = \Lambda_{DIS}^{n_f=4}$ are used.

Chapter 2

The Transverse Momentum of Partons

This chapter develops a plan for measuring α_s from the average squared transverse momentum of current partons in 2+1 events, $\langle P_T^2 \rangle$, in a hypothetical parton-level experiment. This plan will be followed, with some modifications discussed in chapter 3, in the analysis of chapter 7.

The starting point is a calculation by Altarelli and Martinelli,[21] which was recently rederived, with small corrections by Körner, Mirkes, and Schüler.[20] In all of the calculations below, the parton-level kinematic variables, as defined in chapter 1 and appendix A, will be used.

In brief, this chapter provides:

- The derivation of the equation for $\langle P_T^2 \rangle$ of the partons in 1+1 and 2+1 parton events and its dependence on α_s.
- A discussion of the uncertainties from the parton distributions.
- A hypothetical parton-level experimental method for measuring $\langle P_T^2 \rangle$.
- An estimate of the higher order effects.

The kinematic ranges: $400 < W^2 < 800\ GeV^2$, $3 < Q^2 < 24\ GeV^2$ and $0.003 < x_{Bj} < 0.04$, with $\langle W^2 \rangle = 600\ GeV^2$, will be regarded as accessible to this analysis. Detailed discussion of the E665 data and the kinematic cuts will be provided in chapter 5.

2.1 The Average Parton Transverse Momentum Squared

By definition, the $\langle P_T^2 \rangle$ is given by

$$\langle P_T^2 \rangle = \Big(\int P_T^2 \frac{d\sigma^2_{DIS\ NLO}}{dx_{Bj}dydP_T^2} dP_T^2\Big)/\Big(\int \frac{d\sigma^2_{DIS\ NLO}}{dx_{Bj}dydP_T^2} dP_T^2\Big). \qquad (2.1)$$

As a matter of convenience in evaluating equation 2.1, the integrals are performed over u and z, using equation 1.3, derived in the previous chapter.

The integral in the denominator is given by equation 1.1 or 1.2. Note that this integral is over all 1+1 and 2+1 parton events.

The integrand in the numerator is weighted by P_T^2. Rewriting the numerator using equation 1.4,

$$P_T^2\sigma_{DIS}^{NLO} = P_{T\ 1+1\ LO}^2\sigma_{1+1}^{LO} + P_{T\ 1+1\ NLO}^2\sigma_{1+1}^{NLO} + P_{T\ 2+1\ LO}^2\sigma_{2+1}^{LO}.$$

Since this calculation assumes the incoming parton has no intrinsic momentum, thus requiring all 1+1 parton events to have $P_{T\ 1+1}^2 = 0$, the above equation becomes

$$P_T^2\sigma_{DIS}^{NLO} = P_{T\ 2+1\ LO}^2\hat{\sigma}_{2+1}. \tag{2.2}$$

Equation 2.2 is not divergent since P_T^2 removes the divergence, as shown in section 1.5.

Equation 2.2 was evaluated at the parton level by Altarelli and Martinelli in reference 21. The calculation was performed by dividing the interaction into two event types, gluon bremsstrahlung (q) and photon-gluon fusion (G), which were calculated separately for interactions with transversely polarized (T) and longitudinally polarized (L) virtual photons. The result will be called the P_T^2 weighted splitting functions in this thesis. Explicitly factoring out the Q^2 dependence gives

$$\begin{aligned}
Q^2 p_q^T(z) &= \int du \frac{d\hat{\sigma}_q^T}{dzdu} P_T^2 = Q^2 \frac{4}{3}\frac{4z^2 - 2z + 7}{12z}, \\
Q^2 p_G^T(z) &= \int du \frac{d\hat{\sigma}_G^T}{dzdu} P_T^2 = Q^2 \frac{1-z}{3z}[z^2 + (1-z)^2], \\
Q^2 p_q^L(z) &= \int du \frac{d\hat{\sigma}_q^L}{dzdu} P_T^2 = Q^2 \frac{4}{9}(1-z), \\
Q^2 p_G^L(z) &= \int du \frac{d\hat{\sigma}_G^L}{dzdu} P_T^2 = Q^2 \frac{2}{3}(1-z)^2,
\end{aligned} \tag{2.3}$$

These must be convoluted with the probability of finding a parent parton at a given χ and Q^2 in order to evaluate 2.2. These probabilities are parameterized by the function $F_2(\chi, Q^2)$ and the parton distribution $xG(\chi, Q^2)$ and are discussed in the next section. The result must be integrated from from x_{Bj} to 1 because all parent partons with fractional momenta $\chi \geq x_{Bj}$ may contribute to the processes at x_{Bj}.

Dividing numerator by denominator,

$$\begin{aligned}
\langle P_T^2 \rangle = &\frac{\alpha_s(Q^2)}{2\pi}\frac{Q^2 x_{Bj}}{F_2(x_{Bj}, Q^2)}\frac{1 - y + y^2/2}{1 - y + y^2/2(1 + R_{QCD})} \\
&\cdot \int_{x_{Bj}}^1 f(\chi, y_{Bj}, F_2(\chi, Q^2), G(\chi, Q^2), p(\frac{x_{Bj}}{\chi}))d\chi
\end{aligned} \tag{2.4}$$

where

$$\begin{aligned}
\int_{xBj}^1 f \equiv &\int_{x_{Bj}}^1 \frac{d\chi}{\chi^2}[F_2(\chi, Q^2)p_q^T(\frac{x_{Bj}}{\chi}) + (\sum_i e_i^2)\chi G(\chi, Q^2)p_G^T(\frac{x_{Bj}}{\chi})] \\
&+ \frac{1-y}{1 - y + y^2/2}\int_{x_{Bj}}^1 \frac{d\chi}{\chi^2}[F_2(\chi, Q^2)p_q^L(\frac{x_{Bj}}{\chi}) + (\sum_i e_i^2)xG(\chi, Q^2)p_G^L(\frac{x_{Bj}}{\chi})].
\end{aligned} \tag{2.5}$$

It is very important to note that $\langle P_T^2 \rangle$ is the average transverse momentum of ALL events, with the transverse momentum of 1+1 parton events assumed to be zero.

Measuring the kinematic variables, the parton distributions, and $\langle P_T^2 \rangle$ of the partons as a function of Q^2, permits extraction of α_s:

$$\alpha_s = \frac{\langle P_T^2 \rangle}{Q^2} \frac{2\pi F_2}{x_{Bj}} \frac{1}{\int_x f(\chi, y_{Bj}, F_2, G, p) dx} \tag{2.6}$$

So far, the calculation has not considered the magnitude of the $O(\alpha_s^2)$ terms. The calculations that exist will be discussed in a later section in this chapter and will be shown to be dependent upon the jet algorithm applied. The calculated $O(\alpha_s^2)$ terms are small for this analysis, so the consistent set of NLO definitions, listed in table 1.1, will be used in this throughout this chapter.

2.2 The Experimental Inputs: R, F_2 and xG

R, F_2 and xG defined to NLO are required as inputs to equations 2.6 and 2.4. These are extracted from the cross sections for deep inelastic scattering, which E665 has not yet measured. Therefore, results from other experiments are used as inputs. The uncertainty from F_2, R and the parton distributions, including xG, is discussed below: A useful review of recent experimental measurements of all three distributions is given in reference 38.

- *The value of R*

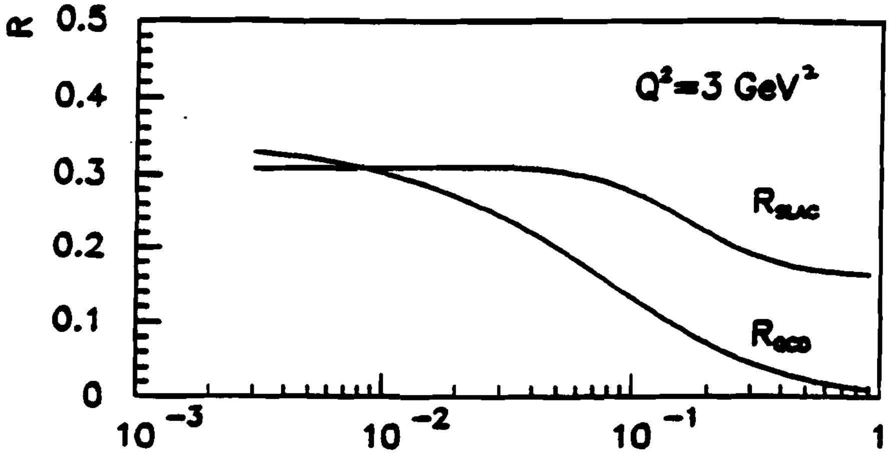

Figure 2.1. Comparison of R_{SLAC} to R_{QCD}.

The experimental value of R is extracted from measurements of the cross section for deep inelastic muon scattering, as given in equation 1.2. In this equation the differential cross section, Q^2, xbj and y are measured using the scattered muon. R can be isolated by taking the ratio of the cross sections at the same Q^2 and x_{Bj} for different beam energies, because F_2 will cancel. This method has been applied in a series of precision experiments performed at SLAC.[17]

Nonperturbative effects in R are found to be largest at low Q^2 and high x_{Bj}.[17] The measured value of R from the SLAC experiments is compared to R_{QCD}, given in equation 1.12, as a function of x_{Bj} for $Q^2 = 3\ GeV^2$ in figure 2.1. R_{QCD} and R_{SLAC} diverge rapidly for $x_{Bj} > 0.02$, the kinematic region of the SLAC measurement. However, x_{Bj} is less than 0.02 for the E665 data. Thus, the region in which R_{QCD} and R_{SLAC} disagree carries very little weight in the integral of equation 2.4. In this analysis, R_{QCD} will be used, but a systematic error will be determined by comparison with R_{SLAC}.

- *The Functions Weighting F_2, and xG*

In order to evaluate the importance of experimental errors on the measurements of R, F_2, and xG, the kinematic ranges in which these functions will contribute must be considered. The weighted splitting functions (the p" functions of equation 2.3) divided by χ^2, which multiply F_2 and xG functions in equation 2.4 are: $p_q^T(zx_{Bj}/\chi)/\chi^2$, $p_q^L(x_{Bj}/\chi)/\chi^2$, $p_G^T(zx_{Bj}/\chi)/\chi^2$, and $p_G^L(x_{Bj}/\chi)/\chi^2$. These are shown as a function of χ in figure 2.2. Curves are shown for $x_{Bj} = 0.007$ and $x_{Bj} = 0.02$, the average values of x_{Bj} in the lowest and highest Q^2 bins which will be used in this analysis. The curves begin at $\chi = x_{Bj}$ because the parent must have equal or greater momentum than the quark which interacts with the virtual photon.

As will be shown below, for $\chi > 0.003$, R, F_2 and xG are relatively flat in the low χ region and drop rapidly to zero at $\chi \sim 1$. Both longitudinal functions and the transverse function associated with F_2 fall almost exponentially with a steep slope, causing the low χ regions of R, F_2 and xG to be preferentially selected. The transverse multiplier of xG does not decrease as quickly, changing by roughly an order of magnitude over the full χ range. Based on this, the discussion of R and F_2 will focus on mainly low χ, while the full χ range will be considered for xG.

- *Measuring F_2 and $G(x, Q^2)$*

F_2 is extracted from measurements of the cross section for deep inelastic muon scattering (equation 1.2) given Q^2, x_{Bj}, y and R. Many high precision experiments have been performed in order to determine F_2 and it may be considered reasonably well determined.[38]

The gluon distribution is more difficult to measure. Its contribution to deep inelastic scattering through the scaling violation of F_2 is a small effect which is strongly coupled to the choice of Λ.[39] Therefore, even with very high statistics, there is a large associated uncertainty. The gluon distribution contributes directly to the rate of J/ψ production through the photon-gluon fusion diagram. Unfortunately, the statistical significance of the present data is low and the result is dependent on the mass of the charm and a normalization factor, neither of which are well understood.[40] The cross section for direct photon production in pp scattering is directly proportional to the gluon distribution, however the

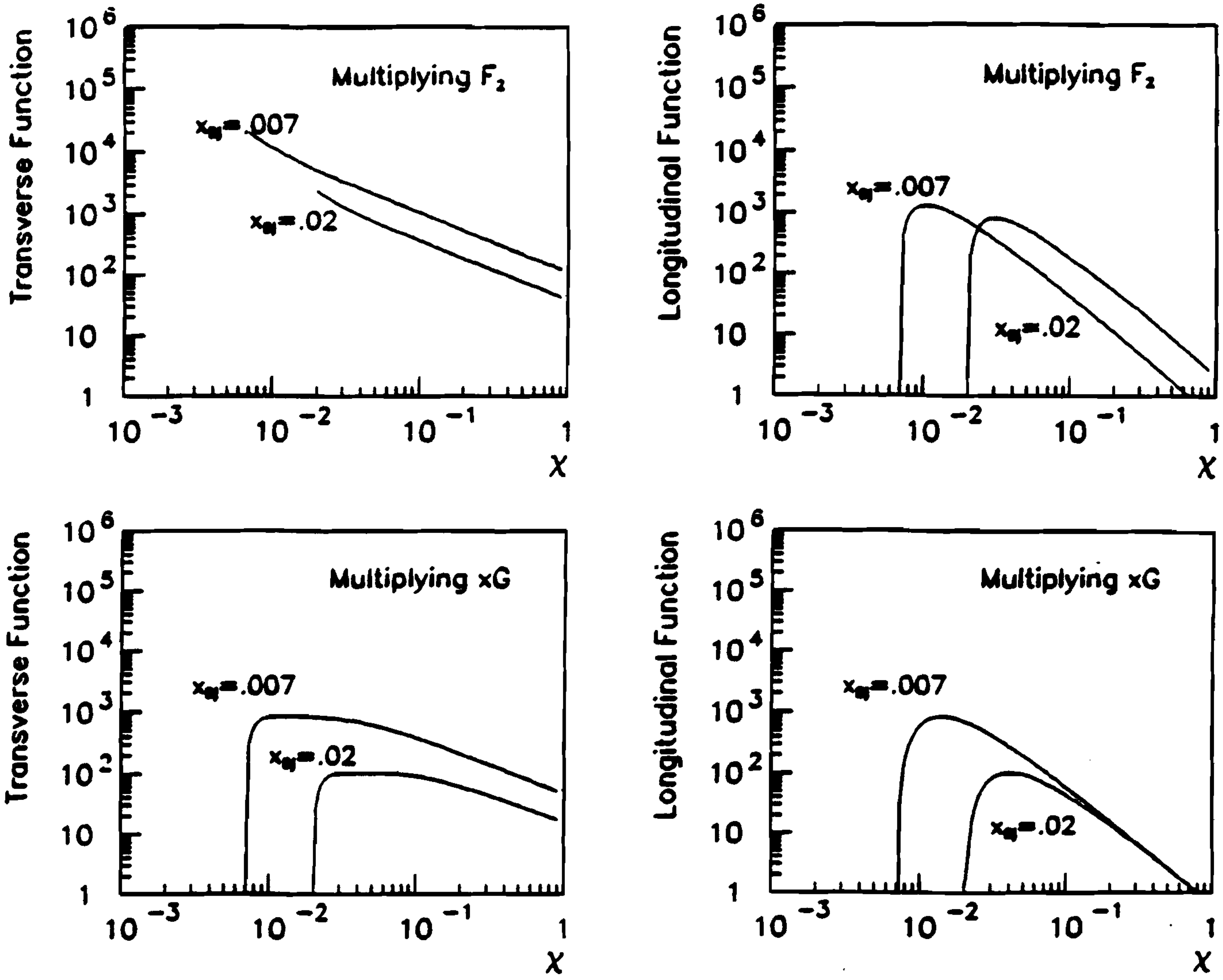

Figure 2.2. The functions $p_q^T(x_{Bj}/\chi)/\chi^2$ and $p_q^L(x_{Bj}/\chi)/\chi^2)$, the weighted splitting functions over χ^2, which multiply F_2 and xG in this analysis.

rate of production is low, isolation of photons is fraught with experimental difficulties, and there are various theoretical ambiguities over the definition of scales such as Q^2.[41] Other methods for extracting xG, including heavy flavor production, Drell-Yan production and W and Z production at the colliders, have drawbacks which make them little better than the previous three.[33] The gluon distribution extracted using scaling violations (NMC data,[39] μH_2, μD_2), J/ψ production (NMC data,[40] μH_2) and direct photon production (AFS data, [41] pp) are shown in figure 2.3a. The statistical and systematic error are added, resulting in an error of ~ ±10% for all data sets.

Global fits of F_2 and xG data from many different experiments provide parton dis-

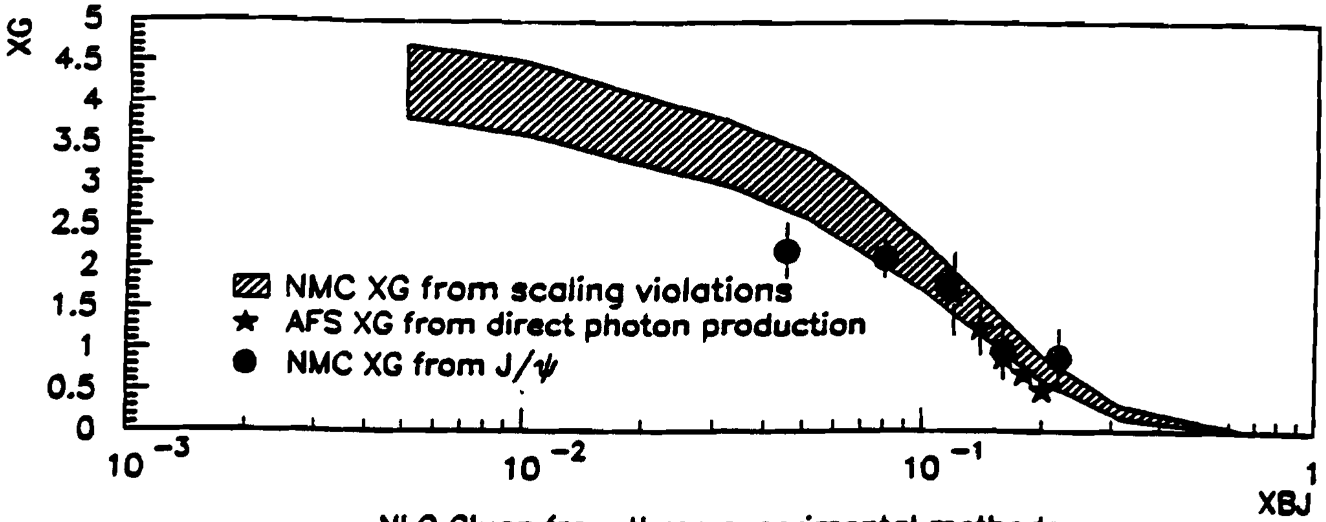

NLO Gluon from three experimental methods

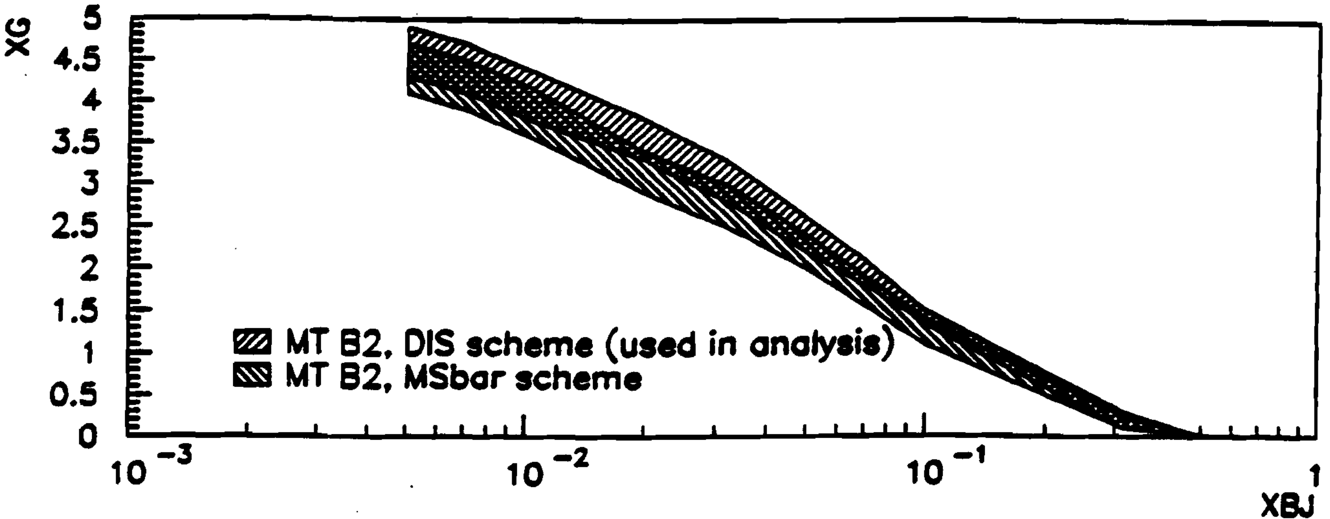

NLO Gluon defined in two schemes

Figure 2.3. Comparison of data on the NLO gluon distribution from references 39—42. The comparison is for $Q^2 = 5 - 7\ GeV^2$. **a)** The Gluon Distribution as a function of x_{Bj} in the $\overline{MS}$ scheme. Shaded region — $xG(x, Q^2)$ extracted from scaling violations in F_2 by the NMC collaboration; points — NMC J/ψ data; stars — fit to AFS direct photon data. **b)** Comparison of xG from scaling violations from the Morfin-Tung B2 fit in the $\overline{MS}$ and DIS schemes. Actual function values are at center of shaded regions. Spread of shaded regions is this author's best estimate of the sum of the systematic and statistical error.

tributions over a broad kinematic range with better understanding of systematics such as normalization and with high statistical significance. Many global fits to various data sets have been published; for fits to recent data see references 421, 431, and 441. Even within the set of global fits, there are variations in the extracted xG function depending on which data sets are included. Extrapolations of these fits into unmeasured kinematic regions are highly speculative.

To see the scheme dependence in xG, compare the Morfin-Tung "B2" global fit[42] to the BCDMS (μ scattering), CDHSW (ν scattering), CCFR (ν scattering), E288 (Drell-Yan) and E605 (Drell-Yan) data in the $\overline{MS}$ and DIS factorization schemes shown in figure 2.3b. The Morfin-Tung fits lie at the center of the shaded regions. The spread of the shaded regions is this author's best estimate of the sum of the systematic and statistical error on the fit. The region below $x_{Bj} = 0.05$ is an extrapolation of the fits. The systematic and statistical errors overwhelm the scheme dependence effects.

- *The Choice of Parameterization of F_2 and $G(x, Q^2)$*

This analysis requires parton distributions which are applicable in the kinematic range $x_{Bj} > 0.003$, $Q^2 > 3\ GeV^2$. The 1992 structure functions from the NMC[39] (μp scattering) and CCFR[45] (νFe scattering) experiments provide independent measurements in this kinematic regime. These data sets will henceforth be called NMC92 and CCFR92 data. These data extend into previously unmeasured kinematic regions of low x_{Bj} and Q^2. The results are in mutual agreement and in good agreement with the CHIO, BCDMS and SLAC data in the overlapping kinematic regions.[45]

At the time of this analysis, parameterizations which used CCFR92 and NMC92 data were not yet coded into the publicly available CERN-maintained parton distribution library (PDFLIB). [47] The parameterization used in this analysis, Morfin-Tung B2 (NLO, $\Lambda_{QCD}^{n_f=4} = 191\ MeV$), was chosen because it reproduced the NMC92 and CCFR92 sets reasonably well,[46] as demonstrated in figure 2.4. The neutrino data were corrected to the charged lepton F_2 and for nuclear effects. Morfin-Tung B2 is parameterized in the DIS scheme, which is advantageous for fast calculation of F_2 from the parton distributions. This means that for theoretical comparisons, Λ_{DIS} should be used in α_s.

A ±10% error covers the uncertainty in the gluon distribution. Therefore, for systematic studies, xG will be varied by this amount in the analysis. A ±10% is also considered for F_2 because the agreement of the Morfin-Tung B2 fit, shown in figure 2.4, is not perfect and because the measurements extend only to $x_{Bj} = 0.008$, while this analysis extends to $x_{Bj} = 0.003$.

Recalling equation 2.4 and figure 2.2, note that F_2 is an order of magnitude smaller than xG at low x, while the multiplying functions for F_2 are an order of magnitude larger than those of xG (see figure 2.2). The relative contributions of the two terms to equation 2.4 are therefore comparable.

- *Comparison of Deuterium and Hydrogen*

This analysis will make use of data sets from hydrogen and deuterium targets. Therefore, it is necessary to demonstrate that differences between the proton and neutron structure functions will not affect the analysis. The ratio of the neutron to proton cross sections

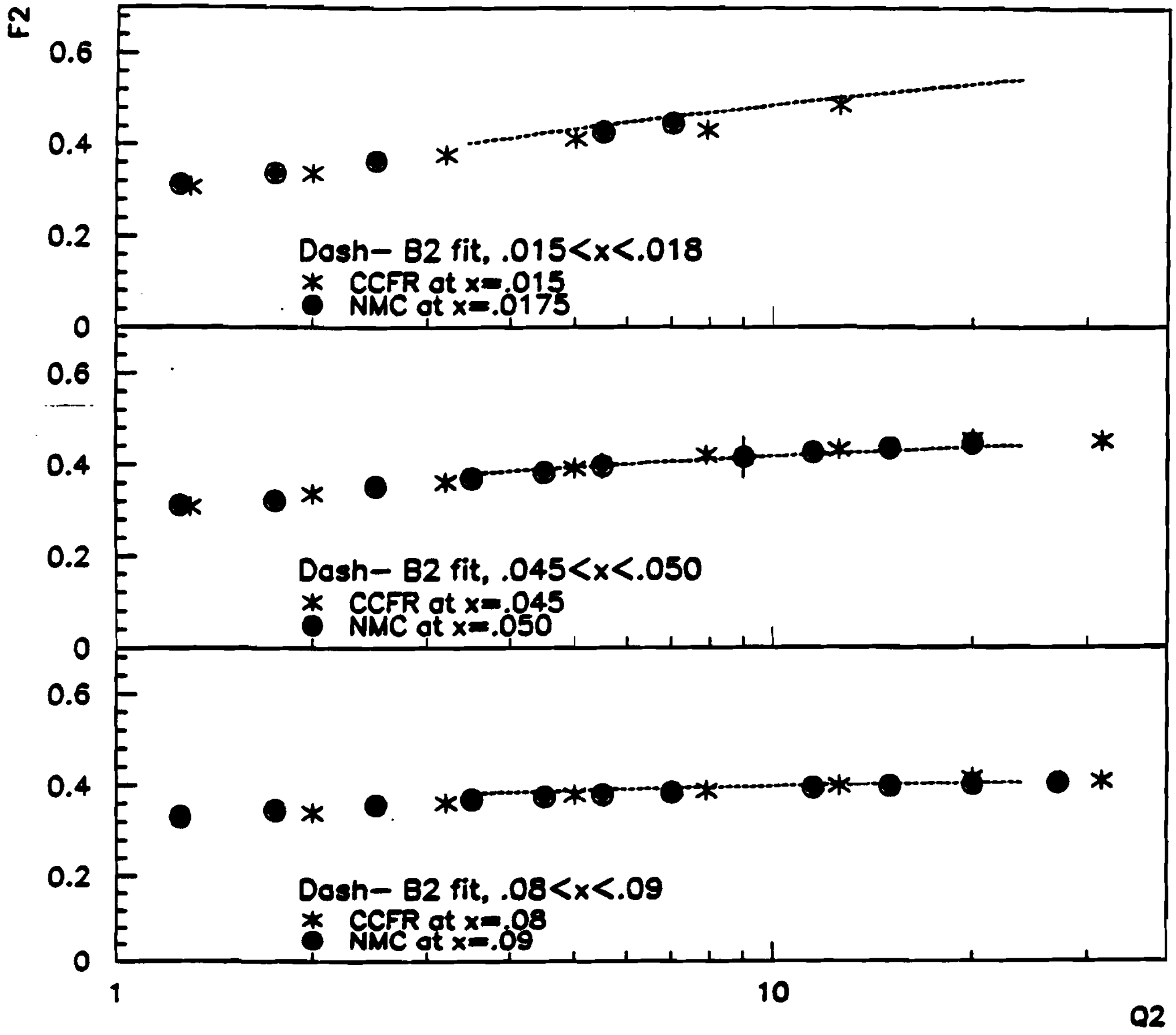

Figure 2.4. Comparison of Morfin-Tung fit B2 to the 1992 NMC and CCFR results at low x_{Bj} and Q^2. The fit is shown only in the kinematic region of this analysis.

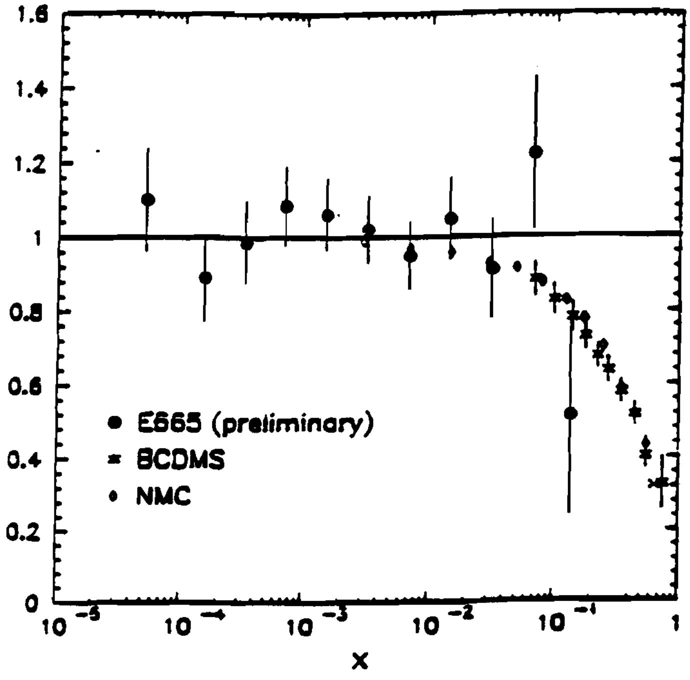

Figure 2.5. F_2^n/F_2^p for three muon scattering experiments

has been studied extensively in E665 and other experiments. [48] A summary of the data on F_2^n/F_2^p is shown in figure 2.5. At low x_{Bj}, the ratio is consistent with unity. It begins to decrease at $x_{Bj} \approx .1$ towards a value of 0.25 at high x_{Bj}. Recall that the multiplying functions for F_2 decrease much more rapidly than this (figure 2.2), effectively "selecting" only the region where $F_2^n/F_2^p \approx 1$ for significant contribution to the integral of equation 2.4.

2.3 Theoretical Expectations and Uncertainties for $\langle P_T^2 \rangle$

Figure 2.6 shows the theoretically predicted value for $\langle P_T^2 \rangle$ as a function of Q^2 (solid line in all plots), for $400 < W^2 < 800$ GeV^2, using the Morfin-Tung B2 DIS parameterization. At low Q^2, the function rises quickly, but for $Q^2 > 3$ GeV^2, $\langle P_T^2 \rangle$ vs. Q^2 appears to be linear, with a relatively small slope. Although the full Q^2 range is shown, in principle PQCD is only applicable in the region $Q^2 \gg \Lambda^2$.

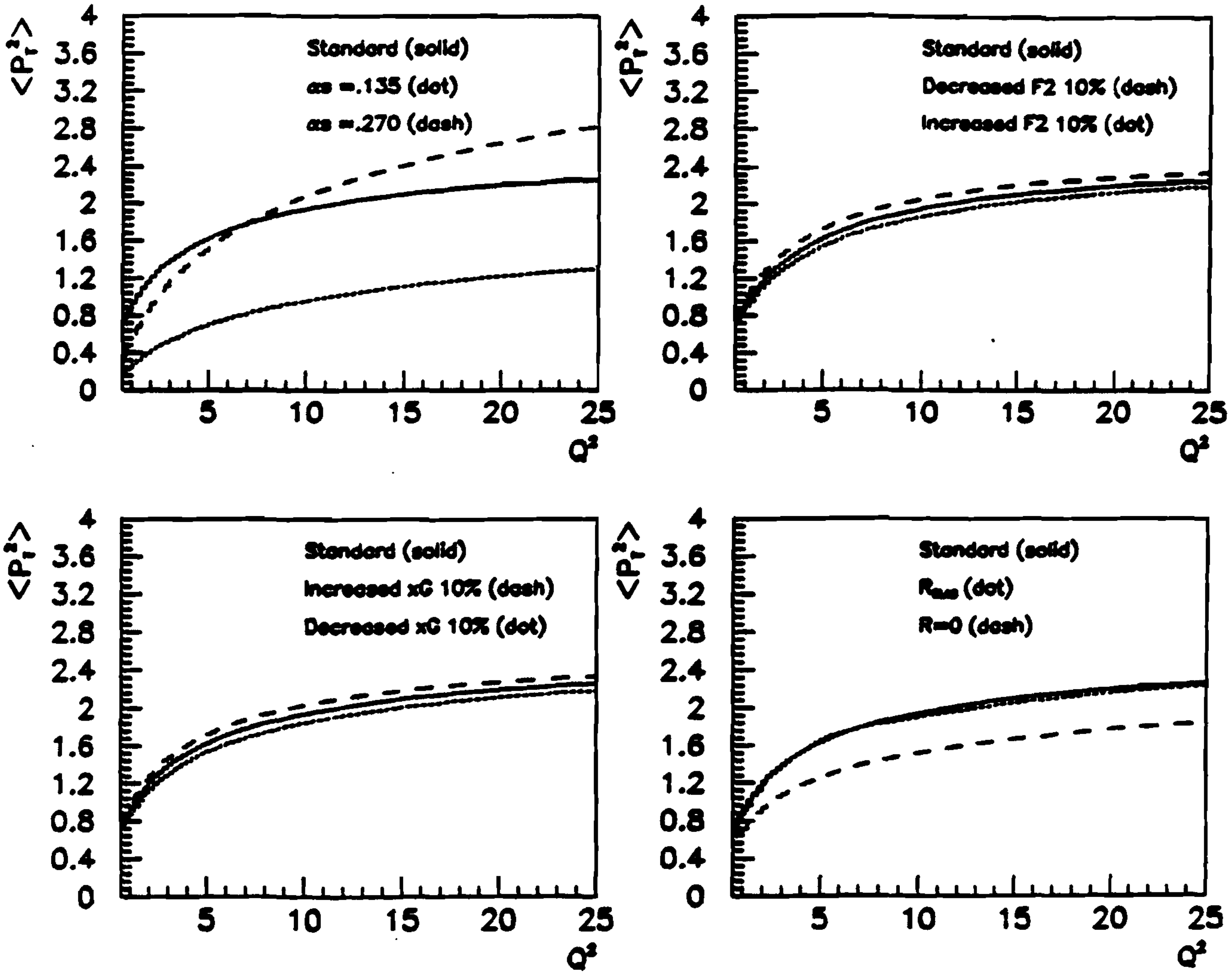

Figure 2.6. **a)** The theoretically predicted value for $\langle P_T^2 \rangle$ as a function of Q^2 (solid line); the expectation for constant $\alpha_s = 0.135$ (dotted) and $\alpha_s = 0.27$ (dashed). **b)** Theoretical predictions varying F_2: Solid— Morfin-Tung B2, Dash— F_2 decreased by 10%, Dotted — F_2 increased by 10%. **c)** Theoretical predictions varying xG: Solid— Morfin-Tung B2, Dash— xG increased by 10%, Dotted — xG decreased by 10%. **d)** Theoretical predictions varying R: Solid — $R = R_{QCD}$, Dotted — $R = R_{SLAC}$.

In figure 2.6a, the dotted line shows the expected $\langle P_T^2 \rangle$ dependence on Q^2 if α_s did not vary with Q^2. If α_s does not vary with Q^2, then one might expect its magnitude to be the average value of α_s measured by the AMY[49] ($\sqrt{s} = 50\ GeV$) and LEP[50] ($\sqrt{s} = 91\ GeV$) experiments: 0.135. The variation of the parton distributions with Q^2 is an experimental fact, whether or not one assumes α_s runs, therefore this should not be altered. $\langle P_T^2 \rangle$ is a factor of 2 lower than the standard prediction with α_s running and has a slightly steeper slope. An alternative choice is to fix α_s at the PQCD value for the average Q^2 of this analysis: $\alpha_s = 0.27$. This is shown by the dashed curve in figure 2.6. Given sufficient statistics and control of the systematic errors, a clear signal for the variation of α_s should be observed.

The dotted and dashed lines on figure 2.6b show the predicted $\langle P_T^2 \rangle$ with increased and decreased F_2 distributions; the dotted and dashed lines on figure 2.6c show the prediction with decreased and increased xG distributions. In each plot, the normalization of only one distribution was varied while the other was fixed at the standard Morfin-Tung value. The net effect is a $\sim 5\%$ overall uncertainty in both cases. In order to study the possible Q^2 dependent effects, F_2 was multiplied with a "higher twist" term of the form: $[1 + (a + bx_{Bj} + cx_{Bj}^2)/Q^2]$.[51] The best fit to the CCFR92 and NMC92 data within the kinematic range of this analysis came from $a = -0.07$, $b = 0.732$, and $c = 4.0$, respectively. The result was a 1% variation in $\langle P_T^2 \rangle$ at low Q^2 .

In the region of low Q^2 and high x_{Bj}, R has been measured to differ dramatically from R_{QCD}. As discussed above, the large x_{Bj} region is suppressed by the multiplying functions. The dotted line on figure 2.6c shows the predicted $\langle P_T^2 \rangle$ if R_{SLAC} rather than R_{QCD} is used in the analysis. Note that the longitudinal splitting functions derived for use in equation 2.4 assumed $R = R_{QCD}$, therefore, for this study these functions were multiplied by R_{SLAC}/R_{QCD}. The difference is $\sim 2\%$ with a very small Q^2 dependence. The effect of assuming $R = 0$, an historically popular but disproven choice, is shown by the dashed line.

In conclusion, the systematic uncertainty in the theoretical prediction from F_2, xG and R is on the order of 7% with negligible Q^2 dependence.

2.4 The Blueprint for the Analysis

In a world without hadronization, in order to evaluate equation 2.6, one might plan to isolate the set of 2+1 parton events, average their transverse momenta and then evaluate

$$\langle P_T^2 \rangle = \langle P_T^2{}_{2+1} \rangle \frac{N_{2+1}}{N_{1+1} + N_{2+1}}. \tag{2.7}$$

Unfortunately, the cross section for first order PQCD processes diverges for emission of partons with low momenta or at small angle, as shown in section 1.5. So, in principle,

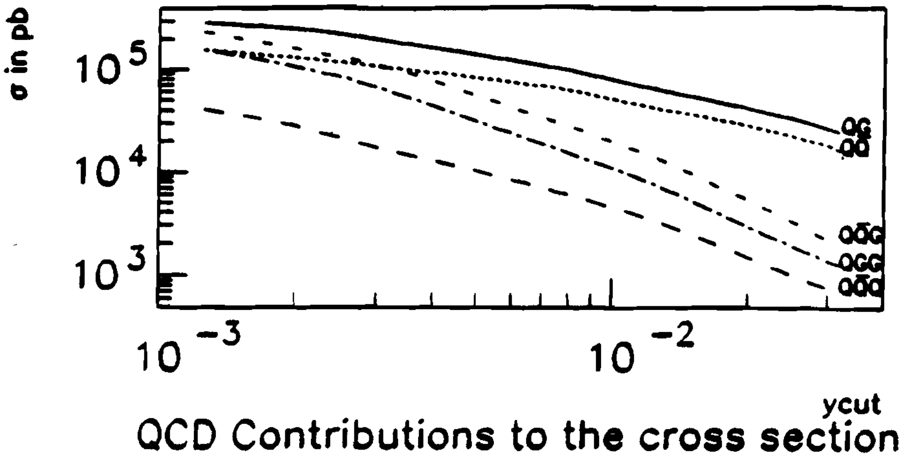

Figure 2.7. Contributions to the cross section as a function of y_{cut} for processes proportional to α_s and the external α_s^2

N_{2+1} is infinite.

The practical solution to this is to introduce a cut-off, below which an event is defined to be 1+1. There are many methods of removing infrared singularities originating from the emission of soft and collinear partons. In the "JADE" method, commonly used by theorists and described in detail in reference 20, a cut at some arbitrary value (called "y_{cut}") is made on the scaled invariant mass, $y_{ij} = m_{ij}^2/W^2$, where m_{ij} is the invariant mass of the two current partons. Soft or collinear parton pairs with invariant mass below the value of y_{cut} are treated as single entities.

The cross section for 2+1 events has been calculated as a function of y_{cut},[52] and the contributions are shown in figure 2.7. The 2+1 parton contributions are shown separately as gluon bremsstrahlung ("QG") and photon gluon fusion ("QQ"). The other contributions are from 3+1 parton processes which will be discussed further in the following section. The value of y_{cut} where an analysis is performed is arbitrary, however $y_{cut} = 0.04$ is a popular choice among theorists because the 3+1 contributions are over an order of magnitude smaller than the 2+1 parton contributions. For $y_{cut} = 0.04$, the total two parton cross section is shown as a function of $\sqrt{s}$ in figure 2.8. In the region of E665, the contributions from gluon bremsstrahlung and photon gluon fusion are approximately equal.

Applying an invariant mass cut on the outgoing partons implicitly cuts on the minimum and maximum fraction of the proton's momentum that can be carried by the incoming parton. To calculate the minimum χ, note that a cut on the outgoing parton invariant masses implicitly represents a cut on the invariant mass of the virtual photon - incoming parton system, $m_{ij\ in}^2/W^2 = (2k \cdot q - Q^2)/W^2 > y_{cut}$. Substituting $z = Q^2/2q \cdot k$,

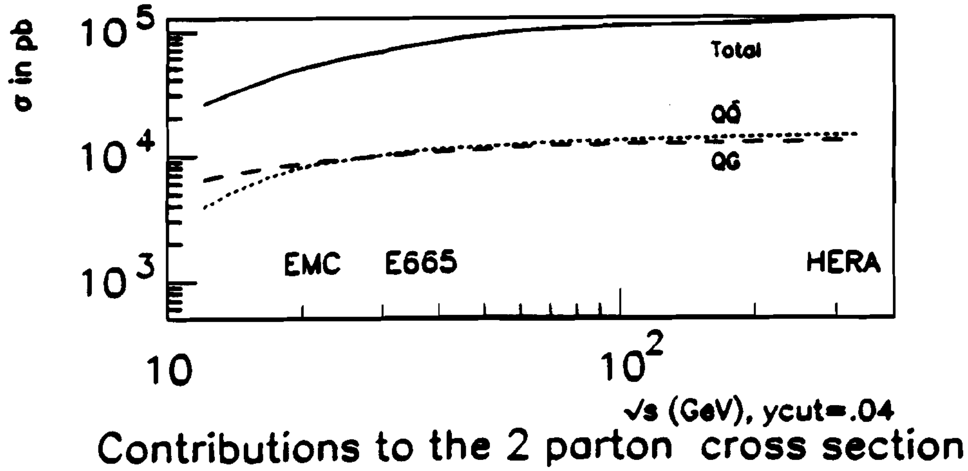

Figure 2.8. The cross section calculated to α_s as a function of $\sqrt{s}$. Past and present deep inelastic experiments are noted.

$W^2/Q^2 = 1/x_{Bj}$ for small x_{Bj}, and $\chi = x_{Bj}/z$, one finds

$$\chi > y_{cut} + x_{Bj}.$$

Note that this change in the lower limit of the integral over $f(\chi, y_{Bj}, F_2, G, p)$ is quite important if $x_{Bj} \ll y_{cut}$, the case for E665. To obtain the maximum $\chi = q \cdot p/q \cdot k$, use $2p \cdot (q + k - p) > y_{cut} W^2$. Given massless partons and using $p \cdot k/p \cdot q = (2p \cdot k + k \cdot q)/2q \cdot p - \chi/2 = (1 - \chi)/2$, one finds

$$1 - 2(1 - x) y_{cut} > \chi.$$

Because there is little contribution to the integral of f at $\chi \to 1$, this correction has little effect.

If the JADE Algorithm is used, then the numerator of the average transverse momentum becomes

$$P_T^2 \sigma_{DIS}^{NLO} = P_T^2\,{}_{2+1\;LO}\sigma_{2+1}{}_{y_{ij} < y_{cut}} + P_T^2\,{}_{2+1\;LO}\sigma_{2+1}{}_{y_{ij} > y_{cut}}$$

and the first term is defined to not contribute. Hence, with the JADE Algorithm,

$$P_T^2 \tilde{\sigma}_{DIS}^{NLO} = P_T^2\,{}_{2+1\;LO}\sigma_{2+1}{}_{y_{ij} > y_{cut}}$$

is evaluated.

In order to evaluate this, recall that the weighted splitting functions (eq 2.3) represented integrals over all $u = kp/kq$. Defining $v = y_{cut}/(1 - \chi)$, an invariant mass cut between the partons requires

$$v < u < 1 - v,$$

which, at small values of y_{cut}, will have a small effect. The weighted splitting functions have been recalculated [53] with these limits using the program *Mathematica*:

$$\begin{aligned}
\tilde{p}_q^L(z) &= \frac{4}{9}(1-z)(1-6v^2+4v^3), \\
\tilde{p}_G^L(z) &= \frac{2}{3}(1-z)^2(1-6v^2+4v^3), \\
\tilde{p}_q^T(z) &= \frac{(1-2v)}{9z}[7+2z+2v(1-v)(1+2z-6z^2)] - \tilde{p}_q^L(z), \\
\tilde{p}_G^T(z) &= \frac{1-z}{3z}(1-2v)[1-v(1-v)(1-6z+6z^2)] - \tilde{p}_G^L(z).
\end{aligned} \tag{2.8}$$

The resulting equation for the average is

$$\begin{aligned}
\langle \tilde{P}_T^2 \rangle = & \frac{\alpha_s(Q^2)}{2\pi} \frac{Q^2 x_{Bj}}{F_2(x_{Bj},Q^2)} \frac{1-y+y^2/2}{1-y+y^2/2(1+R_{QCD})} \\
& \int_{y_{cut}+x_{Bj}}^{1-2(1-x)y_{cut}} f(\chi, y_{Bj}, F_2(\chi,Q^2), G(\chi,Q^2), \tilde{p}(\frac{x_{Bj}}{\chi}, y_{cut}))dx.
\end{aligned} \tag{2.9}$$

This could be evaluated "experimentally" for a given y_{cut} in our world without hadronization,

$$\langle \tilde{P}_{T\ \text{"}exp\text{"}}^2 \rangle = \langle \tilde{P}_{T\ 2+1}^2 \rangle \frac{\tilde{N}_{2+1}}{\tilde{N}_{1+1} + \tilde{N}_{2+1}}. \tag{2.10}$$

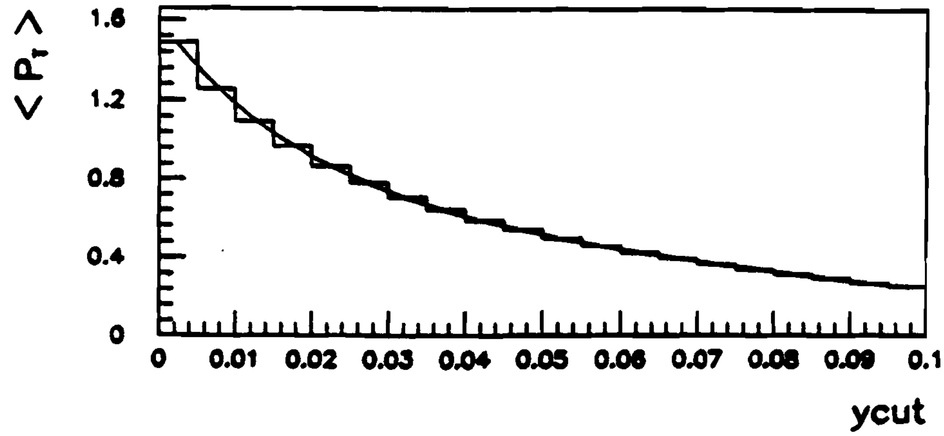

Figure 2.9. The predicted dependence of $\langle \tilde{P}_T^2 \rangle$ upon y_{cut} for $Q^2 = 4\ GeV^2$. The dependence is well fit with an exponential multiplied by a quadratic term.

The $\langle \tilde{P}_T^2 \rangle$ dependence upon y_{cut} is well fit to an exponential multiplied by a quadratic term, as shown in figure 2.9. $\langle \tilde{P}_T^2 \rangle$ decreases as a function of y_{cut} because increasing

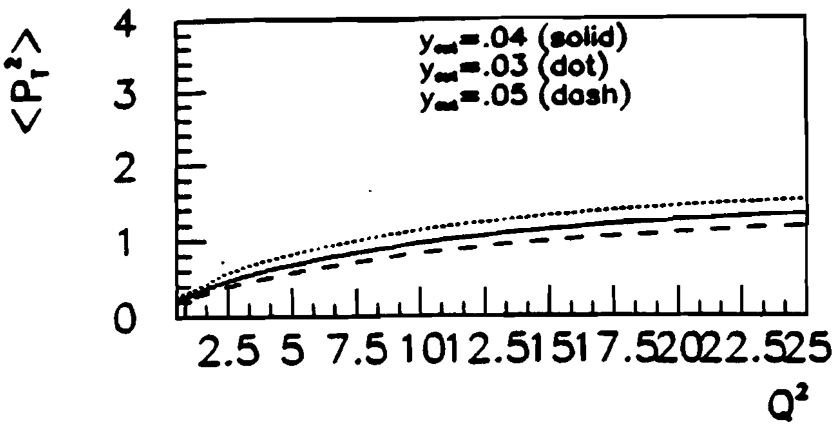

Figure 2.10. $\langle \tilde{P}_T^2\rangle$ for $y_{cut} = 0.04$ (solid), 0.03 (dot), and 0.05 (dash)

y_{cut} decreases the number of 2+1 parton events events more quickly than the transverse momentum of those events increases. The value of $\langle \tilde{P}_T^2\rangle$ asymptotically approaches $\langle \tilde{P}_T^2\rangle$ at low y_{cut}. $\langle \tilde{P}_T^2\rangle$ is evaluated as a function of Q^2 for $y_{cut} = 0.03$, 0.04 and 0.05 in figure 2.10. This predicted behavior can be tested by measuring $\langle \tilde{P}_T^2{}_{\text{``exp''}}\rangle$ at various values of y_{cut}.

Using measurements of $\langle \tilde{P}_T^2{}_{\text{``exp''}}\rangle$, the variation of $\alpha_s$ with $Q^2$ can be tested. Equation 2.9 may be rewritten in terms of $\langle \tilde{P}_T^2{}_{\text{``exp''}}\rangle$:

$$\alpha_{s\,\text{``exp''}} = \frac{\langle \tilde{P}_T^2{}_{\text{``exp''}}\rangle}{Q^2} \frac{2\pi F_2}{x_{Bj}} \frac{1}{\int_x f(\chi, y_{Bj}, F_2, G, \tilde{p})dx}. \tag{2.11}$$

Evaluating this in Q^2 bins then tests the predicted variation of α_s.

Alternatively, the distribution of $\langle \tilde{P}_T^2{}_{\text{``exp''}}\rangle$ *vs* y_{cut} may be fit in each Q^2 bin; the fit may then be extrapolated to $y_{cut} = 0$ where $\langle \tilde{P}_T^2\rangle$ (equation 2.9) is equivalent to $\langle P_T^2\rangle$ (equation 2.4).[54] This technique is only possible because $\langle P_T^2\rangle$ is not divergent. However, in chapter 7 this method will be shown to be limited by several difficulties and therefore will be used only as a cross-check of the first technique.

2.5 Higher Order Corrections

The lack of a complete calculation of the higher order contributions to the average squared transverse momentum is one of the most important uncertainties in this analysis. In order for $\sigma_{DIS} \approx \sigma_{DIS}^{NLO}$ to be a good approximation, the $O(\alpha_s^2)$ terms must be small. Also, it is important to assure that the Q^2 dependence of the neglected $O(\alpha_s^2)$ terms will not affect the conclusions of the analysis. In this section, the magnitude of the higher order corrections will be estimated based on the portions of the calculation which are available.

The external contributions to the cross section from terms proportional to α_s^2 has been calculated as a function of y_{cut}.[52,53,56] The magnitude of the external contributions to the cross section proportional to α_s^2 are shown in figure 2.7. By $y_{cut} \approx 0.04$, the 3+1 contributions are more than an order of magnitude smaller than the 2+1 terms. Therefore, $y_{cut} = 0.04$ is a popular choice for theoretical cuts in deep inelastic scattering jet calculations. Computer code for these calculations has not been completed. Graudenz has also published the calculation of the cross section through α_s^2, excluding the loop contributions, at $Q^2 = 10, 30$, and $100\ GeV^2$ According to reference 55, page 82, the contribution of the 3+1 events to the total cross section is 4% at $Q^2 = 10\ GeV^2$ and 7% at $Q^2 = 30\ GeV$. The Graudenz calculation is in the $\overline{MS}$ scheme, the parton distribution functions from Charcula[57] are used, and α_s is defined as in equation 1.7.

As an order of magnitude estimate, it should be noted that the higher order corrections to the average squared transverse momentum are expected to be smaller than those of the production cross section at a given choice of y_{cut}.[58] This is because the factor of P_T^2 preferentially suppresses the 3+1 parton events, which have lower momentum per parton. Hence, one expects the contributions to be smaller than 4—7%.

No parameterization of the Q^2 dependent correction to $\langle \bar{P}_T^2 \rangle$ is available at this time. However, Graudenz has published the α_s^2 contribution to the thrust, the total longitudinal momentum of the partons divided by total momentum, at $Q^2 = 100\ GeV^2$.[55] This author has used the thrust information to solve for the α_s^2 contribution to $\langle \bar{P}_T^2 \rangle$.

At $100\ GeV^2$, the percentage difference in the average thrust calculation with α_s and α_s^2 terms, compared to using α_s terms only, is 2%. The change is small because there are few 3+1 events and these events do not have high transverse momenta. From the thrust and the average momentum of the jets, the percentage correction to $\langle \bar{P}_T^2 \rangle$ due to the terms proportional to α_s^2 is calculated to be $< 4\%$ at $Q^2 = 100\ GeV^2$. From the plots on page 78 of reference 55, the percentage change between the two calculations of $\langle \bar{P}_T^2 \rangle$ between $Q^2 = 10\ GeV^2$ and $Q^2 = 100\ GeV^2$ is 7%. This indicates that the terms proportional to α_s^2 vary from ~ 3.7 to 4% over the Q^2 range of this analysis at $y_{cut} = 0.04$.

No calculations for the higher order corrections to the average squared transverse momentum at y_{cut} other than 0.04 are available in the literature at this time. This is an important limitation on the results extracted using extrapolations of fits to $y_{cut} = 0$.

The higher twiset terms which are proportional to powers of Λ/Q^2 have not been calculated. For $Q^2 > 3\ GeV^2$, these terms are expected to be small.

Variation of this parameter leads to changes in what is defined as a jet.

- A jet is made up of massive particles, hence $E_{jet} \neq P_{jet}$. At the parton level, even if the constituent masses of the quarks were used, $E_{parton} \approx P_{parton}$.

Having said this, one can make the following parton-jet duality hypothesis:

On Average, the jets will reflect the kinematic
properties of the underlying partons

This hypothesis has a venerable history, dating back to the original fragmentation models by Andersson, Gustafson and Peterson,[60] and by Feynman and Field.[59] Its theoretical basis has been discussed more recently in references 6, 61— 63. Using this assumption, jet rates and properties have been successfully predicted in all types of experiments where jets have been observed (see references 64—66, for example).

However, this assumption is only as good as the algorithm used to identify the jets. The purpose of the following sections is to use the E665 Monte Carlo to test the hypothesis of parton-jet duality on jets identified using the JADE Jet Algorithm, described below. In analogy with the parton level, in all following discussions, 1+1 will refer to one forward jet and one target remnant jet. A 2+1 jet event has a total of three jets, with one due to the target remnant. The target remnant jet is assumed to be the most backward-going in the CMS.

3.2 The JADE Jet Algorithm

Since the first observations of multi-jet events in e^+e^- experiments in 1979, many methods have been developed to properly assign particles to jets (see for example, references 66-68). A global comparison in reference 68 shows that for the above parton-jet duality hypothesis, all of the algorithms are approximately equally good. This analysis uses the JADE Jet Algorithm,[67] originally developed by the JADE Collaboration at DESY. This is an application, at the hadron level, of the algorithm described in the section 1.6.

The JADE Algorithm uses a recursive process in which the scaled invariant masses of particles in the event are compared to a cutoff. For each pair of particles, the invariant mass m_{ij} is calculated:

$$m_{ij}^2 = 2E_iE_j(1 - \cos\theta_{ij}). \tag{3.1}$$

The invariant mass is then scaled by the total energy in the center-of-momentum frame:

$$y_{ij} \equiv m_{ij}^2/W^2. \tag{3.2}$$

The two particles, i and j, which have the minimum y_{ij} are selected for consideration. An arbitrary parameter y_{cut} is introduced such that if

$$y_{ij} < y_{cut} \tag{3.3}$$

then the particles are assumed to belong to the same jet. The 4-momenta of i and j are added and the pair is now treated as a single "quasi-particle." The method is repeated until there are no combinations which fulfill the requirement. The number of remaining (quasi-)particles is the number of "jets" in the event.

The rate of jet production will be considered for 1+1, 2+1 and 3-or-more+1 jet events. The rate of (3+)+1 will be shown to fall quickly with increasing values of y_{cut} and in the final analysis y_{cut} is chosen such that the number of (3+)+1 jet events is negligible.

3.3 Definitions of the Transverse Momenta

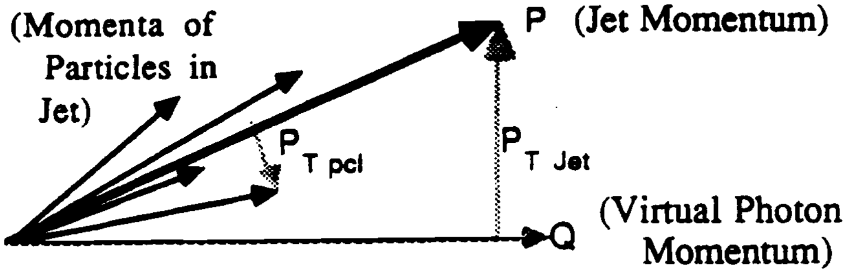

Figure 3.1. Transverse momentum of a jet.

This section defines the transverse momenta studied in the analysis of jet events. As discussed above, the (3+)+1 jet events are negligible in the final analysis. Therefore this section concentrates on 1+1 and 2+1 jet transverse momenta. First, the transverse momentum variables are defined. Next, the 2+1 case, which is actually the simplest, is discussed. Finally, the 1+1 expectations are presented. When order-of-magnitude expectations are calculated, the values from references 69 and 70 are used.

When discussing the transverse momentum, an arrow (→) indicates the vector, while absence of an arrow indicates the magnitude of the vector. All definitions below are listed in Appendix A.

If k_T were the only extra source of transverse momentum besides $P_{T\ QCD}$, then

$$\begin{aligned} \overrightarrow{P_T}_{jet\ a} &= \overrightarrow{k_T} + \overrightarrow{P_T}_{QCD}, \\ \overrightarrow{P_T}_{jet\ b} &= \overrightarrow{k_T} - \overrightarrow{P_T}_{QCD} \end{aligned}.$$

Intrinsic transverse momentum may cause the jet vectors and the virtual photon to be aplanar. If $\overrightarrow{k_T}$ and the virtual photon lie in the same plane as the 3-vectors of the two outgoing partons, the magnitude of $\overrightarrow{P_T}_{QCD}$ is recovered through equation 3.4and the magnitude of $\overrightarrow{k_T}$ is obtained through

$$k_T = \frac{(P_{T\ jet\ a} - P_{T\ jet\ b})}{2}. \tag{3.6}$$

If $\overrightarrow{k_t}$ does not lie in the plane, then equation 3.4 is only approximate. Equation 3.4 is a good approximation if $k_T \ll P_{T\ QCD}$, causing the angle out of the plane to be small. $\langle k_T^2 \rangle$ has been measured to be $(0.44\ GeV)^2 = 0.19\ GeV^2$ in previous experiments,[69] using other methods than jet characteristics. Equation 3.6 averaged over the angles of the incoming parton with the jet plane will be exact:

$$\frac{k_T}{\sqrt{2}} = \frac{(P_{T\ jet\ a} - P_{T\ jet\ b})}{2}. \tag{3.7}$$

○*Fragmentation ($P_{T\ frag}$):*

With fragmentation, the discussion moves from the parton to the jet levels. Even in the simplest fragmentation models, at least one hadron must be associated with both the forward and backward system in the CMS in order to close the color of the event. This shared daughter particle may be expected to have, on average, transverse momentum equal to $\langle P_{T\ frag} \rangle = 0.35\ GeV$.[69] As with intrinsic momentum, the distribution of fragmentation transverse momentum is assumed to be a two dimensional Gaussian.[69] The result of the fact that this particle is assigned to only one of the systems is that each will then have transverse momentum with respect to the virtual photon axis. In the 2+1 case where only fragmentation and PQCD are considered, adding this transverse momentum vector to the PQCD transverse momentum vectors results in

$$\begin{aligned} \overrightarrow{P_T}_{jet\ a} &= \overrightarrow{P_T}_{frag} + \overrightarrow{P_T}_{QCD}, \\ \overrightarrow{P_T}_{jet\ b} &= \overrightarrow{P_T}_{frag} - \overrightarrow{P_T}_{QCD} \end{aligned}.$$

The result is

$$P_{T\ 2\ jet} = \frac{(P_{T\ jet\ a} + P_{T\ jet\ b})}{2} \approx P_{T\ QCD}.$$

○*Measuring* $\langle P_{T\ frag}^2 \rangle$, $\langle k_T^2 \rangle$ *and* $\langle P_{T\ QCD}^2 \rangle$:

Based on the above discussion, a plan for measuring $\langle P_{T\ frag}^2 \rangle$, $\langle k_T^2 \rangle$ and $\langle P_{T\ QCD}^2 \rangle$ can be developed. $\langle P_{T\ frag}^2 \rangle$ can be measured from the transverse momentum of the particles with respect to the jet axis. Then, recalling the relation in equation 3.5,

$$\frac{\frac{\pi}{4}(\langle P_{T\ frag}^2 \rangle + \langle k_T^2 \rangle)}{2} = \langle (\frac{P_{T\ jet\ a} - P_{T\ jet\ b}}{2})^2 \rangle \tag{3.8}$$

may be evaluated and a value for $\langle k_T^2 \rangle$ can be extracted. The expectation for this value, given the world averages for $\langle P_{T\ frag}^2 \rangle$ and $\langle k_T^2 \rangle$, is $\langle (\frac{P_{T\ jet\ a} - P_{T\ jet\ b}}{2})^2 \rangle = 0.11\ GeV^2$.

Even if the E665 jet measurements of equation 3.8 agree with those done by other experiments using different methods, such simple interpretations should not be pushed too far. There may be other soft sources of transverse momentum in the two jet events. One thing that can be said, however, is that these measurements provide an overall order-of-magnitude estimate for the soft transverse momentum effects.

If the soft effects are small, then equation 3.4($P_{T\ QCD} = (P_{T\ jet\ a} + P_{T\ jet\ b})/2$) is expected to effectively remove most of the soft contributions, leaving all of the transverse momenta due to the underlying PQCD process in the event.

Unfortunately, two effects can drastically reduce the measured values of $P_{T\ jet\ a}$ and $P_{T\ jet\ b}$, resulting in incorrect determination of $\langle P_{T\ QCD}^2 \rangle$. These are cross talk between the jets, $P_{T\ crosstalk}$, and misidentifying a 1+1 parton event as a 2+1 jet event.

○*Cross Talk Between the Jets* ($P_{T\ crosstalk}$):

Misassigning particles in jet *a* to jet *b* results in "cross talk" between the jets. This will always decrease the magnitude of the transverse momenta of the jets. Note that again, by color closure arguments, at least one particle must be shared between the partons and, by necessity, "misassigned." Therefore, one can expect to always slightly undermeasure the transverse momentum.

In an effort to reduce misassignments, y_{cut} is chosen such that the the jets are separated. In the simple model, this would leave the mismeasurement due to the shared daughter. If the momentum should be divided equally on average then the undermeasurement of the transverse momentum squared may be expected to be of the order of $\langle P_{T\ frag} \rangle / \sqrt{2}$.

○*Contamination by Misidentified 1+1 Jet Events:*

If the jet algorithm is fooled due to some fluctuation in fragmentation leading to an apparent 2+1 structure, then obviously the measured transverse momentum in the event will not be related to $P_{T\ QCD}$. An example of such a case would be a 1+1 parton event with two high energy particles that had $y_{ij} > y_{cut}$. The algorithm would manufacture two non-remnant jets using these particles. The distribution of the transverse momentum of the particles measured with respect to the virtual photon axis falls exponentially.[72] Therefore, naively one may expect that the two fake jets in our example will have transverse momenta, $P_{T\ 1\ as\ 2}$, which are lower than the $\langle P_{T\ QCD} \rangle$ of properly identified 2+1 events.

Therefore, it is important to choose an algorithm that has good agreement between the jet and parton characteristics. The only way to test this is by Monte Carlo comparisons.

This should represent the simplest case since the Monte Carlo is designed to have the jets reflect the partons. If the algorithm fails in this case, then it is probably doomed to fail in nature. If it works, then this gives some confidence it may also work when applied to the data.

∘*Summary of the 2+1 Jet Case:*

In conclusion, if the quality of the jet-finding algorithm is good and nonperturbative effects are small, then if one defines

$$P_{T\ 2\ jet} = \frac{(P_{T\ jet\ a} + P_{T\ jet\ b})}{2}, \tag{3.9}$$

then $P_{T\ 2\ jet} \approx P_{T\ QCD} \approx P_T$.

•*1+1 Jet Case:*

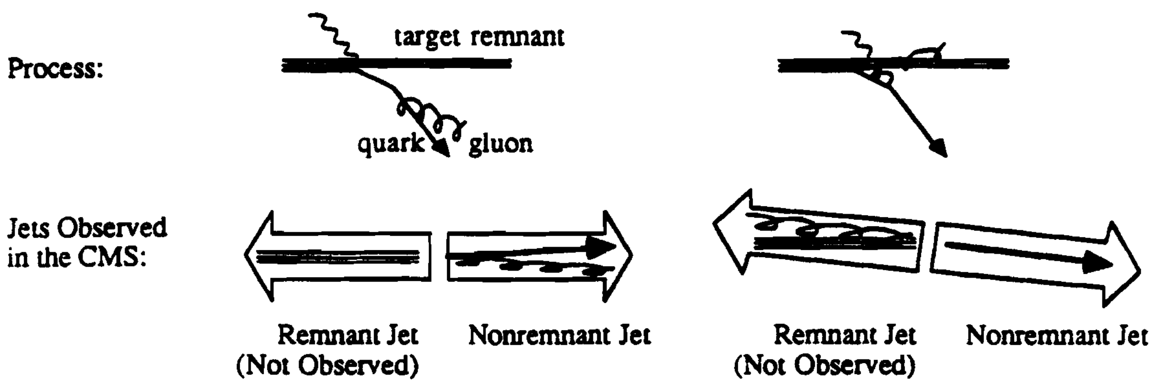

Figure 3.3. An example of 1+1 parton events which actually had very soft gluon emissions. The diagram is shown in the CMS and no intrinsic transverse momentum is considered. The dotted line shows the virtual photon axis. **a)** The gluon was emitted after the virtual photon-quark interaction, so it is in the forward direction. When the vectors of a and b are added, the resulting sum lies along the virtual photon axis. **b)** The gluon was emitted before the interaction and therefore is in the target remnant direction. Adding vectors a and c to make this a 1+1 event leads to transverse momentum of the sum and the forward parton with respect to the virtual photon axis.

The 1+1 jet case is actually somewhat more complex than the 2+1 case. This case has contributions from $P_{T\ frag}$ and k_T and also the underlying soft QCD processes in the event.

As discussed in chapter 1, at the parton level, there is no such thing as true 0th order events. All events are 2+1, but some are highly collinear or have a soft second parton. In an analysis, if y_{cut} is set to a high enough value to assure that 2+1 events are hard PQCD, then many events in the 1+1 jet set will have two underlying current partons, with one having energy just below the cut. Figure 3.3 illustrates soft gluon bremsstrahlung, where the scaled invariant mass of the struck quark and the parton were just below the cut, as an example. In the first case, the gluon was radiated after the quark was struck. The soft gluon is combined with the struck quark and there is no net transverse momentum with respect to the virtual photon axis. In the second case, the gluon was radiated before the quark was struck and is, therefore, collinear with the target remnant. Combining these introduces an apparent transverse momentum with respect to the virtual photon axis. Calling this transverse momentum $P_{T\ 2\ as\ 1}$, one would expect

$$\langle P_{T\ 1\ jet}^2 \rangle = \frac{\langle P_{T\ frag}^2 \rangle + \langle k_T^2 \rangle}{2} + \langle P_{T\ 2\ as\ 1} \rangle.$$

$P_{T\ 2\ as\ 1}$ has not been calculated, so the only statement that can be made is that the measured value of $\langle P_{T\ 1\ jet}^2 \rangle$ is expected to be larger than the measured value of equation 3.8.

Note that if E665 could reconstruct the target jet, then the transverse momentum could be measured with respect to this axis and $\langle P_{T\ 2\ as\ 1} \rangle$ would no longer contribute. The forward spectrometer data used in this analysis does not have enough backward CMS acceptance to identify the target jet axis. This will be discussed in detail in later chapters. However, the streamer chamber data, which is a subset of the events used in this analysis, has full charged particle acceptance and could be used for such a study in the future.

3.4 The Monte Carlo: Description and Caveats

A Monte Carlo simulation provides the parton/experimental-world connection, introducing: intrinsic momentum for the partons, fragmentation of the partons into hadrons, accurate representation of the muon beam, multiple scattering, secondary interactions, electromagnetic radiative corrections and decays. A Monte Carlo which has been tuned in previous experiments and reproduces the particle distributions in E665 can provide a set of "well understood" events on which one can test the quality of the jet-finding algorithm. There are several "tuned" Monte Carlo packages available, which differ mainly in the model for the fragmentation of the partons. These include the independent fragmentation model,[59] QCD cascade models,[73,74,75] and the Lund color string model.[76] The string model has been found to reproduce most accurately the results of e^+e^- and deep inelastic scattering experiments, [77] and therefore is used in this analysis.

The Monte Carlo program generates the physics interaction at the parton level, based on PQCD calculation and then fragments the outgoing partons into hadrons based on a fragmentation model. This study uses the standard Lund Monte Carlo[69] (Lepto

5.2 by G. Ingelman, Jetset 6.3 by T. Sjostrand and M. Bengtsson). Leading order parton distributions[42] were used. Two physics generators are available for use in this Monte Carlo. The first is an exact matrix element calculation based on the PQCD calculations by R. Peccei and R. Ruckl[78] and is used for the acceptance corrections in this analysis. The second is a variation on the QCD cascade model, in which incoming and outgoing partons radiate or split if there is sufficient energy for the newly created parton pair.[75] The Parton Shower model[75] is used for study of acceptance correction systematics. The Lund string fragmentation,[76] described in detail below, is applied to the final set of partons from both physics generators. The parameters of the Monte Carlo have been tuned on other experiments than E665 and were not changed from the default values. [69,70]

The beam muons for the Monte Carlo simulation are parameterizations of a random sample of muons measured in the E665 Beam Spectrometer.[79] Therefore the kinematics of the incoming muon reflect real events accurately. Electromagnetic bremsstrahlung by the muon is simulated using the GAMRAD program which is based on the radiative cross section calculations of Mo and Tsai. [80]

The Lund Monte Carlo physics generator, Lepto 5.2, uses the exact PQCD cross section calculated through terms proportional to α_s to generate events, regulating divergences with an invariant mass cut of $m^2 = 2\ GeV^2$ and a $y_{cut} = 0.0025$. In order to check the Monte Carlo parton-level output agreed with the published theory applied in section 2.4 and 2.5, comparisons of the Lund Monte Carlo code to the PQCD calculations by Brodkorb, Körner, Mirkes and Schüler[20,52] were made.[81] The following discrepancies should be noted:

1. The longitudinal term of the PQCD cross section is not included in the Monte Carlo when determining the overall event rate in each Q^2 and x_{Bj} bin. The organization of the Monte Carlo is such that this does not affect the relative fraction of production of each event type.[82]
2. In reference 20, equation 3.25a should read: $(1 + x_p^2)$; not: $(1 + x_p)^2$. Consultation with the authors confirmed that this was a typographical error.[83] After correction, the underlying matrix elements integrated over z for the calculation and the Monte Carlo agreed if the partons were assumed to be massless.
3. The use of constituent masses in the Monte Carlo leads to deviations from the massless calculation at $W < 15\ GeV$ for $x_{Bj} < 0.003$. This is outside the kinematic region of this analysis.
4. When crossing flavor thresholds in the Monte Carlo, the number of flavors in α_s is changed but Λ is not, so α_s is discontinuous. The threshold was defined as $Q^2 = m_q^2$, so this had no effect on this analysis.[82]

In conclusion, the parton-level output from the Monte Carlo physics generator agrees with the calculations presented in chapter 2 within the kinematic range of this analysis.

The Lund Monte Carlo introduces intrinsic transverse momentum (k_T) which was ignored in equation 2.4. In the calculation of 2.4, the approximation of zero intrinsic momentum was justified if $\sqrt{Q^2} \gg k_T$.[21] The value of k_T is chosen randomly according to a two dimensional gaussian, *i.e.* a gaussian in k_y and k_z.[71] $\langle k_T^2 \rangle$ is equal to the average measured value from EMC, $(0.44\ GeV)^2 = 0.19\ GeV^2$,[70] which is more than an order of magnitude smaller than the lowest Q^2 used in this analysis. It will be shown that this is also a factor of 5 smaller than the average transverse momentum of jets in the two jet events. The effect of intrinsic momentum will be studied using the Monte Carlo.

The Lund Monte Carlo hadronizer, Jetset 6.3, uses a string model to convert the generated partons to hadrons. In this method, the outgoing partons are represented by ends of a "color string" with a string constant (energy per unit length of the string) of 1 GeV/fm. As the two partons move apart, the string is stretched and potential energy is stored in the string until it breaks. The ends of the string at the break represent a new $q\bar{q}$ pair. The color of the q and $\bar{q}$ are chosen such that the string fragments will be color singlets. The q and $\bar{q}$ will have equal magnitude and opposite-sign transverse momenta with respect to the color string which broke. The magnitude of the transverse momentum is given by an exponential which has been tuned to match the fragmentation transverse momentum (measured with respect to the jet axis) observed in e^+e^- experiments: $P_{T\ frag} = 0.35\ GeV$.[70] In principle, if the invariant mass of either new string were large enough, the process would be repeated. In practice, one string is always of low enough invariant mass to be regarded as a particle, so only the other string continues to fragment. Gluons are represented by kinks in the color string. A kink may fragment leading to a gluon jet. A simple qq target remnant is fragmented in a similar manner producing at least one baryon.

However, this simple model is difficult to extend to photon gluon fusion and scattering from sea quarks. In the case of photon gluon fusion, when the target is left in a color octet state, the strings are associated to the partons according to the simplest possibility: the remaining target nucleon is divided into a quark and a diquark pair and the target remnant quark is combined with the antiquark of the pair from the gluon while the diquark is combined with the quark from the gluon. In a sea scatter, the target remnant is made up of three quarks and an extra quark (anti-quark). In this case a "primary baryon (meson)" consisting of two (one) of the valence quarks and the quark (antiquark) is created. The primary hadron is massive and on-shell. Transverse momenta of equal magnitude and opposite sign with respect to the virtual photon axis are randomly assigned using the distribution for intrinsic transverse momentum. In some cases, this results in the primary hadron kinematically isolated from the diquark fragments. In both sea scatters and photon gluon fusion, the peculiar fragmentation effects occur in the extreme backward direction. This is outside of the acceptance of the E665 forward spectrometer, used in this analysis.

The resulting particles, before decays, will be called the "Truth" data. Acceptance corrections are to the Truth level in this analysis.

The Monte Carlo particle distributions at the "Truth after decays" level are found to fit the E665 corrected forward hadron spectra well. References 12 and 14 are theses which provide in-depth confirmation of this assertion. The good agreement with the Monte Carlo reflects the fact that the problems enumerated above mainly affect absolute event production rates and not event topology. Crucially, reference 12 has demonstrated that the Monte Carlo hadron production disagrees significantly with the corrected data if the PQCD generator is not used.

The target fragmentation effects have been the subject of several theses using the E665 Streamer Chamber, which has acceptance over the full CMS. Reference 84 shows disagreements which increase with W^2 between Monte Carlo and corrected data multiplicities for $x_F < 0$. Reference 85 shows some disagreement between the predicted rapidity distributions and the corrected data. Reference 86 has shown reasonably good agreement between the rapidity and transverse momentum distributions of Λ particles in the $x_F < 0$ region.

3.5 Parton-Jet Duality from the JADE Jet Algorithm

The Monte Carlo will be used to examine the quality of the JADE Jet Algorithm. Due to the production of backward primary baryons, however, one adjustment to the JADE Algorithm is made: the primary baryon is always assigned to the target remnant jet. If this is not done, then the distributions discussed below are broadened.

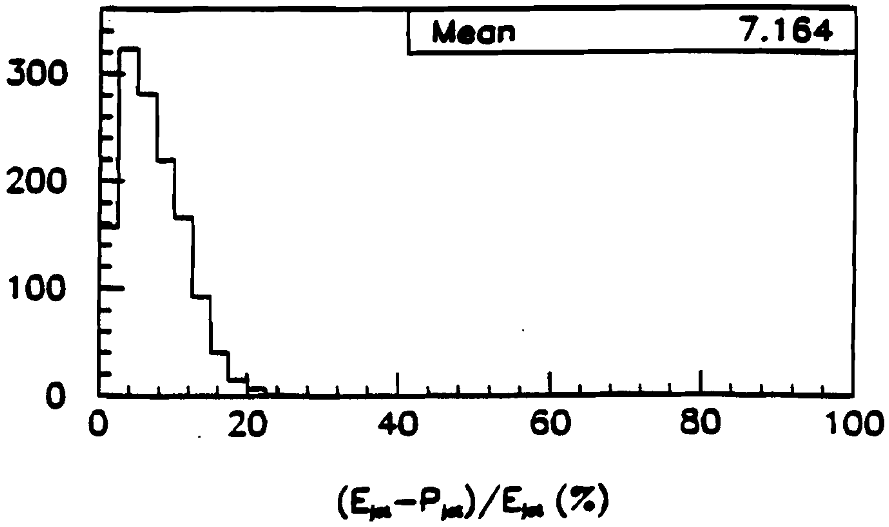

Figure 3.4. Percentage difference between jet energy and momentum.

Before comparisons can be made, the problem of "massive" jets and massless partons must be addressed.[87] At the end of the JADE Jet Algorithm procedure, each jet has a 4-vector equal to the vector sum of the particles contained in the jet. Because jets consist of massive particles, $E_{jet} \neq P_{jet}$, while at the parton level it was assumed that $E_{parton} = P_{parton}$. The traditional way to account for this error is to rescale the jet vector so that $E_{jet} = P_{jet}$ (see for example references 65, 31 or 88). Figure 3.4 shows the percentage difference between the jet energies and momenta for the Monte Carlo Truth data in the CMS frame. $(E_{jet} - P_{jet})/E_{jet} = 7\%$, represents a good estimate of the uncertainty due to rescaling the jets. For all remaining discussion, the jet vectors will be scaled.

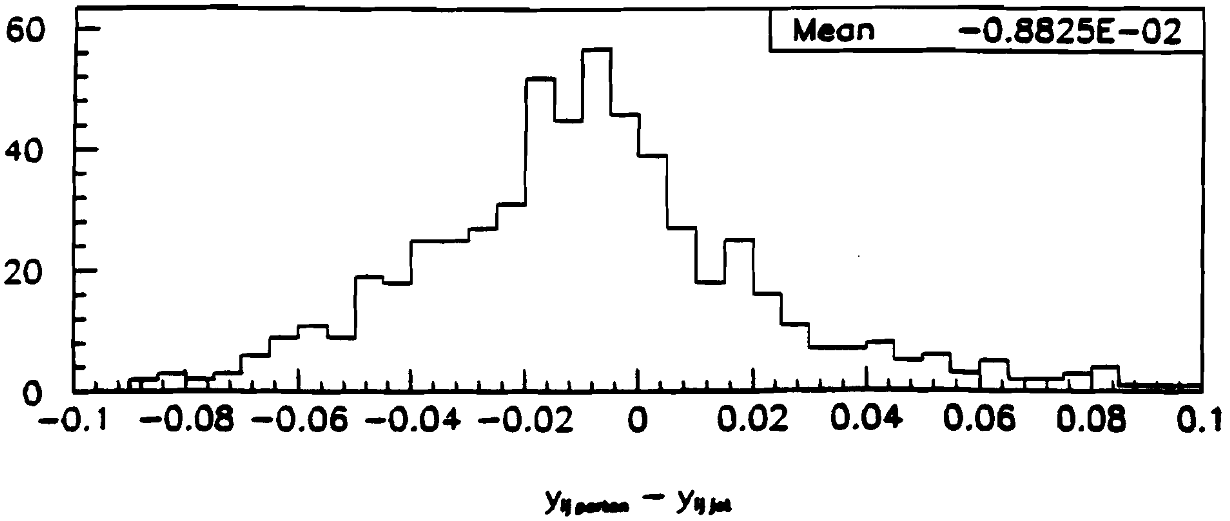

Figure 3.5. The difference between the scaled invariant mass squared y_{ij} of the underlying partons and the y_{ij} of two jet events.

The aim of this section is to demonstrate that, on average

- the y_{cut} at the jet level corresponds to some y_{cut} at the parton level,
- the jet production rate reproduces the rate of parton production at a given y_{cut},
- the angles of the jet vectors with respect to the virtual photon axis reproduce the parton emission angles, and
- the jet energies are correlated to the underlying parton energies.

Figure 3.5 shows the difference between the scaled invariant mass (y_{ij}) of the partons in 2+1 parton events and the y_{ij} at the point where the event has 2+1 jets. Recall that the Monte Carlo has invariant mass cuts which require that $y_{ij\ partons}$ be greater than approximately 0.01. The distribution is centered at approximately $\Delta y_{ij} = -0.01$. This is not surprising since the jets must have at least one shared particle. In the CMS, the shared particle energy must be approximately W/m, where m is the jet multiplicity. For forward 2+1 parton events, $E_{parton\ 1} + E_{parton\ 2} \approx W/2$ is a reasonable approximation, so the invariant mass of the jets is $\sim 2(E + W/m)(W/2 - E - W/m)(1 - cos\theta)$ while

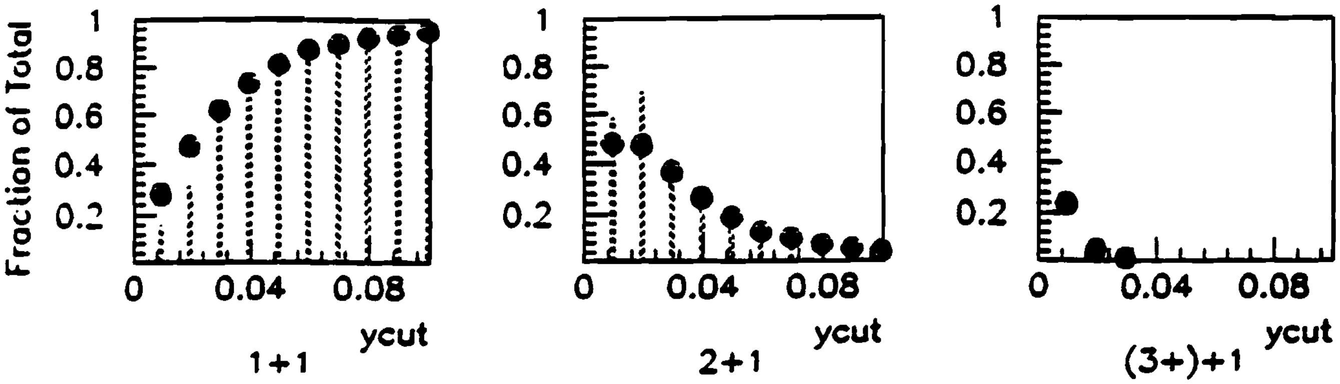

Figure 3.6. Dots: 1+1, 2+1 and 3-or-more+1 jet rates from Monte Carlo Truth vs. y_{cut}. Solid lines: the 1+1 and 2+1 parton rates. The Monte Carlo has no 3+1 underlying parton events. Note that y_{cut} at the jet level is shown on the x axis and that this is y_{cut} + .01 at the quark level (see discussion in text).

at the parton level the invariant mass is $\sim 2E(W/2 - E)(1 - cos\theta)$, where one assumes that $cos\theta_{jet} \approx cos\theta_{parton}$. Therefore $\Delta y_{ij} = -2E/Wm + 1/2m + 1/m^2$. Using typical values for E665: $W = 25\ GeV$, $m = 5$, $E = 10\ GeV$, one expects $\Delta y_{ij} \approx -0.02$. Given the approximations made above, this is consistent with the Monte Carlo predicted value: $\langle \Delta y_{ij} \rangle = -0.01$. For all further Monte Carlo comparisons, the topology for y_{cut} at the jet level will be compared to $y_{cut} - 0.01$ at the parton level.

In the analysis presented in chapter 7.1, the correspondence between y_{cut} at the jet level and y_{cut} at the parton level will be determined from the average squared transverse momentum data. The uncertainty in this correspondence leads to an uncertainty in the measured value of equation 2.11.

Figure 3.6 shows the jet rates for the 1+1, 2+1 and 3-or-more+1 jet events in the Monte Carlo Truth as a function of the y_{cut}. The 1+1 and 2+1 rates are compared to the rates at the underlying parton level using $\Delta y_{ij} = -0.01$ as discussed above. There is rather poor agreement in the two lowest y_{cut} bins, which may be due to fluctuations in hadronization. By $y_{cut} = 0.04$, there is good agreement between the Monte Carlo rates and the underlying parton rates. Furthermore, by $y_{cut} = 0.04$, the 3-or-more+1 events contribute very few events. In this analysis, $y_{cut} = 0.04$ will be used, with $y_{cut} = 0.03$ and 0.05 used to estimate systematic error.

Note that given the requirement $W > 20$ used in this analysis, a $y_{cut} = 0.04$ implies a minimum invariant mass of the jets of $m_{ij} = 8\ GeV$. This is comparable to the minimum cut used in the jet analyses by PETRA experiments of $m_{ij} = 7\ GeV$ and is sufficiently high to make the analysis insensitive to fluctuations from hadronization.[89,90]

Based on these studies, one may conclude that the $y_{cut}^{partons}$ used in the integral for the transverse momentum calculation (equation 2.9) may be taken to be $y_{cut}^{jets} - 0.01$. The effect of this assumption will be studied in the section on "Jets Analysis."

Figure 3.7 compares the angular dependences of the jets and partons. Recalling figure 3.2, θ is the angle between the jet and the virtual photon axis projected into the jet plane

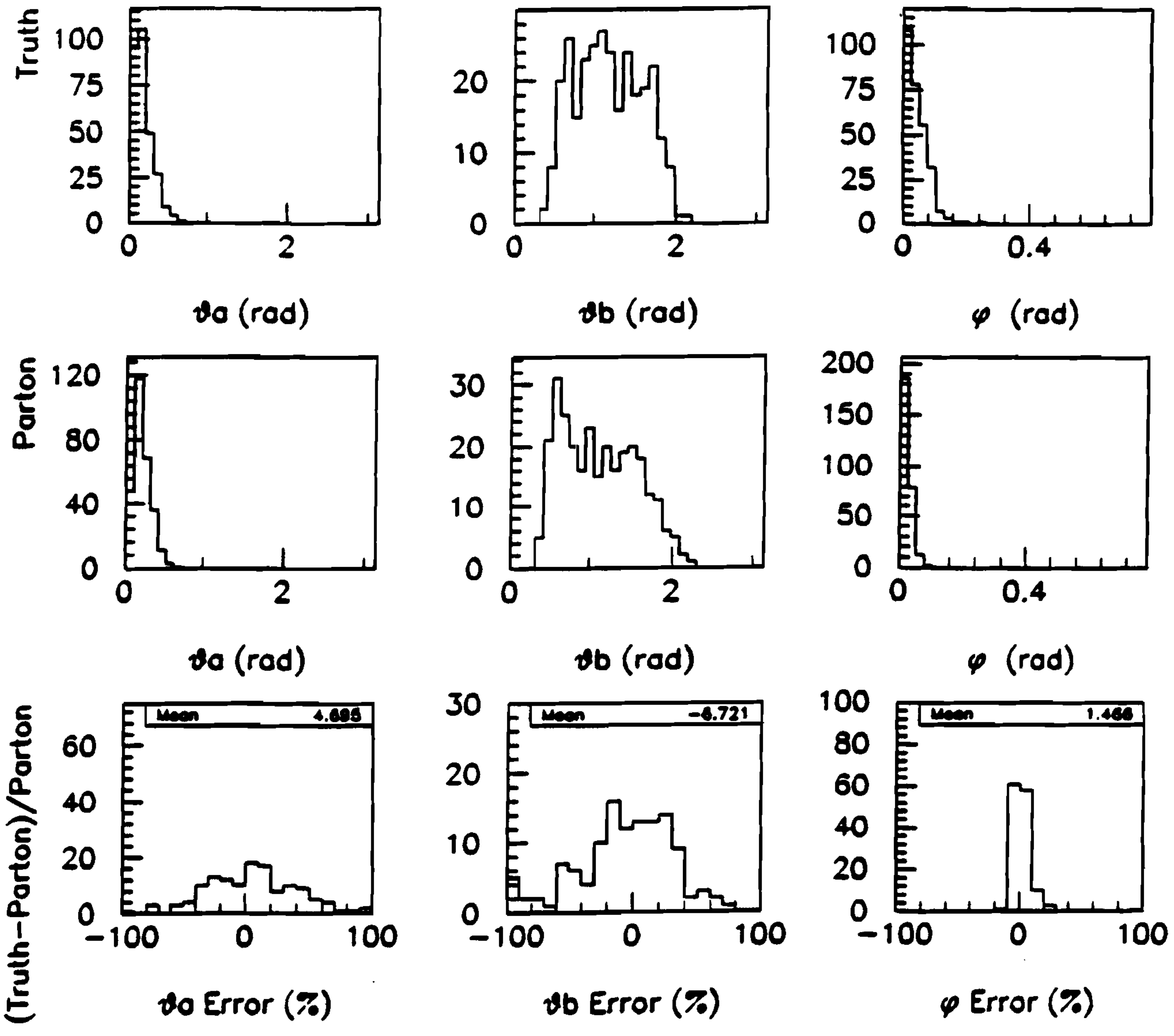

Figure 3.7. Comparison of the angles between the jets and the projected virtual photon axis (θ on figure 3.2) and the jet plane and the virtual photon (ϕ). For each, the Truth jet angle, the parton angle and the percent error between the two are shown.

and ϕ is the angle between the jet plane and the virtual photon vector. Jet a is always the highest momentum non-remnant jet or parton and b is the other non-remnant jet or parton. The columns show θ_a, θ_b and ϕ for 2+1 jet events. The rows represent the Truth jets, the partons, and the percentage difference between the truth and jet levels. For parton-jet duality to hold, the percentage difference must be centered on zero, which can be seen to be true.

Furthermore, parton-jet duality implies that on average the energy of the jets are reconstructed properly and therefore the transverse momenta of the partons will be properly reproduced. Figure 3.8 shows the distributions and percentage differences between the Truth jet and parton level for the energy and transverse momentum. Because most 2−1 events have one parton which is more energetic than the other, the energy distributions show a two peak structure. Note that the transverse momentum of the partons and jets is on average a factor of 5 larger than the intrinsic transverse momentum. The difference distributions are centered on zero, indicating that parton-jet duality holds at least within the Monte Carlo models favored by deep inelastic scattering Data.

A final test of parton-hadron duality in the JADE Jet Algorithm comes from extracting the combined fragmentation and intrinsic transverse momentum. According to equation 3.8:

$$\frac{\frac{\pi}{4}(\langle P_{T\ frag}^2\rangle + \langle k_T^2\rangle)}{2} = \langle(\frac{P_{T\ jet\ a} - P_{T\ jet\ b}}{2})^2\rangle$$

which is expected to be equal to 0.11 GeV^2 given the Monte Carlo inputs, if the assumptions made concerning the jets in section 3.3 are correct. The Monte Carlo Truth distribution, shown in figure 3.9, has a mean of 0.09 GeV^2 which is in reasonably good agreement with the expectation.

In conclusion, the JADE Jet Algorithm identifies jets which, on average, reflect the characteristics of the underlying partons in the event in the Monte Carlo. This algorithm will be used in this analysis.

3.6 From Here to the Analysis

The E665 data provide the first opportunity to test the Parton-Jet Duality Hypothesis in deep inelastic scattering. In order to do this, the experiment and data set must be considered in detail (chapters 4 and 5). Then the algorithm may be applied and compared to the expectations at the parton level (chapter 6).

If the jets provide a window to the parton level, then the theory of chapter 2 may be tested at the jet level. The analog to equation 2.10, which gave the transverse momentum squared averaged over *all (not just 2+1)* parton events in an experimentally measurable

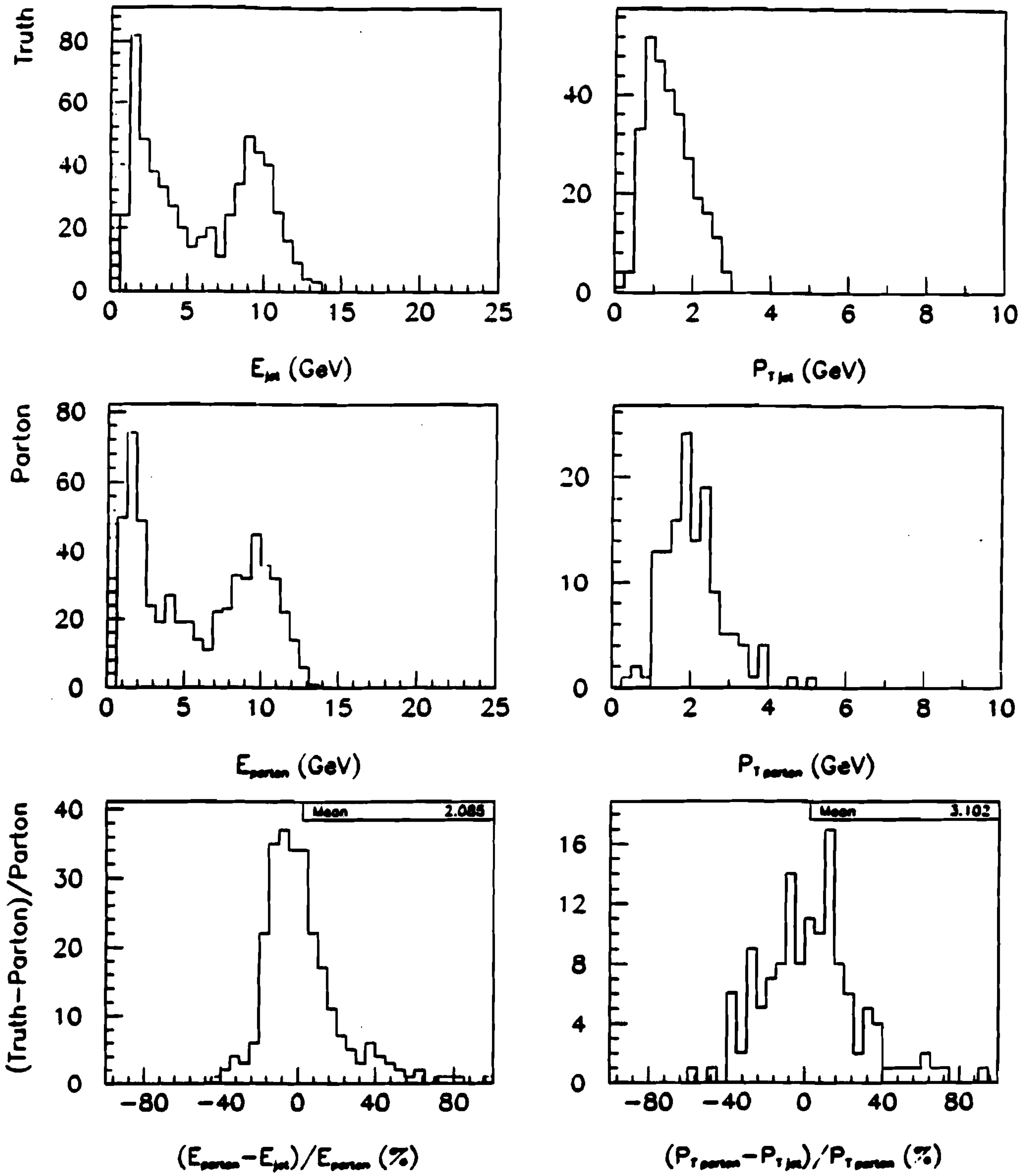

Figure 3.8. a) Comparison of the energies of jets to partons. b) Comparison of the transverse momenta of jets to partons. Percentage differences given by (Truth−Parton)/Parton are shown.

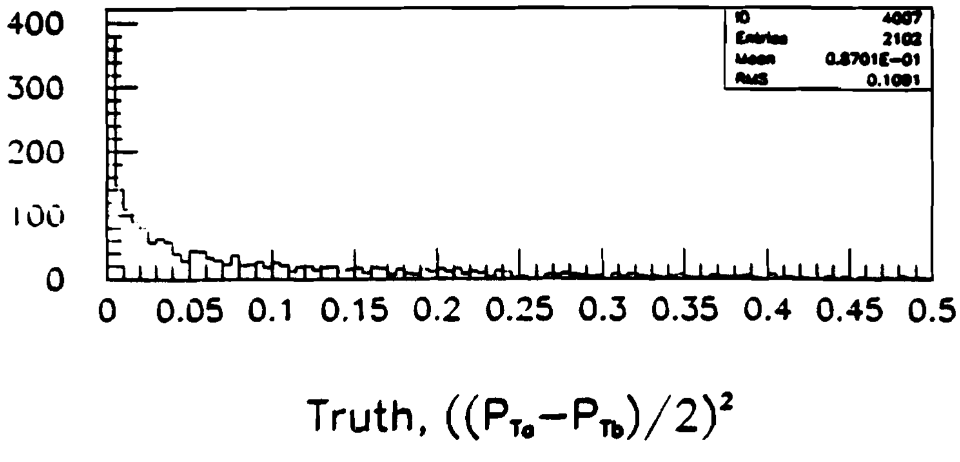

Figure 3.9. Monte Carlo Truth prediction for $[(P_{Tjeta} - P_{Tjetb})/2]^2$. The average was predicted to be 0.11 GeV^2 from section 3.3

form is

$$\langle P_{T\ all}^2 \rangle = \langle P_{T\ 2\ jet}^2 \rangle \frac{N_{2+1\ jet}}{N_{1+1\ jet} + N_{2+1\ jet}}. \tag{3.10}$$

This may be compared to the expectations of equation 2.9, keeping the theoretical uncertainties associated with R, F_2, xG and the connection between y_{cut}^{parton} and y_{cut}^{jet} in mind. Finally, the analog of equation 2.11 can be evaluated:

$$A = \frac{\langle P_{T\ all}^2 \rangle}{Q^2} \frac{2\pi F_2}{x_{Bj}} \frac{1}{\int_x f(\chi, y_{Bj}, F_2, G, \bar{p}) dx}. \tag{3.11}$$

Alternatively, $\langle P_{T\ all}^2 \rangle$ as a function of y_{cut} can be extrapolated fit to $\langle P_{T\ all\ y=0}^2 \rangle$. This eliminates the question of the correspondence between y_{cut} at the jet level and y_{cut} at the parton level. Unfortunately, this method requires high statistics over a broad range of y_{cut} values and a jet algorithm which successfully reflects the underlying partons at low values of y_{cut}. In chapter 7, it will be shown that interpretations from this technique are limited by the statistics of the E665 Run87 data. Nevertheless, this method is useful as a cross-check.

In summary, in chapter 7 the data will be used to test the following PQCD predictions:

1. the y_{cut} dependence of $\langle P_{T\ 2\ jet}^2 \rangle$ is described by equation 2.9.
2. A is equivalent to α_s with the variation predicted in equation 1.7.

Chapter 4

Experiment 665

The data presented in this thesis were collected during the 1987–88 running period of Experiment 665, deep inelastic muon scattering, at Fermilab. The data used here result from scatters from the hydrogen and deuterium targets.

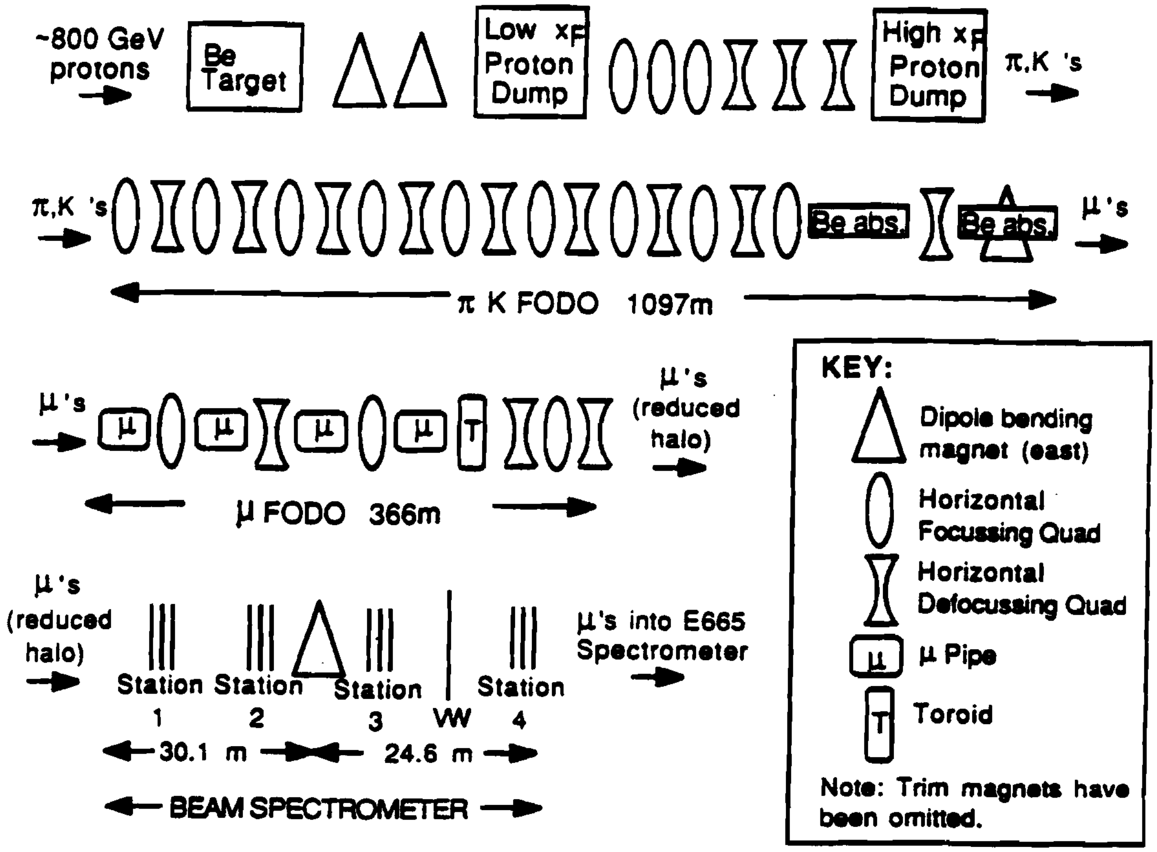

Figure 4.1. The Tevatron Muon Beamline and the Beam Spectrometer.

The purpose of this chapter is to describe the process of obtaining the events, collecting information from the apparatus, reconstructing the particles in the event and producing a final data set for input into this analysis. It provides definitions of terms related to the experiment which will be used throughout the remaining chapters. Only short descriptions of the portions of the experiment relevant to this analysis are presented. Extensive descriptions of all aspects of Experiment 665 are available in references 12-84 and 91-100. This author's contribution to the apparatus is largely related to Run90-91 data, not available for this analysis, and is documented in reference 101. A short overview of the apparatus is provided in reference 102.

This chapter provides:

- Overview of the apparatus and software.
- Description of the muon beamline.
- Description of the beam spectrometer.
- Description of the vertex spectrometer.
- Description of the forward spectrometer.
- Description of the scattered muon detectors.
- Discussion of data reduction.

The resulting data set is examined in detail in chapter 5.

4.1 Overview

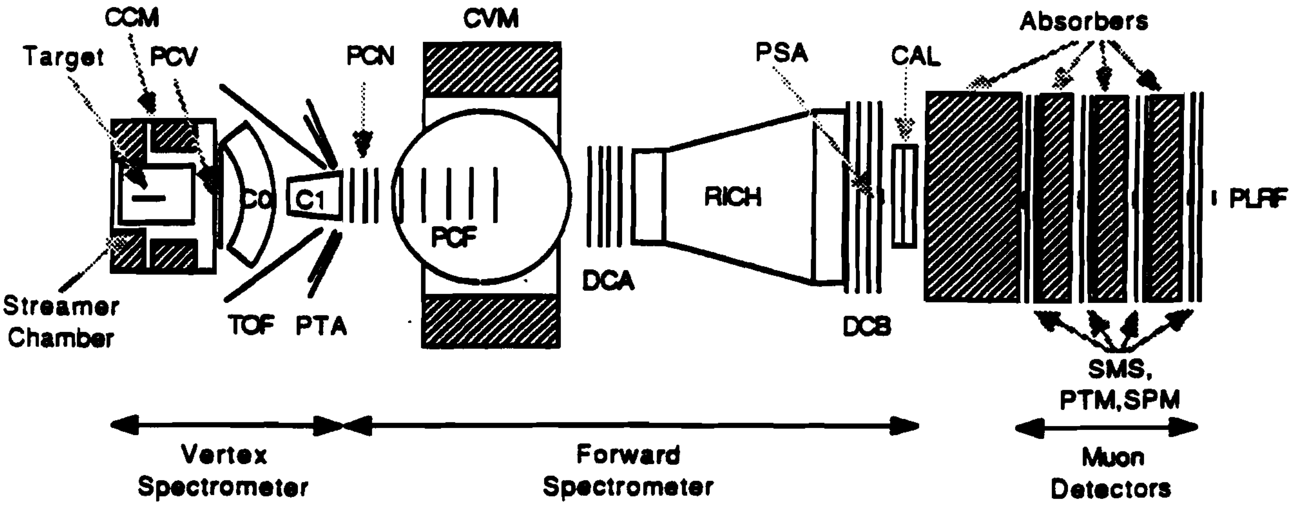

Figure 4.2. Plan view of the Vertex and Forward Spectrometers and Muon Detectors

The E665 apparatus consists of 5 sections: the beamline, the beam spectrometer, the vertex spectrometer, the forward spectrometer and the muon detectors. The first two sections in figure 4.1, the remaining three are shown in figure 4.2. Each spectrometer consists of tracking and particle identification chambers and dipole magnets.

The E665 coordinate system is right-handed with X along the beam axis.

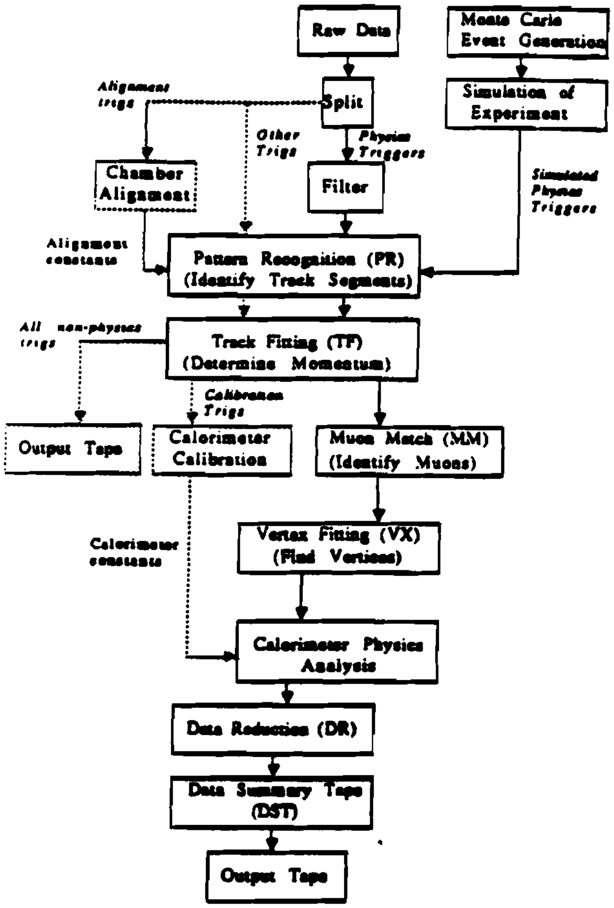

Figure 4.3. Flow chart of the E665 Code.

Muons are produced in the beam line, then travel through the beam spectrometer which provides 0.5% momentum resolution.[100] The incoming muons are incident on a target located within the vertex spectrometer magnet. The scattered muon and the particles produced in the interaction are detected in the vertex and forward spectrometers and stopped in the hadron absorber at the back of the experiment. The resolution on the momentum of the tracks measured in the forward and vertex spectrometers is given

Table 4.1. Tracking Detectors.

Tracking Detectors used in this Analysis

Name	Purpose	Type	Views in Packages	Num. Pkgs	Position of Packages	Anode Construction	Wire Spacing	Cathode Type	Active Region	Gas Mixture	Electronics/ Readout	Efficiency (ref. 82)	Refs
PBT	Beam Muon Reconstruction (PR/TF)	Prop	U,Z,Y,V,Z',Y'	4	Beam Spectrometer (Surrounding NMRE)	10 μm gold plated Tungsten	1 mm actual, 0.5 mm, effective for Y, Z	Mylar coated foil	12.8 cm (Y) 12.8 cm (Z)	Argon-Ethane	NAN-N277 pre-amp & discrim; PCOS readout	Typical: 92% PBT1V: 68%	82,83,88 92, 93
PCV	Upstream Anchor for tracks (PR/TF)	Prop	Y, U,U',V,V',Y'	1	Immediately Downstream of CVM	20 μm gold plated Tungsten	2 mm	Graphite coated Mylar on Rohacell planes	2.8 m (Y) 1.0 m (Z)	Argon-Iso-butane-Freon	Custom designed electronics with CAMAC readout	Typical: 85% PCV2Y: 50%	82,85, 88,94
PCN	Track segment before CCM (PR/TF)	Prop	Y,Z,U,V	3	Immediately Upstream of CCM	20 μm gold plated Tungsten, with attached support wires	3 mm	Graphite on mylar, 3 regions per foil, 5 foils per pkg	2.0 m (Y) 2.0 m (Z)	Argon-Iso-butane-Freon	RMH digitization housed in CAMAC	Typical per package: 94%, 91%, 82%	82,83,88
PCF	Tracking through the CCM (PR/TF)	Prop	Z,U,V	5	Within the CCM gap	20 μm gold plated Tungsten, with attached support wires	2 mm	Aluminized Kapton glued to Styrofoam backed by Mylar	2.0 m (Y) 1.0 m (Z)	Argon-CO2-Freon	NAN-N810 discriminator; NAN-WCS300 scanners; CAMAC readout	Typical: 91%	68,84,88
DC	Track segment after CCM (PR/TF)	Drift	Z,Z',U,U' V,V',Z,Z' (Z planes consist of 2 half-panes)	2	One Package (DCA) after CCM, other (DCB) just upstream of hadron absorber	20.3 μm gold plated Tungsten, with attached support wires	50.8 mm spacing (placement precision: 100 μm)	Cathode & Field Shaping wires: 102 μm, set 9.6 mm from anode	Package 1: 4.0 m (Y) 2.0 m (Z) Package 2: 6.0 m (Y) 2.0 m (Z) Central hole: 10 cm (Y) 5 cm (Z)	Argon-Ethane	NAN-N311 discriminator; MUTES encoding, CAMAC readout	Typical: 95%	82,85,88
						Operation: 492 V/cm Drift Velocity: 4.2 cm/ μs Drift time 500 ns Resolution: < 400 μm							
PSA	Cover Dead Region of DC's (PR/TF)	Prop	Z,Y,Z',Y', U,V,U',V'	1	In front of DCB	10 μm gold plated Tungsten	1 mm actual, 0.5 mm, effective for Y, Z	Mylar coated foil	12.8 cm (Y) 12.8 cm (Z)	Argon-Ethane	NAN-N277 pre-amp & discrim; PCOS readout	Typical: 84% PSA1U1 during D2 running: 0% PSA1V2: 65%	79,88,92
PTM	Detection of outer scatt mu (PR only)	Prop	Y,Z	4	Behind absorber	50 μm gold plated Tungsten	1.27 cm	2.54 cm sq aluminum tubes	7.2 m (Y) 3.6 m (Z) Central hole: ~12 cm sq.	Argon-Ethane	NAN-N272E amp. & disc.; NAN-WCS200 scanner; CAMAC readout	Typical: 95%	55,82,88
SMS	Detection of inner scatt mu (PR only)	Hodo-scope	Y,Z	4	Behind absorber, covering PTM hole	NE110 scintillator	1.32 cm finger width	N/A	20.0 cm (Y) 20.0 cm (Z)	N/A	HAM-R1166 phototubes; LRS4416 disc; LRS229 ADC's LRS448 Latch; CAMAC readout	Typical: 98% (counters were >99%, loss was due to latch ineffic.)	83,88

by $\langle dp/p\rangle = (24 + 0.79P + 121/P) \times 10^{-4}$. The scattered muon travels through the steel absorber and through four sets of muon detectors which are separated by concrete. Information on the tracking detectors for the incoming muons, hadrons and outgoing muons is summarized in table 4.1. The purpose, construction, uncorrelated efficiencies (from reference 96), and useful references on both construction and performance are provided.

The information from the detectors is written to tape if an event satisfies the trigger requirements in both the beam spectrometer and muon detectors. Details on the components of the triggers are given in table 4.2. The trigger logic is discussed below. The physics triggers used in this analysis required incoming and outgoing muon signals, but made no forward spectrometer requirements.

Trigger Components

Category	Name	Position	Use in Triggers	Further Information
Magnets	NMRE	Beam Spectrometer	Momentum selection of incoming muons	Field: 51KGm, Stable to <1%
	CVM	Vertex Spectrometer	CCM and CVM are set to focus muons to the position of the unbent trajectory at approx SPM1	Field: -15 KG (pathlength depends on vertex pos.)
	CCM	Forward Spectrometer		Field: 127 KGm (13.8 KG)
Muon Detection Hodoscopes	SBT	Beam Spectrometer; arranged in 4 packages around NMRE	Identify incoming muons	Material: NE110; Phototube: HAM-R1398 Construction: 13 fingers (Y); 13 fingers(Z); Active Area: 18 cm (Y); 14 cm (Z) Discrim: LRS4416, Latch: LRS4448; ADC: LRS2249
	SPM	Muon Spectrometer; in 4 packages	Identify outgoing muons (LAT only)	Material: ROHM GS2030 scint; GS1919 waveshifter Phototube: HAM-R329, custom bases discriminate Construction: 15 fingers in two rows, central hole Active Area: 7 m (Y); 3 m (Z), with hole Latch: LRS4448; ADC: LRS2249
Muon Veto Hodoscopes	VJ (Jaws)	Beam Spectrometer; 3 packages on stations 2-4	Veto close halo	Material: NE110; Phototube: RCA8575 Construction: 2 jaws which can be adjusted to vary hole as shown: Active Area: 3m (Y), 2m (Z), with hole. Disc: LRS4416;Latch: LRS4448; ADC: LRS2249 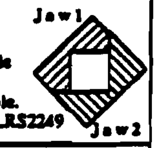
	VW (Wall)	Beam Spectrometer;	Veto wide halo	Material: NE110; Phototube: RCA8575 Construction: 2 walls; 14 fingers, 2 rows each separated by 1.3 cm iron wall Active Area: 7 m (Y); 3 m (Z), with hole Disc: LRS4416;Latch: LRS4448; ADC: LRS2249
	SMS	Muon Spectrometer, 4 packages, one in each SPM bay, covering SPM hole	Veto Unscattered Muons SMS 1 or 4 -- LAT trigger SMS 1 or 2, (subset of fingers) - SAT Trigger	Material: NE110; Phototube: HAM-R329 Construction: 16 fingers (Y); 16 fingers (Z) Active Area: 20 cm (Y); 20 cm (Z) Disc: LRS4413;Latch: LRS4448; ADC: LRS2249
Accelerator RF phase locking	PLRF	Behind the E665 Detectors	Provides reference signal synchronized to accelerator RF	Signal source phase locked to arriving muons. incoming muon signal detected by four 5.08x5.08x1.27 cm NE110 with RCA8575 & HAM-R329 phototubes in 4-fold coinc.; time shift tracking rate: 300 ps/arriving muon

Table 4.2. Trigger Components

Figure 4.3 provides a flow chart of the E665 code used to reconstruct events. The events were initially split according to trigger type. A filter which required reconstructed incoming and outgoing muons and at least one track in the forward spectrometer was applied to the physics triggers.[103] The four main components of the event reconstruction chain are Pattern Recognition (PR), which finds track segments in the detectors, Track

Fitting (TF), which determines the track momenta, Muon Matching (MM), which identifies the muon tracks, and Vertex Fitting (VX), which finds the scattering vertex and any decay vertices. For discussion of philosophy and performance of each of these programs, see references 96, 97, 92 and 98, respectively. Particle identification code is applied to the data after VX. Then the data set is reduced through event requirements (DR), (see reference 104) and put into a summary (DST) format. The DST tapes are the input to this analysis.

4.2 The Beamline

The high intensity muon beam is produced by colliding protons with a target, allowing the resulting pions and kaons to decay, and focussing the resulting muons. The Proton Targeting Devices focus 800 GeV protons from the Tevatron accelerator onto a 48.5 cm long beryllium target. The noninteracting protons are directed into beam dumps while the secondary particles from the interaction are bent into the 1.1 km π/K decay channel tuned to 480 GeV. Approximately 5% of the pions decay before the 11 m Beryllium absorber located at the end of the channel. Hadrons are absorbed in the Beryllium, while muons (and neutrinos) pass through. A bending magnet surrounding the downstream portion of the Beryllium absorber selects muons to be channeled into the experimental hall. the Muon channel was tuned to 580 GeV, and transmitted muons with energy greater than ~ 350 GeV.

The muons fall into two categories: "beam" muons travel through all detectors in the beam momentum spectrometer; "halo" muons enter the aperture of the experiment, but miss at least one of the detectors in the beam momentum spectrometer. Because halo muons have unreconstructable momentum and trajectory, they are not considered useful for analysis. Toroidal magnets, called "halo spoilers" were used to deflect the halo muons radially outward. Positively charged muons were used in this experiment.

Reference 105 provides further details.

4.3 The Beam Spectrometer

The beam spectrometer has the dual purpose of identifying incoming muons for triggering the experiment and providing accurate momentum measurement of the incoming muon in event reconstruction software. Each of the four "packages" or "stations" surrounding the spectrometer magnet (NMRE) consists of wire chambers (PBT), (see table

4.1) muon identification hodoscopes (SBT) and muon veto hodoscope jaws (VJ), (see table 4.2). Station 2 had no Z view SBT and station 1 had no VJ. A hodoscope veto wall (VW) was located between stations 3 and 4. The hodoscopes were used in the physics trigger, as discussed below. The wire chambers were used for the beam reconstruction.

See references 106, 107 for chamber, hodoscope, and electronics design.; references 96, 97, for associated software.

4.4 The Vertex Spectrometer

The Vertex Spectrometer consisted of a target within a streamer chamber (SC) surrounded by a superconducting dipole magnet (CVM), the vertex wire chamber (PCV), wide angle chambers (PTA), and the particle identification detectors (TOF, C0, C1). The PTA, TOF, C0 and C1 were not used in this analysis. The targets used in this analysis were liquid hydrogen and deuterium. Data were taken on the two targets during widely separated running periods. The streamer chamber provided 4π coverage of the interaction vertex, but only for 10^{-3} of the total triggers, due to the dead time of recharging the Marx generator. The bulk of this analysis does not use the SC data, however a few multi-jet event examples with full 4π coverage, such as figure I.2, are shown. The PCV, described in table 4.1, provided the most upstream point on tracks following the muon scatter in the non-SC data set. The long lever arm between the PCV and the forward spectrometer chambers allowed accurate measurement of the momentum of tracks entering the forward spectrometer. It should be noted that one plane of the PCV was only 50% efficient in the beam region and that the overall efficiency of the package was typically 85%.[96] Low momentum tracks which would have negative momentum in the CMS were swept out to large angles by the CVM and detected in the PTA. However, no momentum could be reconstructed for these tracks because, without the SC data, there was no measurement within a magnetic field.

Reference 100 gives details of target construction. See reference 108 for PCV construction, references 96, 99 for PCV performance. Concerning detectors not used in this analysis, see references 84 for SC, 93 for TOF, 14 for C0, and 108 for C1.

4.5 The Forward Spectrometer

The forward spectrometer consisted of wire and drift chambers (PCN, PCF, PSA, DC), a superconducting dipole magnet (CCM) and two particle identification detectors

(RICH, CAL).

The wire and drift chamber construction and characteristics are reviewed in table 4.1. The average chamber uncorrelated efficiency was ~ 90%. A correlated inefficiency (where all chambers fail at once) was reported in a region of the DC's in reference 99. This was observed in a data set from an overlapping time period but different trigger than this analysis. A search for this correlated inefficiency using the data set for this thesis showed no inefficiency. In light of this, no inefficiency was assumed in the Monte Carlo simulation of the detectors for this analysis, but an inefficiency was introduced as part of the systematic error analysis, in order to be conservative.

The electromagnetic calorimeter (CAL) was used in this analysis to identify photons. The calorimeter consisted of 20 $3\ m\ (Y) \times 3\ m\ (Z)$ proportional chambers sandwiched between 20 $1\ cm\ (X) \times 3\ m\ (Y) \times 3\ m\ (Z)$ lead sheets. The proportional chambers have only Y and Z views. Each chamber has two cathodes of graphite coating on a plastic frame. Positive charge buildup near the cathodes is detected by copper pads on the outside of the chambers. The pads are 4 *cm* in the central square, 8 *cm* in the middle region and 16 *cm* in the outer region and are arranged in towers. Therefore, the pads can provide transverse shower information while the wire chambers show the longitudinal shower development. In this analysis, the longitudinal information cannot be used because high multiplicity events lead to multiple hits in the same Y and Z regions which cannot be resolved into separate showers.

The RICH is not used in this analysis.

Table 4.1 gives references for the chamber constructions. See reference 96 for PR and reference 97 for TF in the forward spectrometer. References 96, 99 describe for efficiencies of the chambers. References 91, 13, 99 give CAL construction, data reduction code and performance. See reference 109 for RICH construction and performance.

4.6 The Scattered Muon Detectors

The scattered muon detectors have a two-fold purpose. The first is to signal a scattered muon for triggering the experiment. The second is to provide reconstruction of the scattered muon segment, so that the muon track can be identified. The detectors used in the triggers are hodoscopes (SMS) and (SPM) described in table 4.2. The SMS detectors covered the beam region and were used in various configurations as vetoes for the physics triggers. The SPM's had a central hole and were used for scattered muon identification in the trigger used in this analysis. The PTM detectors (see table 4.1) and SMS detectors were used to reconstruct the scattered muon segment. Matching between the track segment and the forward spectrometer tracks was done in the MM program. No SMS or PTM information was used in momentum determination.

See references 96, 97 for PTM, SMS, and SPM construction and performance.

The Large Angle Trigger (LAT)

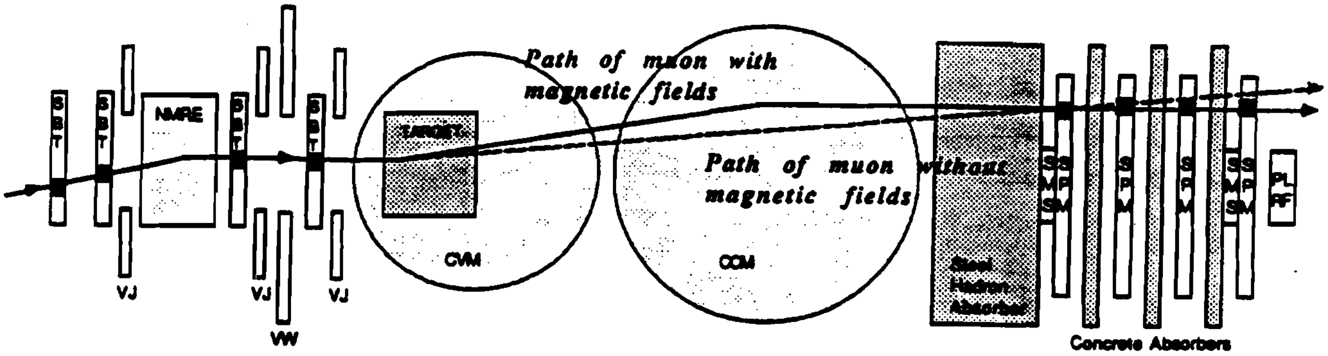

Incoming muon requirements...

1) Hits in 7/7 of the SBT's
2) SBT hits synchronized with accelerator RF
3) No hits in VJ (veto jaws)
4) No hits in VW (veto wall)

Outgoing muon requirements...

1) Hits in 3/4 of the SPM's
2) No hits in SMS 1 or SMS 4
(SMS 2 and 3 not shown)

Figure 4.4. Schematic of the LAT Trigger

4.7 The Triggers

An experimental trigger provides a signal when an event of potential interest has occurred. E665 had many trigger types including Alignment, Calibration and Physics Triggers. The components of the Large Angle Trigger (LAT) used for this analysis are shown in figure 4.4. Specific information on the components of the trigger are listed in table 4.2. The LAT preferentially selected high Q^2 events by requiring muon scatters at large angles:

$$Q^2 = 4E_\mu E'_\mu sin^2(\theta/2).$$

The hit requirements were hits in 7 out of 7 of the SBT's, no hits in the VJ's or VW, hits in 3 out of 4 of the SPM's, and no hits is SMS1 or SMS4. In this analysis, a Small Angle Trigger (SAT) was used for calorimeter studies presented in the next chapter. This trigger projected the incoming muon track in the SBT's to a veto region in SMS1 and SMS2.

An integral feature of all of the triggers was *RF* synchronization. The incoming muons retained the RF structure of the proton accelerator. A device constructed of hodoscopes (PLRF), see table 4.2, tracked the RF structure of the incoming muon beam. Requiring detector hits to be synchronized with the RF eliminated many sources of trigger background.

Nevertheless, as will discussed further in the next section, the trigger performance was not high in Run87. Only approximately 5% of the total physics triggers written to tape had evidence for a muon scatter. The filter and DR programs were used to remove the uninteresting events. Furthermore, the efficiency of the LAT for accepting muons was found to be higher for scatters to positive Z than negative Z. This has no affect on this analysis other than to loose useful events.

See references 100, 98, 94.

4.8 Data Reduction

This section describes the reduction of data from the events written to tape to the initial event sample which formed the input to this analysis. Only the LAT data stream is followed.

The filter rejected events with any of the following characteristics:[103]

1. No in-time reconstructed beam tracks with 7/7 in SBT's.
2. Multiple in-time beam tracks.
3. Beam track fit $\chi^2_{prob} > 1\%$ and $P < 300\ GeV$.

The filter accepted events if any the following were True:

4. One track in the forward spectrometer with no hits in PSA
5. A track in the forward spectrometer with fit $\chi^2_{prob} > 1\%$
6. For events with only one forward spectrometer track, no track consistent with the unscattered extrapolation of the incoming beam track (details in reference 12).

The main sources of rejection were from sources 1, 2 and 6. The losses were related to hardware problems and philosophy of the trigger,[110] and not to the reconstruction code applied to these events.[111] On average, the LAT filter output represented 35% of the filter input.[12] The efficiency of the filter for accepting deep inelastic scattering events was measured to be > 99.99%.[100] The data then entered the reconstruction chain..

Parallel to the data filter, Monte Carlo simulated data, used to study acceptance effects, are generated. The Reconstructed Monte Carlo data used the output of the Truth Monte Carlo described in the chapter 2. The particle decays are simulated. Multiple scattering and photon conversions in the target material and the detectors are simulated using the GEANT (version 3.12) program[112] and code to represent uncorrelated inefficiencies.[96] Tracks are digitized so that the input to the reconstruction chain is in the same format as the data. The description of the simulation of showers in the Electromagnetic Calorimeter is found in reference 113. Electromagnetic and hadronic energy depositions are simulated but longitudinal shower profiles are not. This simulated physics data then enters the reconstruction chain.

The reconstruction chain consists of PR, TF, MM and VX. For tracks in the forward spectrometer, the overall reconstruction efficiency due to the algorithm and the chamber efficiencies was 80%, independent of momentum.[96] The muon matching efficiency was $> 98\%$ and the vertex finding efficiency was $> 99.9\%$.[100] There was no evidence for biases in the momentum distributions of the particles introduced by inefficiencies in the software.[12,96]

The DR program selected events according to the cuts:

$$0 < P_{beam} < 10000\ GeV$$

$$0 < Q^2 < 10000\ GeV^2$$

$$10 < \nu < 10000\ GeV$$

$$0.003 < x_{Bj} < 100$$

$$0 < y < 10$$

$$-13.0 < x_{vertex} < -10.0\ m,$$

where x_{vertex} is the X position of the vertex in the E665 coordinate system. This program rejected 92% of the remaining LAT events. A table describing the rejected events can be found in reference 12. The majority of rejected events failed the vertex requirement. Most had vertices outside of the target region. Other losses were due to beam reconstruction and scattered muon identification failures.

The resulting sample for this analysis consisted of 117,113 events from the D_2 target and 31,236 events from the H_2 target.

Finally, the information on the events is written to summary tapes (DST) in compact form. As a technical point concerning use of the Monte Carlo in the analysis, the DST format for storing the Monte Carlo information mixed the apparent and true kinematic variables in electromagnetic radiative events in the True Kinematic Bank. This problem was corrected in the analysis code by calculating all "true" kinematic variables at the partonic interaction vertex.

The output tapes form the "initial sample" of data for the analysis described in the chapter 5.

Chapter 5

The Hydrogen and Deuterium Data Sets

This chapter describes the characteristics of the data sets which were used for this analysis, lists the cuts which were applied to obtain the final sample, and provides detailed comparison of the data to the Reconstructed Monte Carlo simulation of the detector.

Use of charged track and electromagnetic calorimeter data from the Run87 H_2 and D_2 targets were used for this analysis will be justified. Comparison is made between the H_2 and D_2 data sets, which were collected during widely separated time periods. Several previous analyses combined the charged particle data from these periods, but this is the first analysis to combine the electromagnetic data for the two periods.

New variables which are used in the particle distribution comparisons are:

p_T The transverse momentum of the particles measured with respect to the virtual photon axis.

$z = E_{particle}/\nu$

$x_F = 2P_L^{CMS}/W$, commonly called "Feynman x."

The CMS is the center of momentum frame of the virtual photon and the proton. The coordinate system is rotated so that the X axis lies along the virtual photon direction.

The cuts which determined the final analysis sample are explained in detail. The purposes of the cuts are to select the kinematic ranges where QCD is applicable and a large fraction of events are expected to be due to hard QCD process; to remove events in which interactions other than a deep inelastic scatter also occurred; and to define those particles which will be used in this analysis. The full set of cuts is summarized in the final section of this chapter.

Throughout this chapter, the data is compared to the E665 Reconstructed Monte Carlo simulation which has been run through the reconstruction chain. Attention should be paid to the quality of the modeling of the E665 detector, *eg* acceptance losses in the particle kinematic distributions.

5.1 Event Requirements

The general requirements on the events for the analysis sample fall into two categories. First are the cuts which isolate the kinematic regions of interest. Second are the requirements designed to remove events with particles from processes external to the deep inelastic scatter or with grossly mismeasured kinematics.

The kinematic cuts applied to each event are:

$$W^2 > 400\ GeV^2$$

$$Q^2 > 3\ GeV^2$$

$$y < .80$$

$$x_{Bj} > 0.003$$

$$-12.0 < x_{vertex} < -10.2$$

The W^2 cut selects the region where observable jet production is expected. The Q^2 cut is chosen to be two order of magnitudes larger than typical values of Λ^2_{QCD} and an order of magnitude larger than the expected intrinsic momentum and fragmentation effects to ensure that the theory described in chapter 1 is applicable. The y cut removes radiative events. [114] The x_{Bj} cut was from the Data Reduction Program described above, but is should be noted that the y and Q^2 limits effectively impose this. The vertex cut selects events from the target region. These kinematic requirements eliminated 87% of the total sample. All percentages discussed below are of the sample after kinematic cuts.

The following requirements were applied in order to isolate a well-understood deep inelastic scattering sample:

1. *One and only one in-time incoming muon. No out-of-time incoming muons.*

The single in-time incoming beam requirement eliminated the possibility of mismeasuring the momentum of the incoming muon due to confusion in pattern recognition and vertex assignment. Three percent of the sample failed this cut.

2. *One and only one muon in the muon detector*

This requirement is made for three reasons. First, multiple muon tracks in the muon spectrometer may lead to misidentification of the scattered muon. Second, hits from muons unrelated to the deep inelastic scatter may introduce confusion in pattern recognition in the forward spectrometer. Third, in-time non-related muons may bremsstrahlung or interact introducing extra energy in the calorimeter. At the same time, real deep inelastic scatters with decays to muons will be removed, so this cuts deserves careful review.

9.6% of the event sample had more than one track (LPRO) in the muon detection system. The rate of multiple muon tracks unrelated to the event was measured using the random beam (no interaction) sample to be 4.4%. This implies that the remaining 5.2% of the multimuon events are due to decays.

The sources of unrelated multiple muon tracks were identified through a scan of 100 random beam events with two or more muon tracks in the PTM and SMS muon detectors. 48% of the scanned events had out-of-time muon tracks in the PTM detector, identified by a track found in the detector with no associated hits in the muon scintillators. The rate is consistent with expectations given the 300 *ns* live-time of the PTM detector. 30% were in-time halo muons which traveled through the return yoke of the CCM magnet and were bent back into the aperture of the spectrometer. Of these events, half showered, producing particles which were detected in the electromagnetic calorimeter. The average energy of these clusters in the calorimeter was 2.35 *GeV*, and the maximum observed energy in the scan was 33.42 *GeV*. 12% of the scanned events were in-time unvetoed halo muons, identified through their associated hits in the muon scintillators and their location in a region of known inefficiency in the veto wall. [115] In 10%, the muon showered while traveling through the muon detector creating numerous hits which were identified as multiple muon tracks.

This cut also eliminates decays of hadrons into muons. According to a study of 3000 reconstructed Monte Carlo events, over half of the decays to muons have small angles with respect to the E665 beam axis, causing the trigger to veto. Only 5.6% of the total reconstructed events had decays to muons, consistent with the observation from the data. The scattered muon was confused with a decay muon in only one of the 168 decay events. Most of the remaining events were pion decays to an observed muon and an unobserved neutrino. This reaction has a decay length of 7.8 *m*. In 48% of these events the pattern recognition program confused hits in the chambers due to the unavoidable failure to recognize the decay vertex. Of the remaining 89 events, 43% of the μ tracks would be dropped from the analysis due to the track cuts described below. These muons had low momentum, therefore little affect on the jet vector direction. The 89 events with properly reconstucted decays showed no apparent bias in event multiplicity, W^2, Q^2.

3. *No electromagnetic cluster with energy* $E > 0.33E_{Beam}$ *within a* 30 *cm region of the projected incoming muon track*

The purpose of this cut is to reject high energy radiative inelastic events. In these events, the kinematics measured from the scattered muon are incorrect and there is an extra high energy photon not associated with the deep inelastic scatter.

Using the calculations of Mo and Tsai,[80] it can be shown that $\sim$ 30% of the deep inelastic scattering events in this analysis are expected to be radiative events, as can be seen in figure 5.1. For E665 beam energies, radiation of photons will be sharply peaked along the incoming muon direction, with a FWHM of $\sim$ 4 *mrad*. For the kinematic cuts in this analysis, approximately 2/3 of the radiated photons will carry more than 33% of the incident muon energy.[114] These photons can be rejected by projecting the incoming muon track to the the calorimeter and searching in a region of 30 *cm* for an associated cluster of energy greater than 33% of the incident muon energy. 18% of the events were eliminated due to this cut. According to studies of the reconstructed Monte Carlo, 92% of those events which were rejected by this cut were radiative events.

The remaining 8%, which represented 1.2% of the total event sample, were random spacial overlaps between the projected incoming muon and photons from decays. This

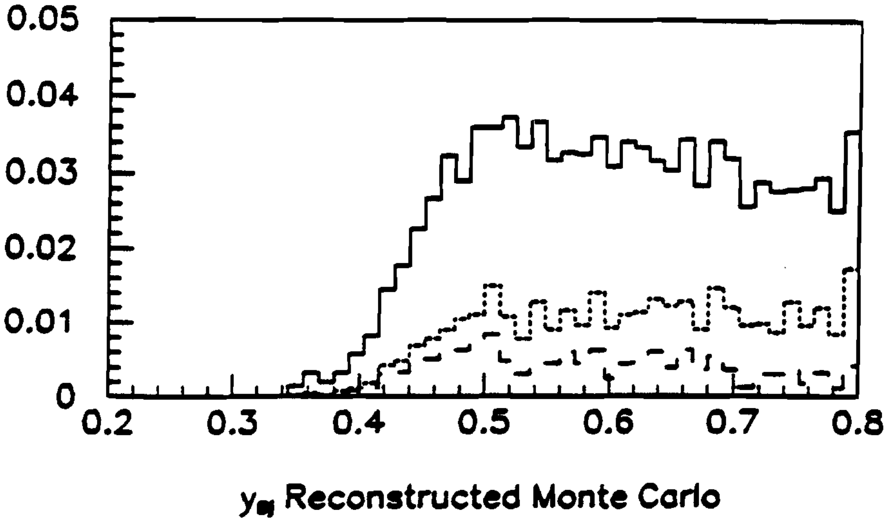

Figure 5.1. Radiative events as predicted by Mo and Tsai as a function of y, normalized to the total number of events passing kinematic cuts: solid – all events, dot – radiative events, dash – radiative events which remain after cut on photons near the projected incoming muon track.

represents 42% of all events with a photon of energy larger than 33% of the beam energy made a random overlap and were cut. There was no bias in the kinematic distributions of these photons. A comparison was made between the jet analysis with and without the photons that were removed by this cut and no significant difference was observed.

4. *No events with zero hadron tracks,* $\nu > 200$ *GeV and* $E^{CAL}_{Total}/\nu > .35$

Events with no tracks, $\nu > 200$ *GeV* and total energy deposited in the calorimeter, E^{CAL}_{Total}, greater than 0.35ν, are due to coherent bremsstrahlung according to Monte Carlo. From Monte Carlo studies, after the projected muon cut, 7.5% more of the radiative events were removed by this requirement. Only 0.3% of the non-radiative events were eliminated by this cut.

5. *No particle that was kinematically forbidden*

21 events were eliminated by requiring that all particles in the event be kinematically allowed. Most events of this type were eliminated because one particle had $z > 1.1$. The momenta of these particles were greater than 300 *GeV*. A visual scan indicated that these tracks were probably incorrectly identified muons. The remaining events were eliminated because the total energy in the event summed to more than $\nu + 3\Delta\nu$, where $\Delta\nu$ is the error on the ν measurement. In these cases there was a large energy deposit in the calorimeter, near the east and west edges, leading to the hypothesis that a halo muon emitted a bremsstrahlung photon and was then bent out of the spectrometer acceptance.

The final "analysis data sets" consisted of 2503 hydrogen events and 9845 deuterium events. The resulting distributions in W^2,Q^2, x_{Bj}, and y for the H_2 and D_2 data sets are

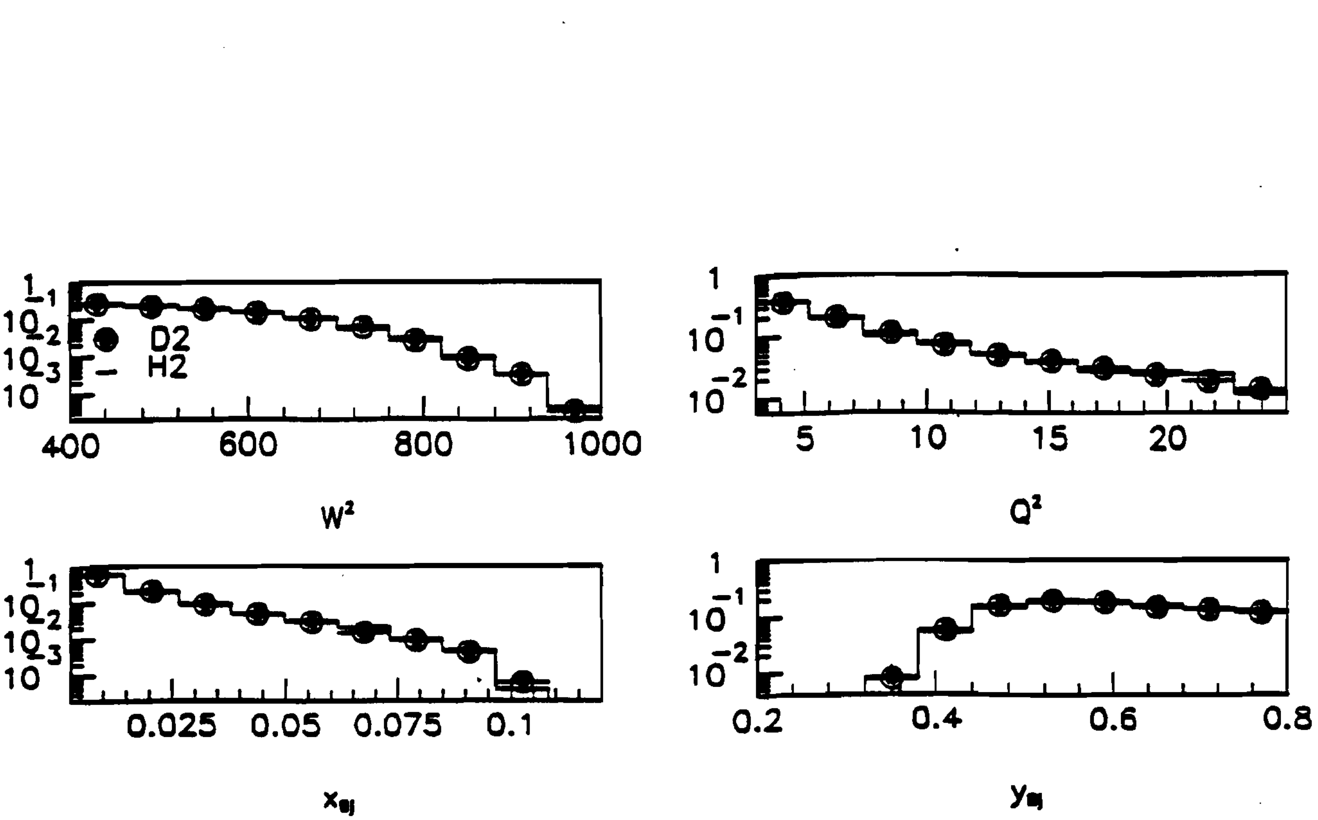

Figure 5.2. Comparison the the H_2 (solid line) and D_2 (points) event kinematics after all event requirements have been applied: **a)** W^2, **b)** Q^2, **c)** x_{Bj}, **d)** $y = \nu/E_{Beam}$

compared in figure 5.2. The distributions have been normalized to have the same number of entries. The two data sets are compatible within statistics, which are indicated on the D_2 data points. The reconstructed Monte Carlo reproduces the kinematic features of the data well, as can be seen from figure 5.3.

5.2 Charged Tracks

The standard E665 software package (PTMV) was used to determine the kinematics of tracks used in this analysis. Only information from the proportional and drift chambers of the forward spectrometer were used. The electromagnetic information in the calorimeter is not used to augment the information from the wire chambers or to make cuts on charged tracks. The E665 software determines two track categories: "fitted"– which are associated to the primary vertex, and "close" - which are all other tracks, whether or not they are

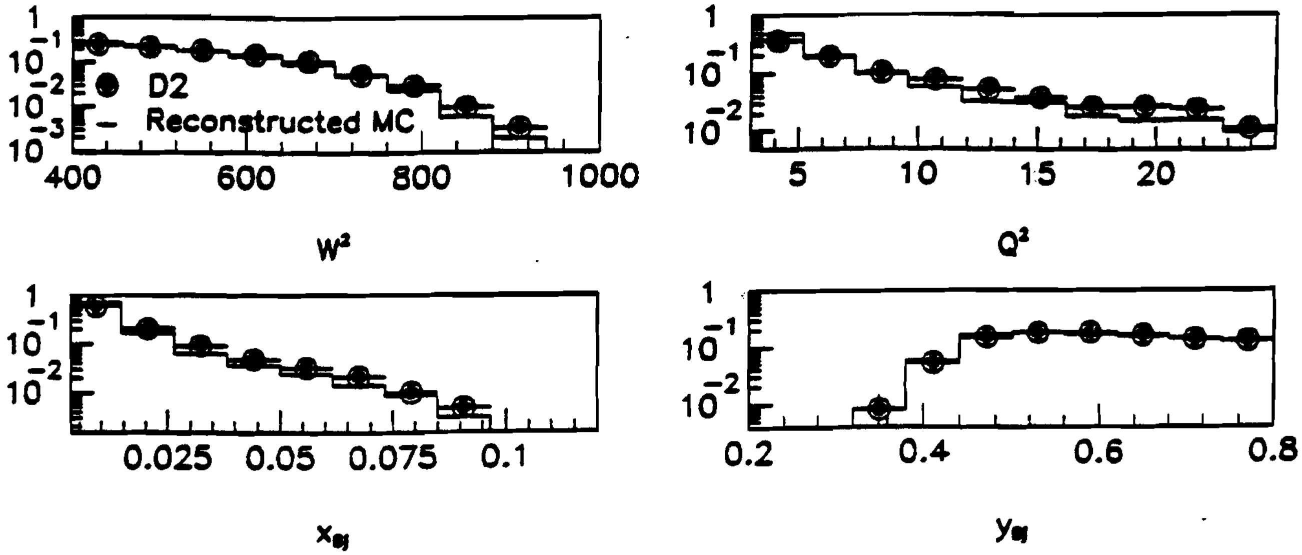

Figure 5.3. Comparison the Reconstructed Monte Carlo (solid) and Data (points) event kinematics after all event requirements have been applied: **a)** W^2, **b)** Q^2, **c)** x_{Bj}, **d)** $y = \nu/E_{Beam}$

close to the vertex. Although close tracks are not explicitly eliminated, the cuts described below effectively eliminate all close tracks.

Detailed studies[12] of the hydrogen and deuterium tracks have resulted in a set of "standard cuts" used in the E665 track analyses:

$$\chi^2_{prob} > .001$$

$$D/\sigma < 5.0$$

$$\Delta P/P < 0.05$$

where D is the minimum distance of approach to the vertex, σ is the error, and P is the track momentum with error ΔP. The resulting distributions of χ^2_{prob}, D/σ and $\Delta P/P$ are shown in figure 5.4a-c for the samples of the hydrogen and deuterium data sets, which agree well.

Distributions of track multiplicity, P_T, and z, shown in $d-f$ of figure 5.4, further demonstrate the agreement between the data sets. Although there was no minimum cut on x_F, the spectrometer acceptance effectively cut all tracks with $x_F \approx -0.1$. The geometrical acceptance of the spectrometer reaches $\sim$ 100% for $P \approx 15$ GeV and $x_F \approx 0.2$. The P_T of tracks is largely uncorrelated to the momentum as can be seen by figure 5.5. Hence the acceptance losses in P do not translate to an acceptance cut in P_T.

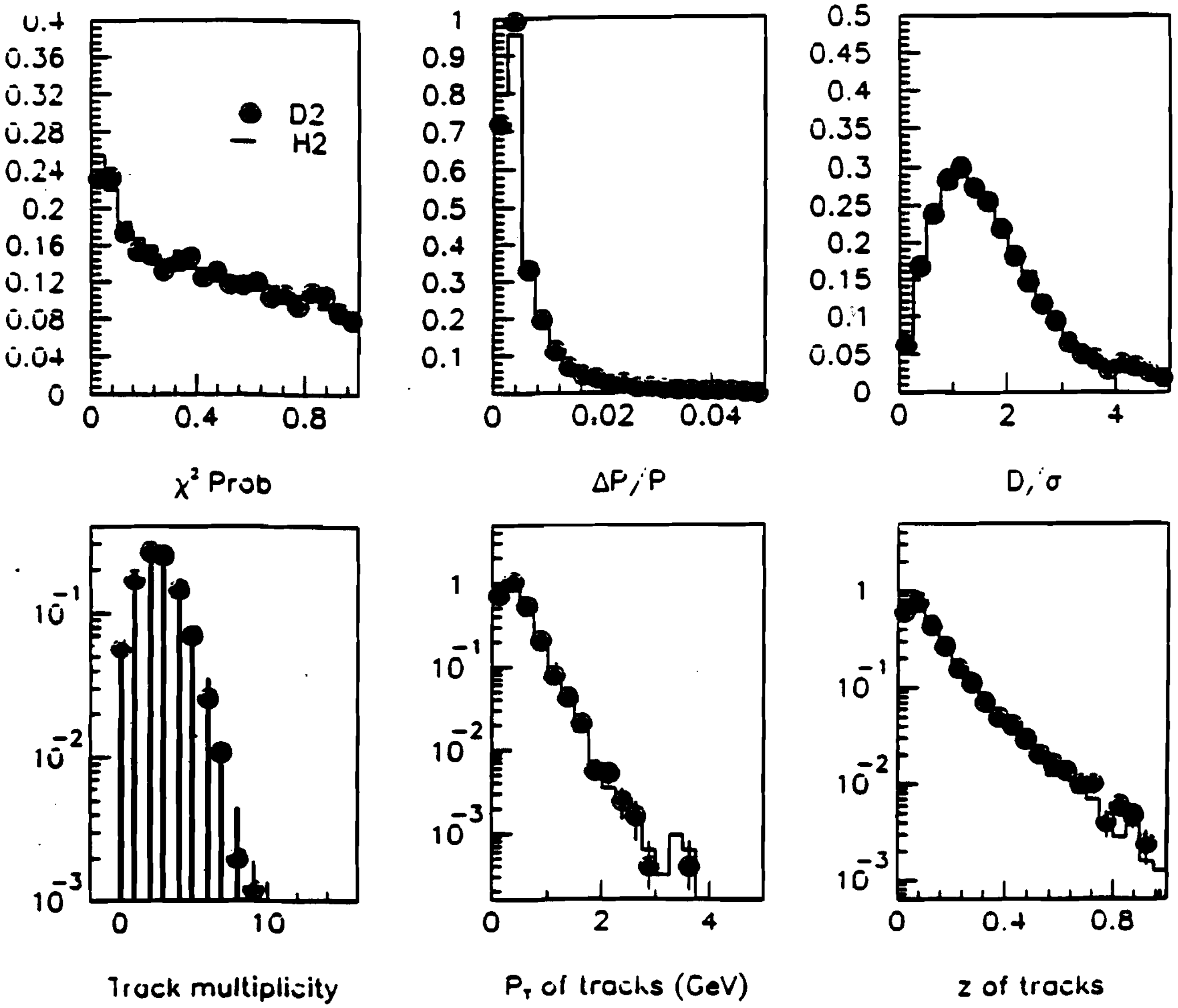

Figure 5.4. Characteristics of tracks used in the analysis for H_2 (solid) and D_2 (points): **a)**χ^2_{prob},**b)** $\Delta P/P$ vs.P, **c)** D/σ, **d)** multiplicity, **e)** P_T distribution, **f)** z distribution. Histograms are normalized to the number of events

Based on the agreement shown in figure 5.4, events from the two data sets may be combined.

Charged tracks were assumed to be pions. According to a study of the reconstructed Monte Carlo, charged kaons, electrons and protons actually represent 6.8%, 4.1% and 1.5% of the particle sample, respectively. Therefore Monte Carlo correction for the true masses is reasonably small.

Figure 5.6 compares the resulting set of tracks to the reconstructed Monte Carlo. Although the agreement is not perfect, note that the Monte Carlo reproduces the the

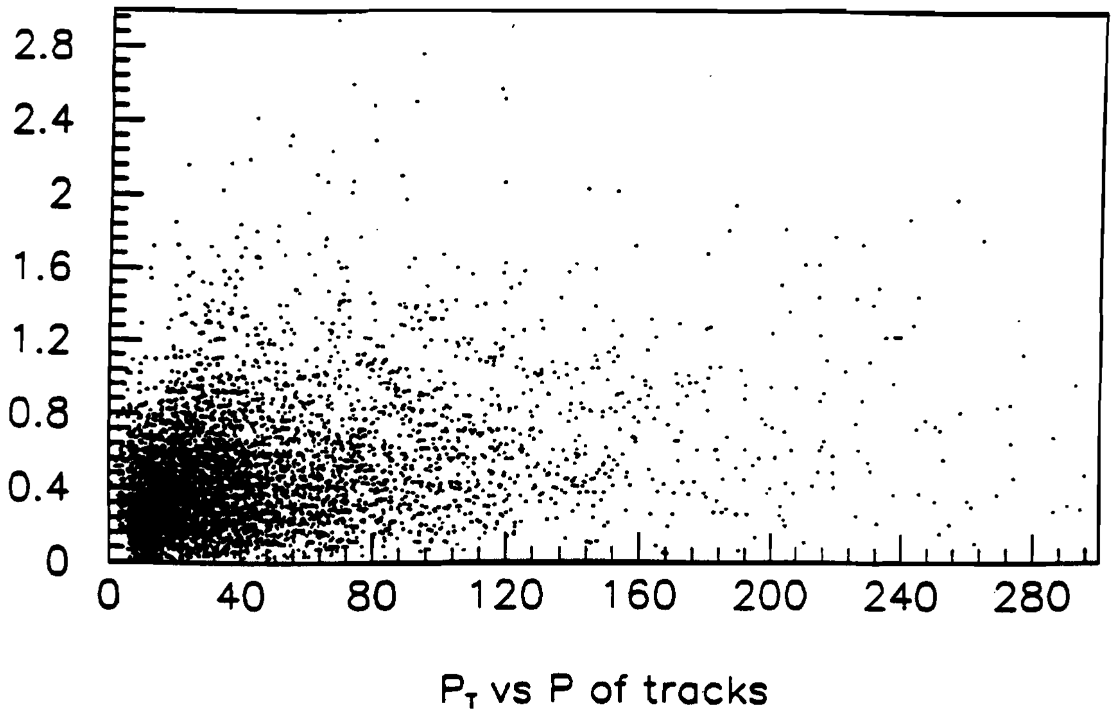

Figure 5.5. P vs. P_T for uncorrected tracks

acceptance in transverse momentum and z well. This is important if the Monte Carlo is to be used for acceptance corrections.

5.3 Electromagnetic Clusters

The goal of the requirements presented in this section is to isolate the set of clusters in the analysis sample which are due to photons. Although the calorimeter provides information on the longitudinal development of showers, the information can only be interpreted for clusters that do not have overlapping bitube information – a small fraction of the total analysis sample. If a bitube is shared between two clusters, then the shower information for each cluster cannot be deconvoluted. Therefore, the photon candidates are obtained strictly through track isolation cuts.

To be certain that the isolation cuts remove most non-photon clusters and that the remaining clusters are "electromagnetic" in origin, studies of the removed and kept clusters are presented below. In order to understand the samples, one must first determine the

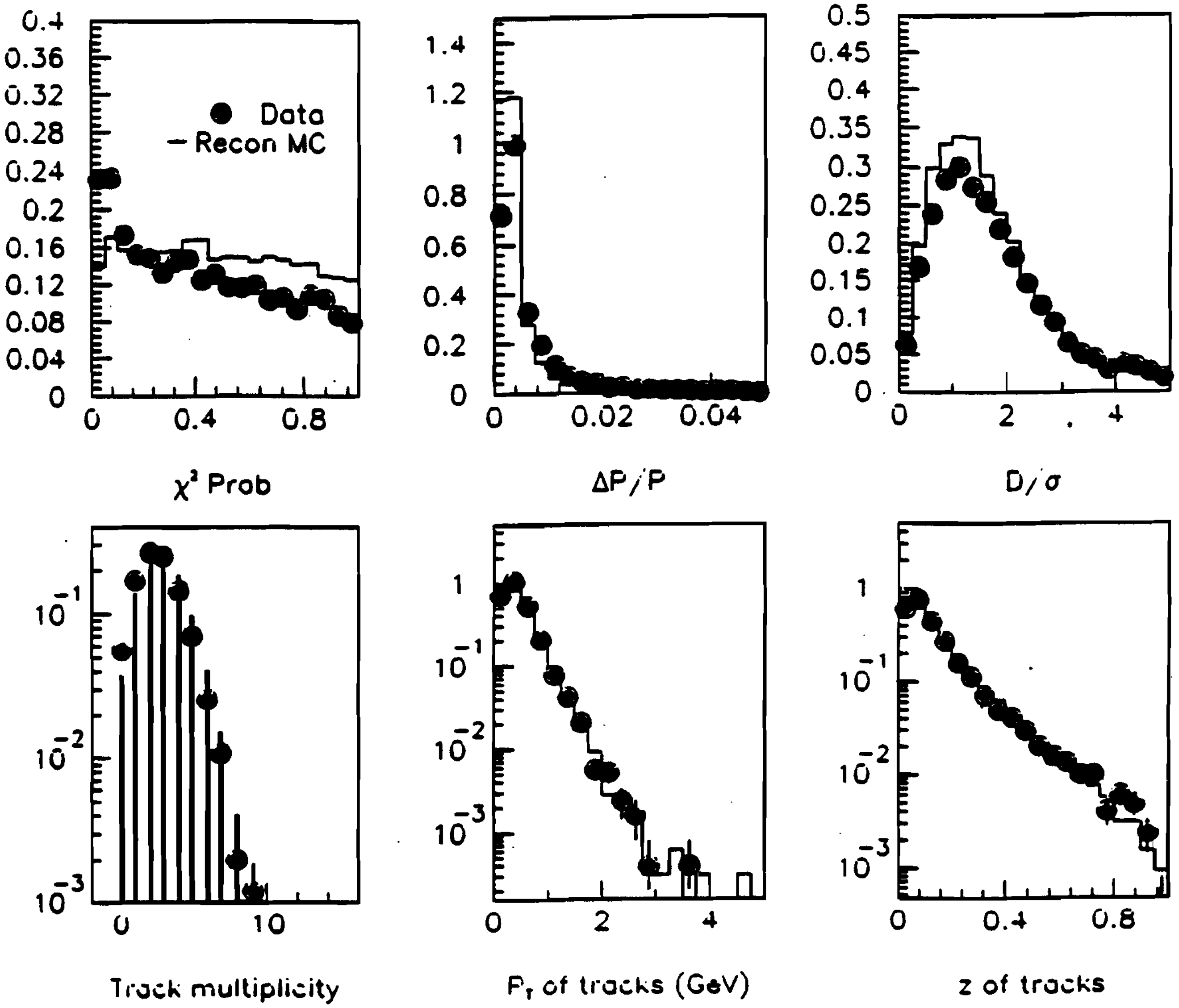

Figure 5.6. Characteristics of tracks used in the analysis for reconstructed Monte Carlo (solid) and data (points): **a)**χ^2_{prob}, **b)** $\Delta P/P$ vs.P, **c)** D/σ, **d)** multiplicity, **e)** P_T distribution, **f)** z distribution. Histograms are normalized to the number of tracks

characteristics of "electromagnetic" and "hadronic" showers in the calorimeter. References 99, 91, and 116 provide detailed analyses and characterizations of electromagnetic and hadronic showers in the calorimeter. For comparison, a sample of electromagnetic clusters is isolated using muon-electron scatters. The "μ-e sample" consists of events with $x_{Bj} < .003$, only one negative track with $z > 0.5$ and no positive tracks other than the scattered muon.

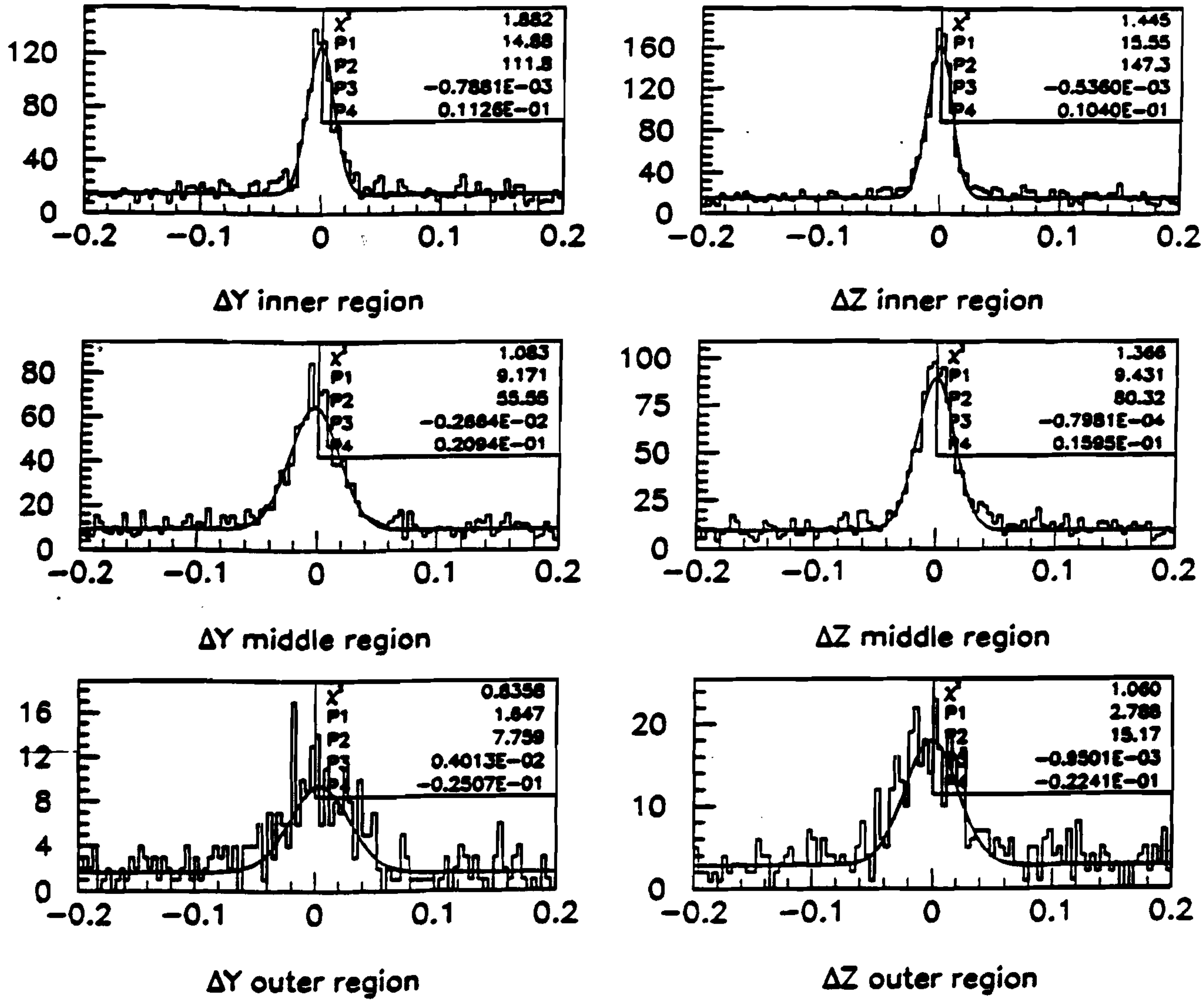

Figure 5.7. Distance from track to nearest cluster in Y and Z for the inner, middle and outer regions of the electromagnetic calorimeter. Data from the analysis sample for the hydrogen running period is shown. The fit is to a Gaussian plus a constant offset. $P1$ represents the offset. $P2$, $P3$ and $P4$ are the amplitude, mean and sigma of the Gaussian.

The calorimeter aperture was defined as:

$$-1.42 < Y < 1.42 \; m$$

$$-1.42 < Z < 1.42 \; m.$$

One outer region calorimeter pad had very high energy ($> 200 \; GeV$) oscillations throughout the D_2 running period which were not eliminated by the oscillation cuts described below. The oscillation introduced fake very high P_T photons and caused the energy of real photons hitting this region to be mismeasured. Therefore this pad region was removed for the analysis:

$$-1.42 < Y < -1.0\ m$$

$$1.0 < Z < 1.42\ m.$$

A minimum energy cut of 5 GeV in the pads was applied in this analysis. This eliminated low energy pad oscillations and cases where the error on the energy of the cluster is sizable. The energy resolution in the calorimeter was measured to be [91]

$$\Delta E/E = 0.07 + \frac{0.44}{\sqrt{E}},$$

Hence at $E_{cluster} = 5\ GeV$ the error on the energy of the cluster is 25%. According to the Monte Carlo, 16% of all photons from pion decays had energy less than 5 GeV and would be cut from the analysis. A study of the jets using Monte Carlo data with and without this energy cut showed no statistically significant change in the average jet transverse momenta. This is not surprising since the momenta of these photons is quite low.

Most oscillations in the pad towers were of low energy and are eliminated by the minimum energy cut. Higher energy oscillations could be eliminated by using longitudinal shower information in those cases where the bitubes were not shared by several clusters. Oscillations are characterized by:

$$Shower\ start\ >\ plane\ 20$$

$$Back/Front\ energy\ ratio < 0.001$$

$$Center\ of\ gravity\ < 0.005\ m$$

$$breadth\ > 0.0$$

A visual scan of 100 randomly selected events in the hydrogen sample and 100 events in the deuterium sample determined that less than 0.1% of the clusters in the final "photon" sample were oscillating pads. These were mainly in the D_2 sample and are discussed below. Note that pad oscillations and noise are not included in the reconstructed Monte Carlo, although studies using simple models were made.

As stated above, pointing with fully reconstructed tracks was used to eliminate clusters associated with tracks. Tracks which reached PCF3 were swum through the magnetic field using the standard E665 swimming package.[117]

The position of the track was determined at a depth of 40 cm in the calorimeter, which is approximately the shower maximum for electromagnetic showers and the shower start for hadronic showers.[99] The distances from the track to the nearest cluster in Y and Z are shown for the inner, middle and outer regions of the calorimeter in figure 5.7. The alignment adjustments required to center these distributions on zero were: $Y_{correction} = -0.0089\ m, Z_{correction} = -0.0064\ m$. One would expect these distributions

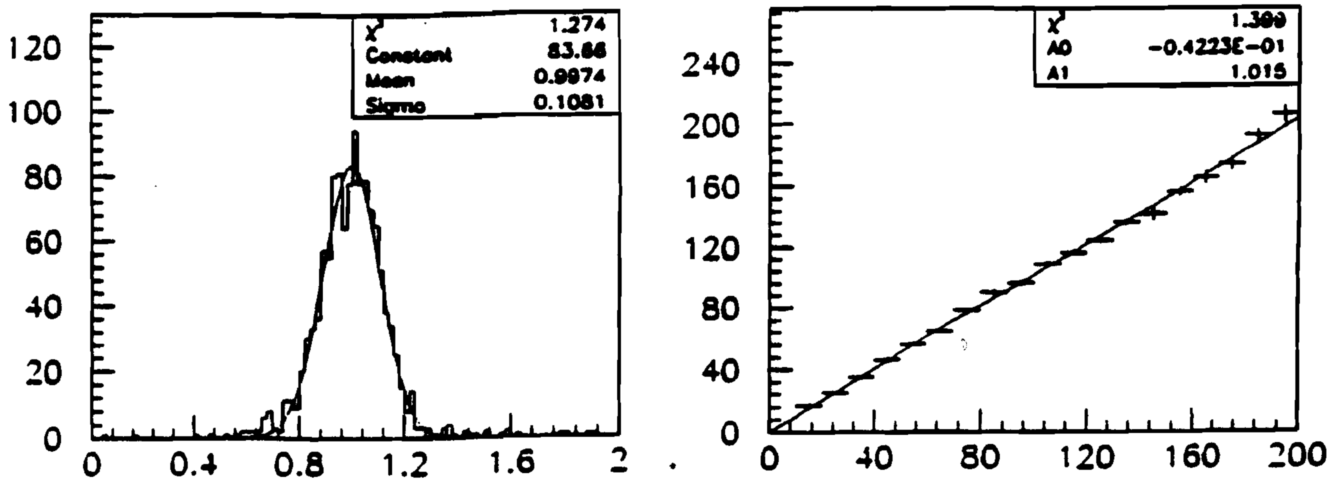

E/P for mu–e candidates, H2

<E> vs. P, H2 (GeV)

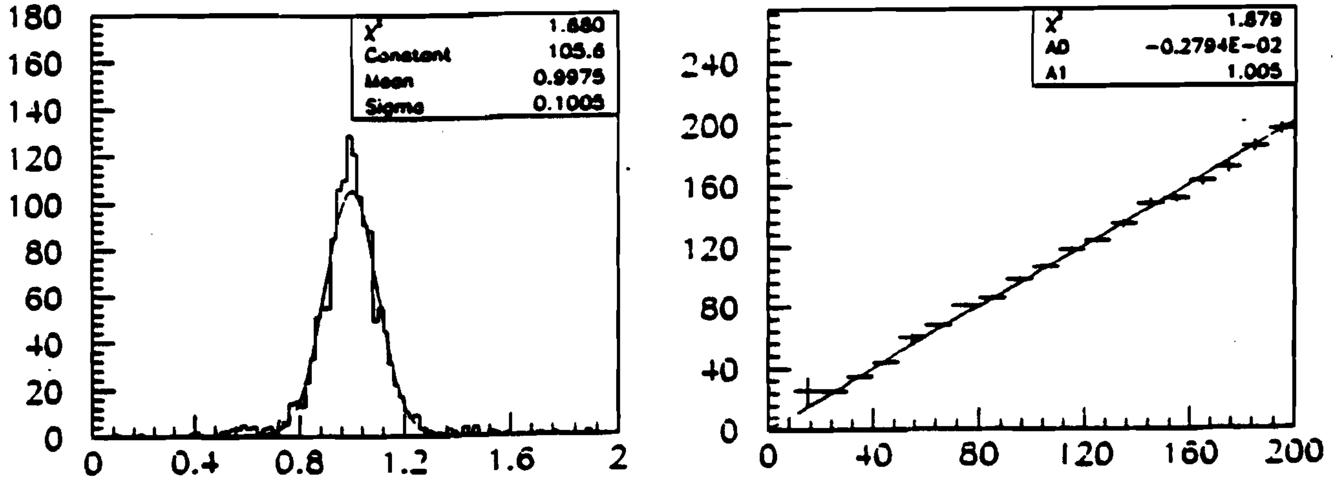

E/P for mu–e candidates, D2

<E> vs. P, D2 (GeV)

Figure 5.8. Distributions of $E_{corrected}/P_{track}$ and $\langle E_{corrected} \rangle$ vs. P_{track} for the hydrogen and deuterium running periods. A straight line fit to $\langle E_{corrected} \rangle$ vs. P_{track} with offset $A0$ and slope $A1$ indicates that the correction over the range of energies used in this analysis is accurate.

to be a combination of a gaussian distribution from clusters associated with the track and a flat distribution from unassociated clusters. The distributions in figure 5.7 are reasonably well fit with this assumption. The area under the peak due to the constant offset is small compared to the area of the gaussian, indicating that few clusters are randomly overlapping with tracks. Considering clusters within 3 σ to be associated with the tracks, one finds that clusters within 5 *cm*, 7.5 *cm* and 10 *cm* should be associated with tracks in inner, middle and outer regions, respectively. Clusters not associated with tracks are

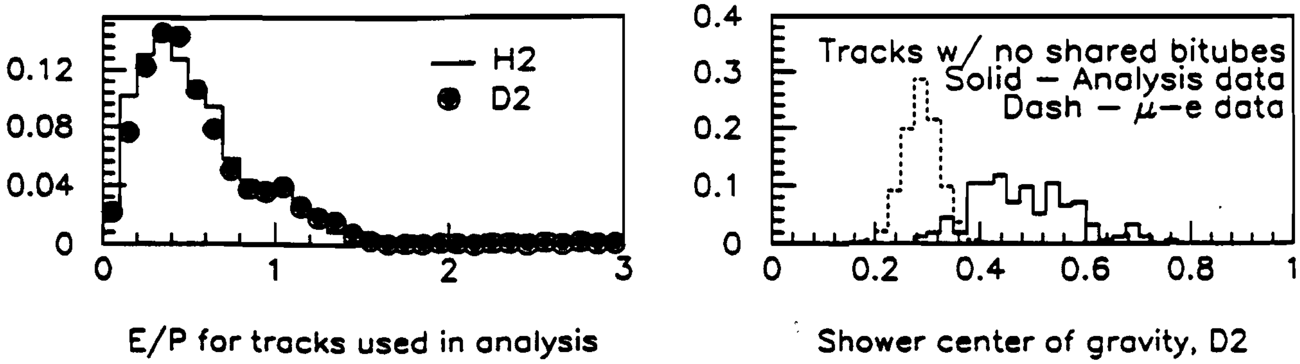

Figure 5.9. **a)** The E/P distribution for all tracks with associated clusters for the hydrogen and deuterium samples used in this analysis. The small excess at $E/P > 0.7$ is due to photon conversions to e^+e^- pairs. **b)** The center of gravity in the calorimeter for those hadronic showers with no shared bitubes. The dashed line shows the center of gravity distribution for electromagnetic events. Center of gravity is measured in meters from the face of the calorimeter.

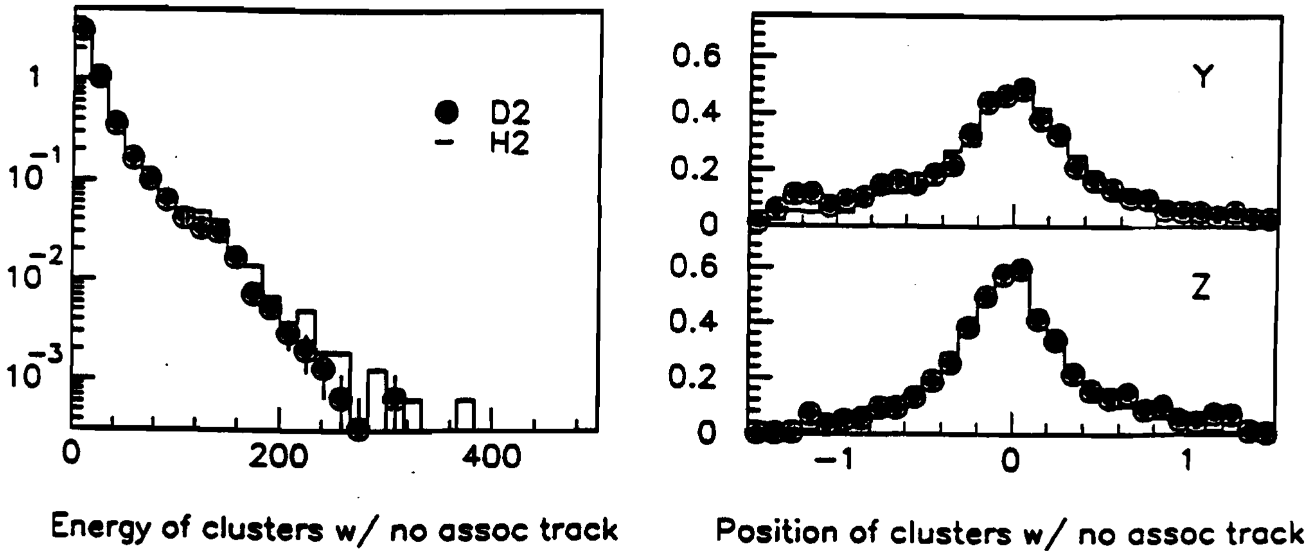

Figure 5.10. For the H_2 (solid) and D_2 (points) data sets, the **a)** Energy, **b)** spacial distributions of the photons

assumed to be due to photons.

The final energy calibration of the calorimeter is determined using the $\mu - e$ scatters.

The distribution of the ratio of the energy of the cluster to the momentum of the track in $\mu - e$ events is calibrated to be centered on one. The corrections applied in this analysis are:

$$\mathrm{H}_2 : E_{corrected} = 0.8758 + 1.0105 E_{cluster} + 0.00158 E^2_{cluster}$$

$$\mathrm{D}_2 : E_{corrected} = 0.7342 + 0.9780 E_{cluster} + 0.000748 E^2_{cluster}$$

Figure 5.8 shows the distributions of $E_{corrected}/P_{track}$ and $E_{corrected}$ vs. P_{track} for each running period. Note that the width of the E/P distribution is consistent with the energy resolution given above. The corrections give $\langle E \rangle = P$ for the full range of electromagnetic energies which will be used in the analysis.

Applying the above energy corrections and track association to the analysis events, one obtains a set of tracks with associated clusters. Figure 5.9a shows the E/P distribution for all tracks with associated clusters for the hydrogen and deuterium samples. The two data samples agree well. There is no evidence of a high rate of random association of clusters with tracks, which would be characterized by large values of E/P. To further demonstrate that clusters associated with tracks are from hadrons rather than random coincidence, figure 5.9b shows the distribution of the center of gravity of the showers in the calorimeter for all tracks unshared bitubes (solid line). This distribution is consistent with character of hadronic showers.[99] For comparison the distribution for mu-e events is shown by the dashed line.

The remaining clusters in the sample are defined to be photons. The energy and spacial distributions of the photons is shown in figure 5.10. One can see evidence of remaining pad oscillations in the D_2 data at $Y < -1.\ m$ and $Z < -1\ m$. A scan of random beam events showed that for oscillations with $E > 5\ GeV$, the average oscillation energy was 6.4 GeV. This average energy and the frequency of these oscillations were too low to warrant removing these pads from the analysis. Furthermore a simple simulation of this oscillating pad in the reconstructed Monte Carlo showed no measurable changes in the jet momenta. Even less frequently, an oscillation with lower average energy, occurred in the D_2 data at $Y > 1.\ m$ and $Z > 1.\ m$, but had no discernable effect on the jet analysis. Aside from these oscillations, the two data sets agree well within errors.

The same distributions are then compared to reconstructed Monte Carlo in figure 5.11. The distributions are normalized to the number of events. The agreement between data and reconstructed Monte Carlo is quite good for the transverse momentum, z and spacial distributions, which are the most important for acceptance corrections.

The resolution of the clustering algorithm is 10 cm.[91] Therefore, for energies larger than 50 GeV the majority of clusters in the calorimeter are actually merged neutral pions. The pion mass was assigned to these clusters, but this represented an insignificant correction.

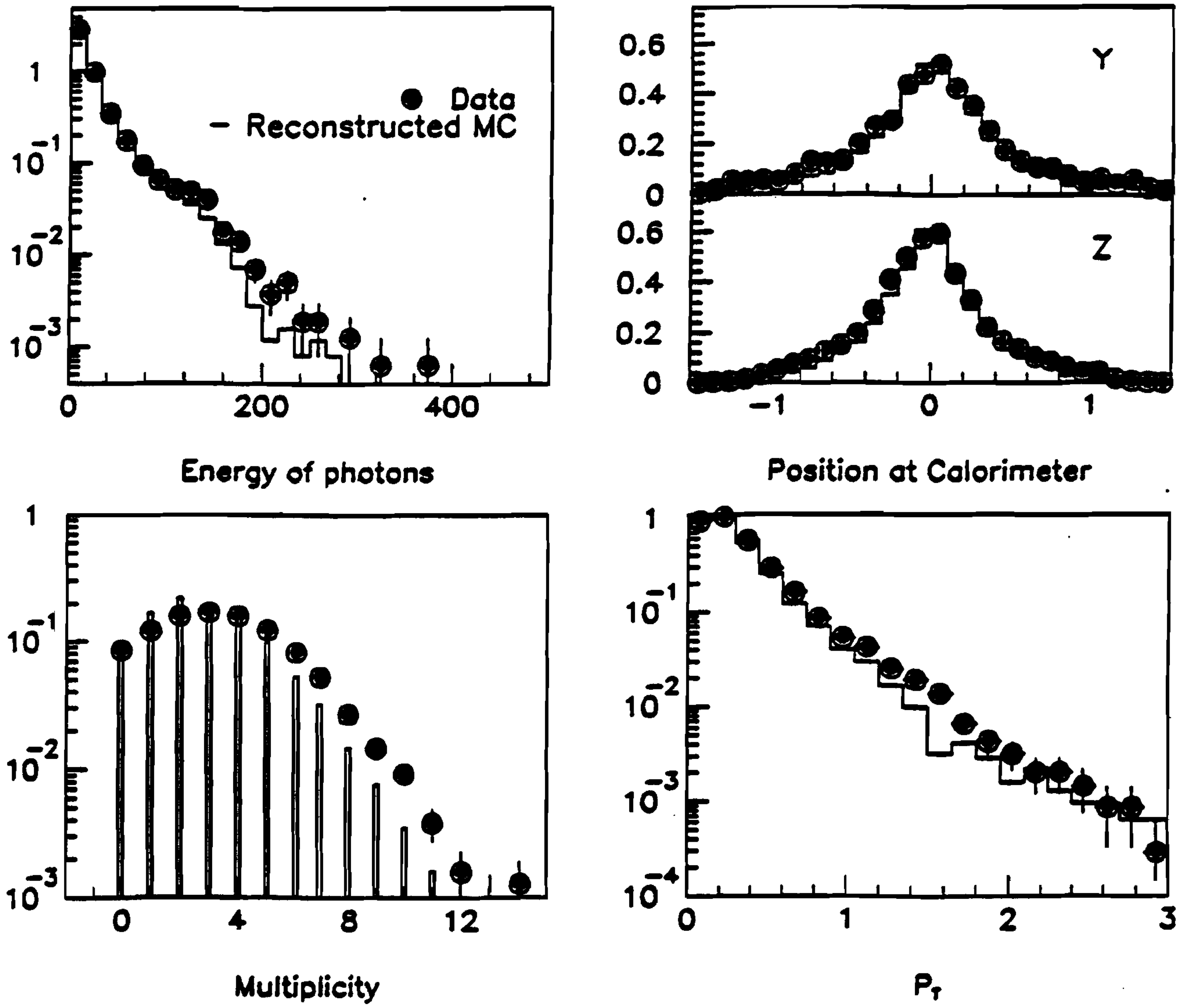

Figure 5.11. For the Reconstructed Monte Carlo (solid) and data (points), the **a)** Energy, **b)** spacial, **c)** multiplicity and **d)** transverse momentum distributions of the photons

5.4 The Acceptance

- *Acceptance of the Scattered Muon.*

In the Q^2 and x_{Bj} region used in this analysis, the E665 detector is expected to be fully efficient for detecting the scattered muon. Thus differences between true values of the kinematic variables at the virtual photon-parton vertex and the measured kinematic

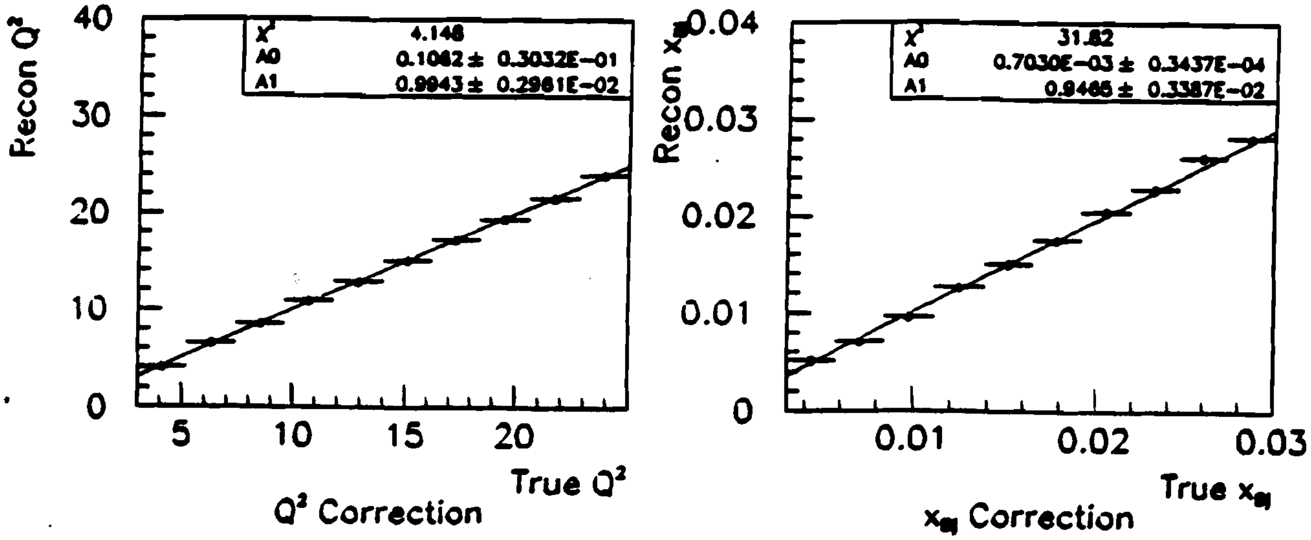

Figure 5.12. Comparison of True event kinematics to Reconstructed event kinematics. The fit is a straight line with slope A1 and offset A0. **a)** Q^2; **b)** x_{Bj}

values are expected to be largely due to measurement errors and electromagnetic radiative corrections. Figure 5.12 shows the correlation between Truth and Reconstructed values of Q^2 and x_{Bj}. The plots are restricted to the kinematic ranges of this analysis causing a zero-suppression on the x-axis. The fits to lines result in slopes ($A1$) ≈ 1 and offsets ($A0$) ≈ 0, indicating that no acceptance corrections for Q^2 and x_{Bj} are required.

- *Acceptance of the Particles.*

Acceptance corrections to the particle distributions are necessary because charged particles are swept out of the spectrometer acceptance by the magnetic fields and neutrals may be outside of the geometric acceptance of the calorimeter. Acceptance can be measured in a number of ways. Figure 5.13shows the Monte Carlo ratios of the number of particles observed in a given x_F bin after the detector simulation to the number before simulation. Based on this simulation, the detector does not have flat acceptance until $x_F = 0.1$. The overall acceptance ratio only reaches $\sim 75\%$, with losses in the region of full geometric acceptance due to undetected neutral hadrons, inefficiencies in the chambers and inefficiencies in pattern recognition.

If the detector had complete acceptance, then the total energy of the particles in the forward CMS would be expected to be approximately $W/2$ GeV. To see this, consider the CMS frame, where the proton is moving fast enough to use the approximation that the struck parton was carrying fraction x_{Bj} of the proton energy P and the target remnant was carrying $(1 - x_{Bj})P$. The energy of the proton and the incoming virtual photon are both equal to $W/2$ in this frame. Adding the energy of the incoming parent parton ($x_{Bj}W/2$) and the virtual photon ($W/2$), the struck quark will have energy $(x_{Bj} + 1)W/2$. For this analysis, $xbj < 0.04$, hence the struck parton which travels forward in the CMS has energy

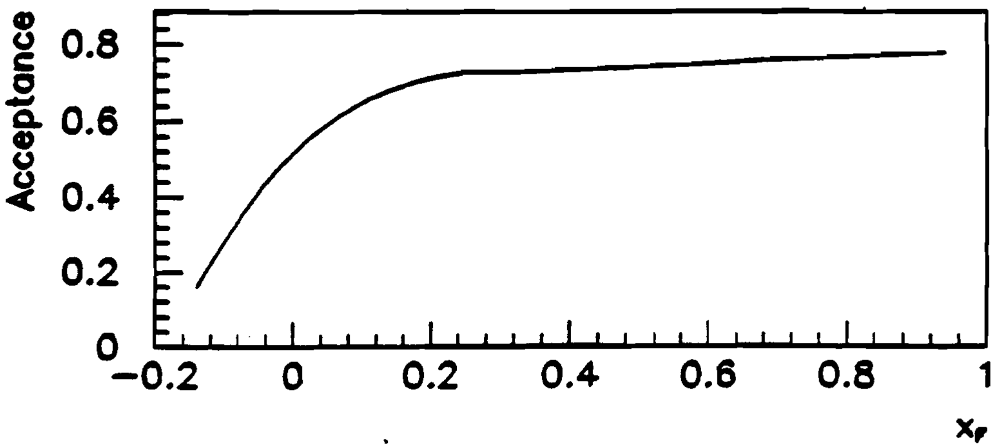

Figure 5.13. Monte Carlos prediction of acceptance of the spectrometer as a function of x_F

approximately equal to $W/2$. Thus the total energy of the observed particles (E_{obs}) in the forward CMS would be expected to be approximately $W/2$ given perfect acceptance. Figure 5.14 shows the distributions for $E_{obs}/(W/2)$ and $\langle E_{obs}/(W/2)\rangle$ versus Q^2 for the uncorrected particles with $x_F > 0$. The average value of the ratio is 75%, which is good in agreement with the level of the acceptance measured using the Monte Carlo (figure 5.13).

5.5 Summary of the Analysis Data Set

In summary, the cuts which define the data are:

Event Requirements:

- $W^2 > 400\ GeV^2$
- $Q^2 > 3\ GeV^2$
- $x_{Bj} > 0.003$
- $y < .80$
- $-12.0 < x_{vertex} < -10.2$

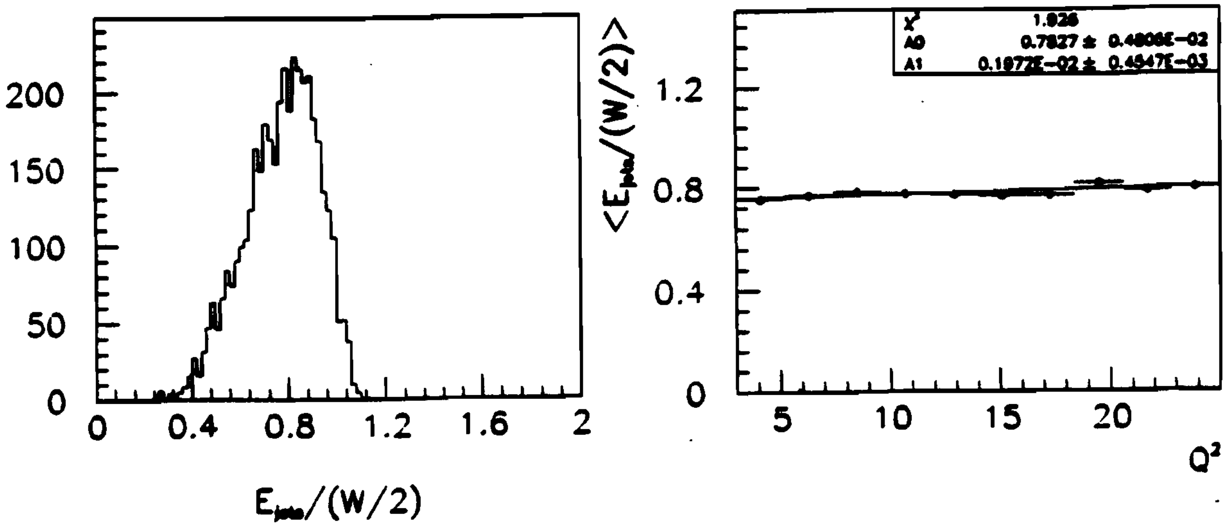

Figure 5.14. **a)** $E_{obs}/(W/2)$ distribution and **b)** $E_{obs}/(W/2)$ versus Q^2. The average value is expected to be $1/C$ for $\langle P_{T\ All}^2 \rangle$.

- Only one in-time incoming and outgoing muon track.
- Zero out-of-time incoming and outgoing muon tracks
- No events with $E_\gamma > 0.33 E_{Beam}$ w/i 30 cm of beam track projected to CAL
- No events with $\nu > 200\ GeV$ and $E_{Total}^{CAL}/\nu > .35$ and 0 hadron tracks
- No events with kinematically forbidden particles.

Track Requirements:

- $\chi^2_{prob} > .001$
- minimum distance of approach to vertex/error< 5.0
- $dP/P < 0.05$

Photon Requirements:

- Clusters within $-1.42 < Y < 1.42\ m$ and $-1.42 < Z < 1.42\ m$.
- No Clusters within $-1.42 < Y < -1.0\ m$ and $1.0 < Z < 1.42\ m$.
- $E_{Clus} \geq 5\ GeV$
- No track within 5, 7. 10 cm for the inner, middle and outer regions.

In conclusion, in this chapter The H_2 and D_2 data sets were shown to be compatible,

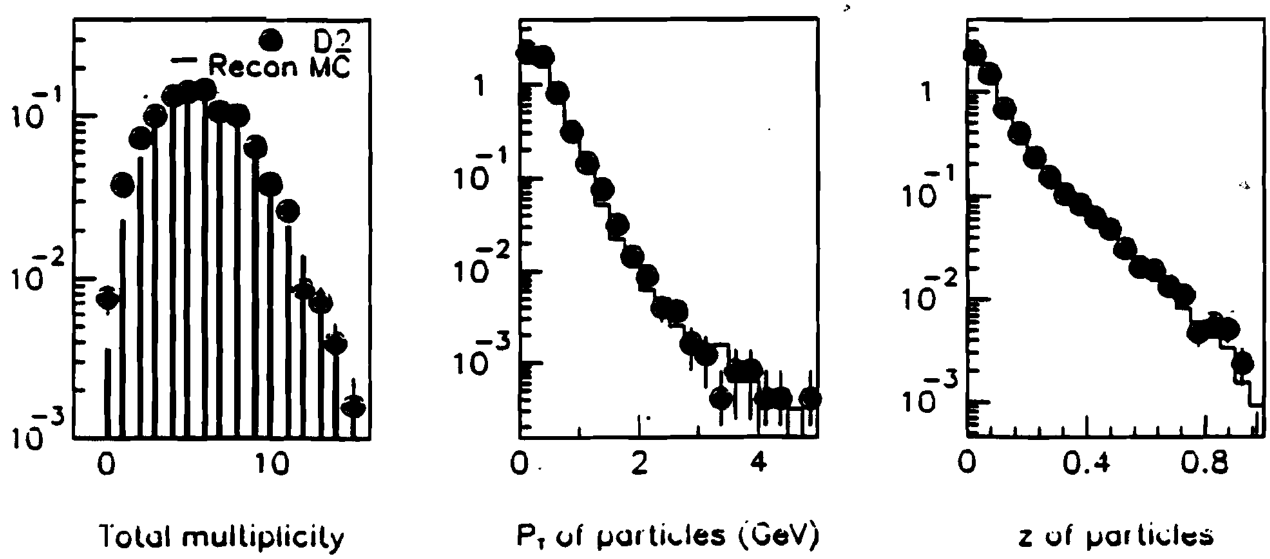

Figure 5.15. Comparison of all particles in data and reconstructed Monte Carlo: **a)** Multiplicity, **b)** Transverse Momentum, **c)**z.

resulting in 12,348 events for use in this analysis after the above cuts. The resulting multiplicity, transverse momentum and z distributions for all particles in the data compared to Monte Carlo are shown in figure 5.15. The reconstructed Monte Carlo agrees well enough with the data to permit accurate acceptance corrections.

Chapter 6

Characteristics of Identified Jets

This chapter presents the characteristics of the jets identified in the E665 data using the JADE Jet Algorithm. Both the uncorrected and acceptance corrected data are described in detail.

As discussed in chapters 1 and 3, three-lobed event structures, such as the one in figure I.2, may indicate an underlying 2+1 parton event. In order to explore this, the 2+1 jet events are compared to the exact Matrix Element PQCD calculation. Strong similarities between the jet distributions and parton-level predictions are observed.

The characteristics of the jets which affect the α_s analysis in chapter 7 are examined. These include the rate of production and the transverse momentum of 2+1 events. Measurements which are predicted to be related to the transverse momentum of the partons from PQCD effects ($P_{T\ QCD}$), the transverse momentum due to fragmentation ($P_{T\ frag}$) and the intrinsic transverse momentum (k_T) of the parent parton are presented. Emphasis is placed on understanding systematic effects from the acceptance correction which might bias the corrected data toward good agreement with the PQCD calculations.

In outline, this chapter will

- Review the JADE Jet Algorithm and its application to the uncorrected data.
- Describe of the jets identified in the E665 uncorrected data.
- Explain the acceptance correction method and its associated uncertainties.
- Apply the acceptance corrections and evaluation of further systematic errors to obtain the acceptance corrected results.
- Review those points in this chapter which are of particular relevance to the α_s analysis presented in the next chapter.

The following will refer frequently to section 3.3, on the expected sources of jet transverse momentum. These are summarized in appendix A. The discussion below is an extension of the analysis published by E665.[15] Slight differences between these rates and the published rates are due to different choices of kinematic requirements on the events and particles introduced to accommodate the analysis of chapter 7.

Complete history and documentation of this analysis, including the data tapes numbers which were used, is available in reference 118.

6.1 Application of the JADE Algorithm to Uncorrected Data

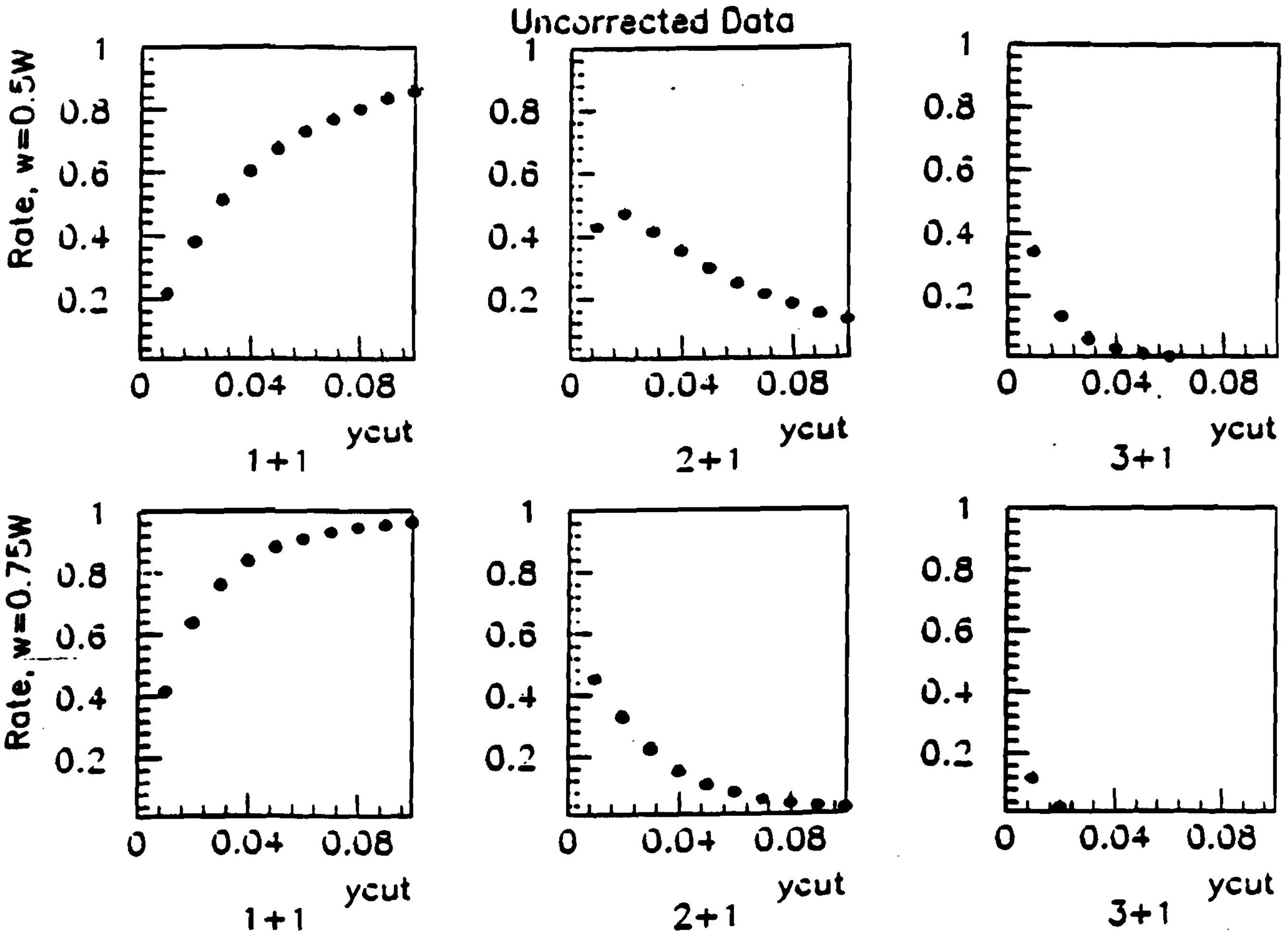

Figure 6.1. The jet rates in the uncorrected data. Fractional rates versus y_{cut} are presented. The columns show the 1+1, 2+1 and (3+)+1 jet rates, respectively. The rows correspond to jets identified with $\bar{w} = 0.5W$ and $\bar{w} = 0.75W$, respectively. The errors are assumed to be binomial and are too small to be visible on the plots. Note that in the uncorrected data the remnant jet is not observed.

The JADE Jet algorithm is applied to the uncorrected data in the following way:

1. For each pair of particles $y_{ij} \equiv (m_{ij}/\bar{w})^2$ is formed, where $\bar{w}$ is an energy scale characteristic of the event;
2. The pair with the minimum y_{ij} is selected;
3. The y_{ij} of the selected pair is compared to an arbitrary jet parameter, y_{cut};

4. If $y_{ij} < y_{cut}$, then the 4-vectors of the selected pair are combined, forming a single "quasi-particle;" The algorithm returns to step 1, including this quasi-particle in the set of particles used to form the y_{ij} in the next iteration;
5. When no pairs of (quasi-)particles remain which satisfy $y_{ij} < y_{cut}$, these remaining (quasi-)particles are each considered to be a jet.

(for comparison to the application at the parton and Truth levels, see sections 2.4 and 3.2, respectively).

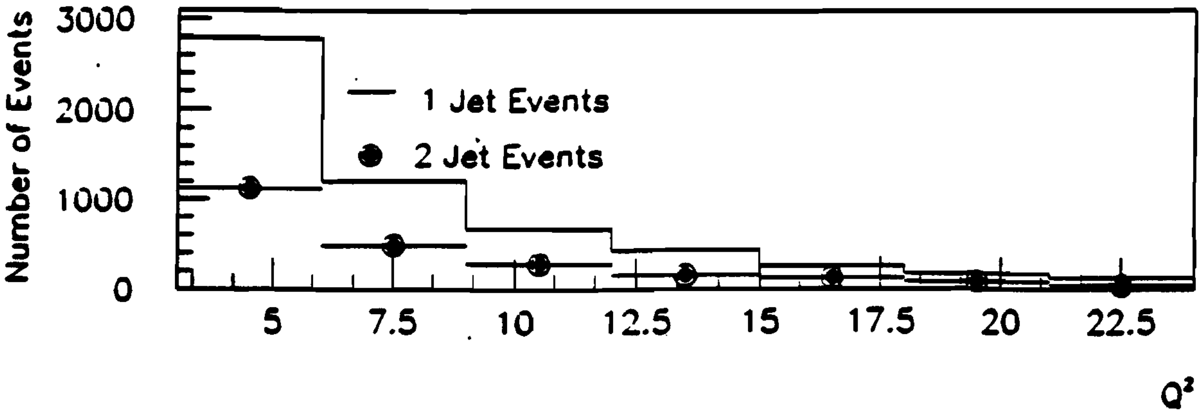

Figure 6.2. The statistics in each Q^2 bin used in this analysis, $\tilde{w} = 0.5W$, $y_{cut} = 0.04$. Dots — Number of 2+1 Jet events, Solid — Number of 1+1 jet events.

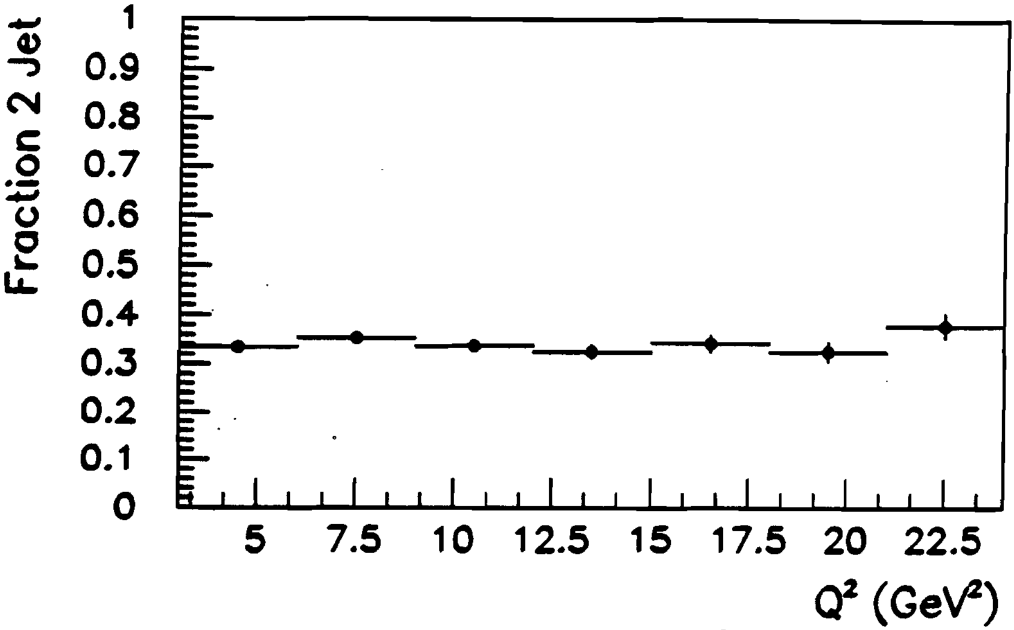

Figure 6.3. The uncorrected jet rates as a function of Q^2, $\tilde{w} = 0.5W$, $y_{cut} = 0.04$

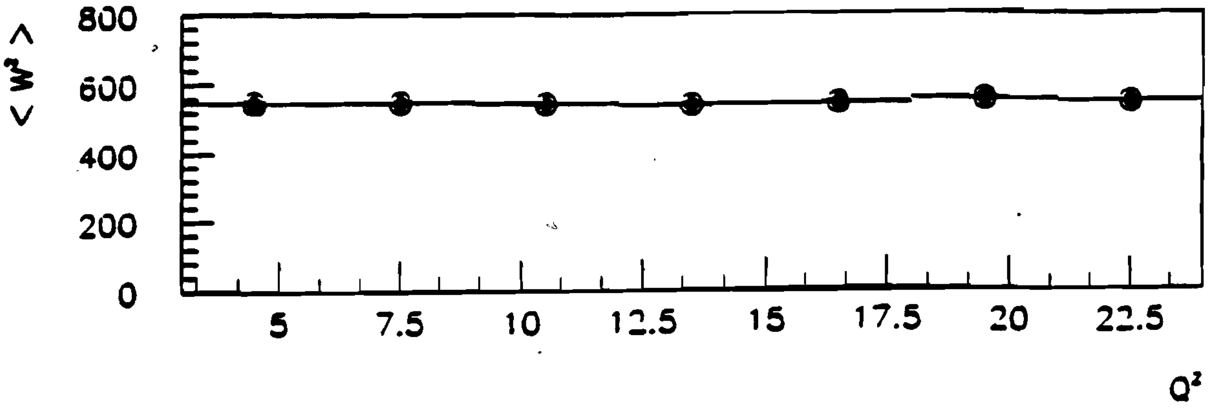

Figure 6.4. The $\langle W^2 \rangle$ in each Q^2 bin.

In the case of full acceptance ("Truth," described in section 3.4), the energy which scaled the invariant mass ($\tilde{w}$) was taken to be W. In the case of the reconstructed data, where only a fraction of the total energy is observed, $\tilde{w}$ must be chosen with consideration for the undetected energy. Two possible choices are considered for $\tilde{w}$ in the reconstructed data in this analysis. The first is $\tilde{w} = 0.75W$, where $\sim$ 75% is the fraction of the true energy detected in an event. The second is $\tilde{w} = 0.5W$, which minimizes the acceptance correction to most jet distributions including the α_s analysis in the following chapter. The differences in the characteristics of the uncorrected and corrected jets for these two choices is discussed in detail below. The variation in the corrected results is used to determine the sensitivity of this analysis to the choice of $\tilde{w}$.

6.2 The Uncorrected Jets

The uncorrected jet rates, as a fraction of the total events, are shown in figure 6.1 as a function of the jet defining parameter, y_{cut}. The rates are presented for 1+1, 2+1 and (3+)+1 events with energy scales $\tilde{w} = 0.5W$ and $\tilde{w} = 0.75W$. In the uncorrected data, the target remnant jet is not observed because the streamer chamber data is not used in this analysis (see section 4.4). It should be noted that varying $\tilde{w}$ is equivalent to changing the effective y_{cut} for a given value of W. That is, $(m_{ij}/(0.5W))^2 > 0.04$ is equivalent to $(m_{ij}/(0.75W))^2 > 0.04(0.5/0.75)^2 = 0.018$. Therefore, the jet rate for $\tilde{w} = 0.5W$ at $y_{cut} = 0.04$ is expected to be equivalent to the rate for $\tilde{w} = 0.75W$ at $y_{cut} = 0.018$, while the rate for $\tilde{w} = 0.75W$ at $y_{cut} = 0.04$ will be the same as for $\tilde{w} = 0.5W$ at $y_{cut} = 0.09$. Comparing the rates at $y_{cut} = 0.04$, approximately three times more jets are observed using $\tilde{w} = 0.5W$ than $\tilde{w} = 0.75W$.

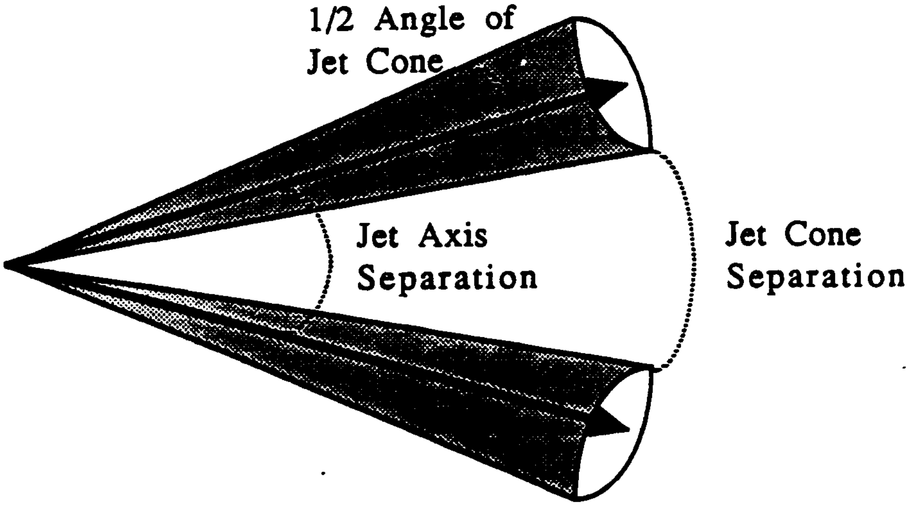

Figure 6.5. Schematic of the jets in the CMS. The solid arrows represent the jet axes. The shaded region represents the cone which contains 90% of the jet energy. The separation between the jet axes, the half-angle of the jet cone and the separation between the cones are shown.

In the analyses below and in the following chapter jet characteristics will be shown as a function of Q^2, therefore the number of events in each Q^2 bin must be considered. The statistics in seven Q^2 bins for at $y_{cut} = 0.04$ using $\tilde{w} = 0.5W$ are shown in figure 6.2. This is the statistical distribution of the data used in the final analyses. The uncorrected rates are shown as a function of Q^2 for $y_{cut} = 0.04$ and $\tilde{w} = 0.5W$ in figure 6.3.

Recalling that the JADE Algorithm uses W in the energy scale, if $\langle W^2 \rangle$ were Q^2 dependent, then the algorithm would introduce a Q^2 dependence into the jet characteristics. However, figure 6.4 shows that $\langle W^2 \rangle$ is independent of Q^2 in the range of these analyses. This is uncorrected data.

$y_{cut} = 0.04$ will be used to define the jets in the following discussion. At $y_{cut} = 0.04$, the contribution of (3+)+1 jet events is negligible. Therefore, only the characteristics of 1+1 and 2+1 events are discussed. Table 6.1 summarizes the characteristics of the uncorrected jets for $\tilde{w} = 0.5W$ and $y_{cut} = 0.04$. Figure 6.5 defines three angles which will be discussed below and appear in table 6.1. Note that the average multiplicity and momentum from table 6.1 are comparable to the 3 jet events first reported at PETRA, which averaged approximately 4 particles and 6 GeV (in CMS) per jet.[5]

The JADE Algorithm introduces an effective cut on the possible opening angle, θ, of the non-remnant jets in 2+1 jet events. To see this, recall that, in order to find 2+1 jets, the algorithm requires

$$2E_{jet\ 1}E_{jet\ 2}(1 - cos\theta)/\tilde{w}^2 > y_{cut}$$

If y_{cut} is nonzero and there is a maximum limit to $E_{jet\ 1}E_{jet\ 2}$, then this necessarily

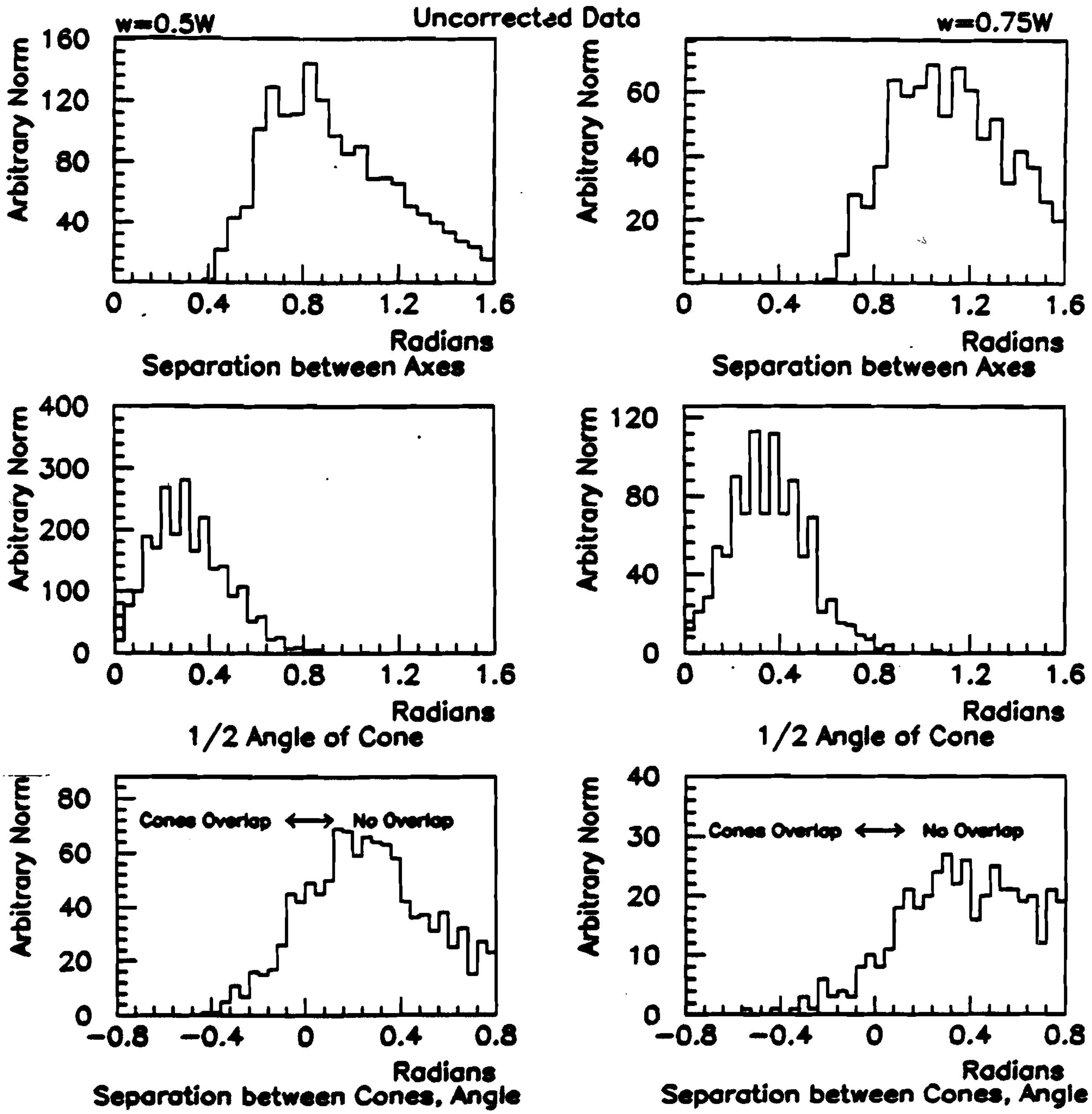

Figure 6.6. For 2+1 events, uncorrected data, **a)** The opening angle between the two non-remnant jets axes, $\bar{w} = 0.5W$, **b)** Opening angle for $\bar{w} = 0.75W$, **c)** The half angle of cone (90% of jet energy) of each jet, $\bar{w} = 0.5W$, **d)** Half angle of cone, $\bar{w} = 0.75W$. **e)** The angular separation between the two jet cones (negative values indicate overlapping jet cones, positive values indicate separated jet cones), $\bar{w} = 0.5W$, **f)** Angular separation between cones, $\bar{w} = 0.75W$,

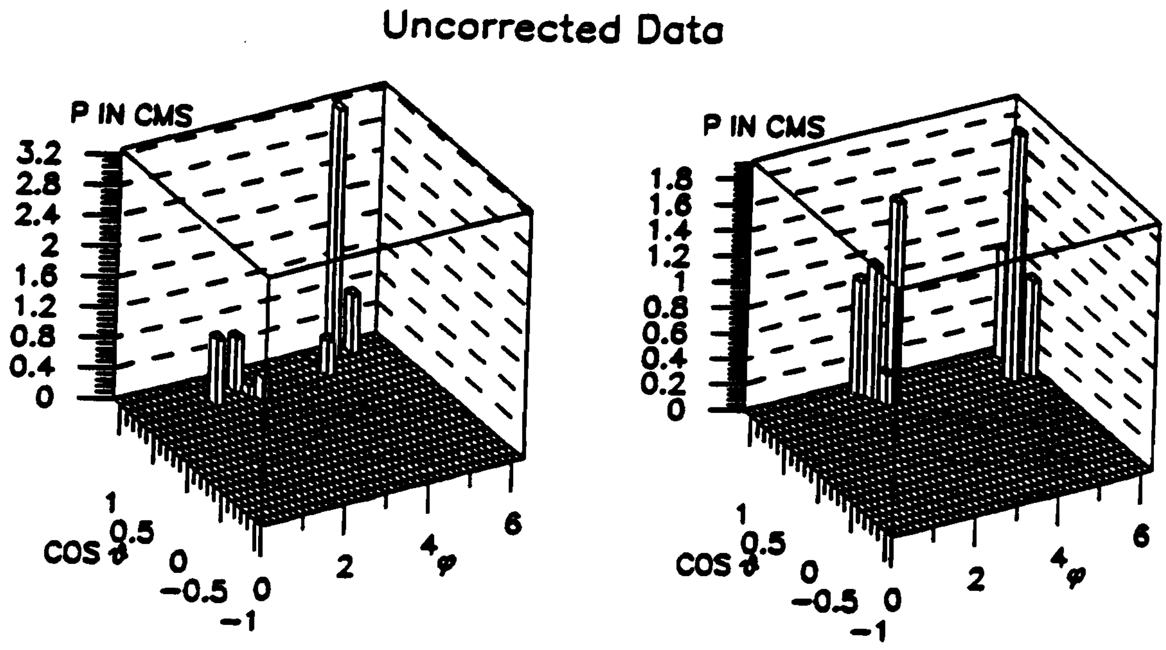

Figure 6.7. Two examples of 2+1 jet events identified with $\tilde{w} = 0.5W$ at $y_{cut} = 0.04$. The negative $cos\theta$ region corresponds to the backward CMS, where the E665 forward spectrometer has no acceptance.

corresponds to a minimum limit on $(1 - cos\theta)$ and a corresponding minimum to θ. The maximum limit on $E_{jet\ 1}E_{jet\ 2}$ is the result of the requirement that $E_{jet\ 1} + E_{jet\ 2} \approx W/2$ in the CMS leading to $E_{jet\ 1}E_{jet\ 2} = E_{jet\ 1}(W/2 - E_{jet\ 1})$. This maximum occurs at $E_{jet\ 1} = E_{jet\ 2} = W/4$. In the case of $y_{cut} = 0.04$ and $\tilde{w} = 0.05W$, then $(1 - cos\theta) > 0.92$ or $\theta > 0.4$ *rad*. This effect can be seen in figures 6.6a and b which show the opening angle between the jet axes for a random sub-sample of the 2+1 jet events. Note that in this figure the first column corresponds to $y_{cut} = 0.04$ and $\tilde{w} = 0.05W$ and the second column shows $y_{cut} = 0.04$ for $\tilde{w} = 0.75W$.

The particles assigned to the jet form a cone about the jet axis, as shown schematically in figure 6.5. Two jet events tend to consist of two collimated streams of particles plus one or two very low energy particles between the jets. The jet cone is defined as the cone which contains 90% of the jet energy, thereby excluding these low energy particles. The distributions of one half of the opening angle of the jet cone is shown in figures 6.6c and d.

The separation between the jet cones may be defined as the angular separation between the particle from jet a and the particle from jet b which are closest in space. This separation is shown in figures 6.6e and f. Negative values of separation indicate that the cones overlap, while positive values indicate separation. Most of the observed jets are well separated at $y_{cut} = 0.04$.

This separation can be observed in figure 6.7. These examples, chosen to be typical rather then "the best," are the first two 2+1 events at $y_{cut} = 0.04$ defined by $\tilde{w} = 0.5W$

Characteristic (Per Uncorrected Jet)	1 Jet	2 Jets
<Multiplicity >	6.0	4.3
<Multiplicity in Cone>	4.8	3.7
<CMS Momentum>	6.8 GeV	4.5 GeV
<Squared Transverse Momentum>	0.9 GeV^2	1.7 GeV^2

Table 6.1. Characteristics of the 1+1 and 2+1 jet events in the uncorrected data

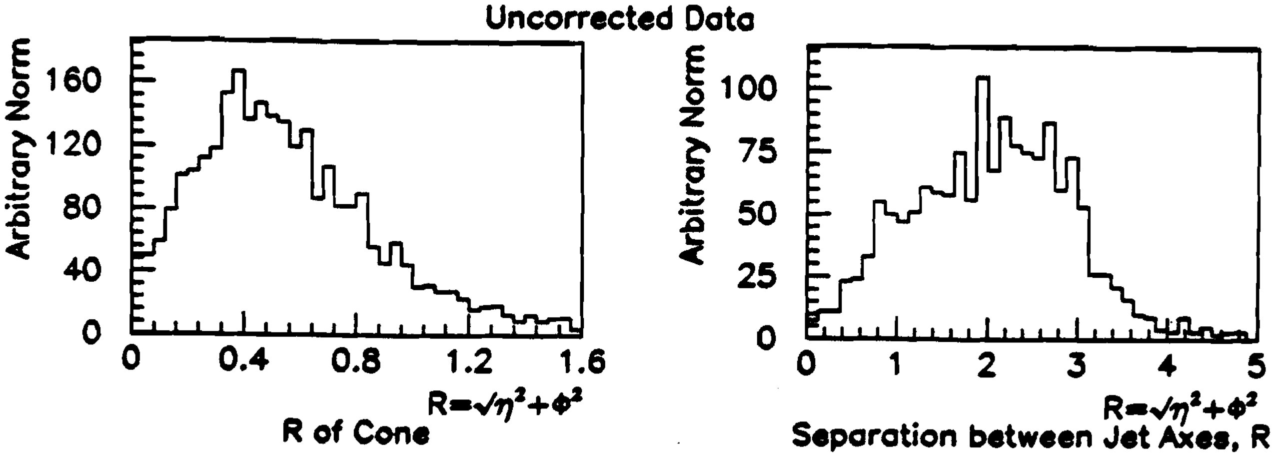

Figure 6.8. The identified jets from the Hadron Collider viewpoint: **a)** R for the jets observed in the E665 Data, **b)** Separation between the jet axes in units of R for the E665 data.

from a deuterium DST tape. In this figure, θ is measured from the virtual photon axis, ϕ is measured about the virtual photon axis, and each particle is entered weighted by its momentum in the CMS. Note that no particles are observable in the backward CMS (negative $cos\phi$) region where the target remnant is expected. Recall from the discussion in section 3.3 that misassignment of particles between jets is expected to reduce the transverse momentum of both jets. Therefore, significant separation is desired to reduce this effect.

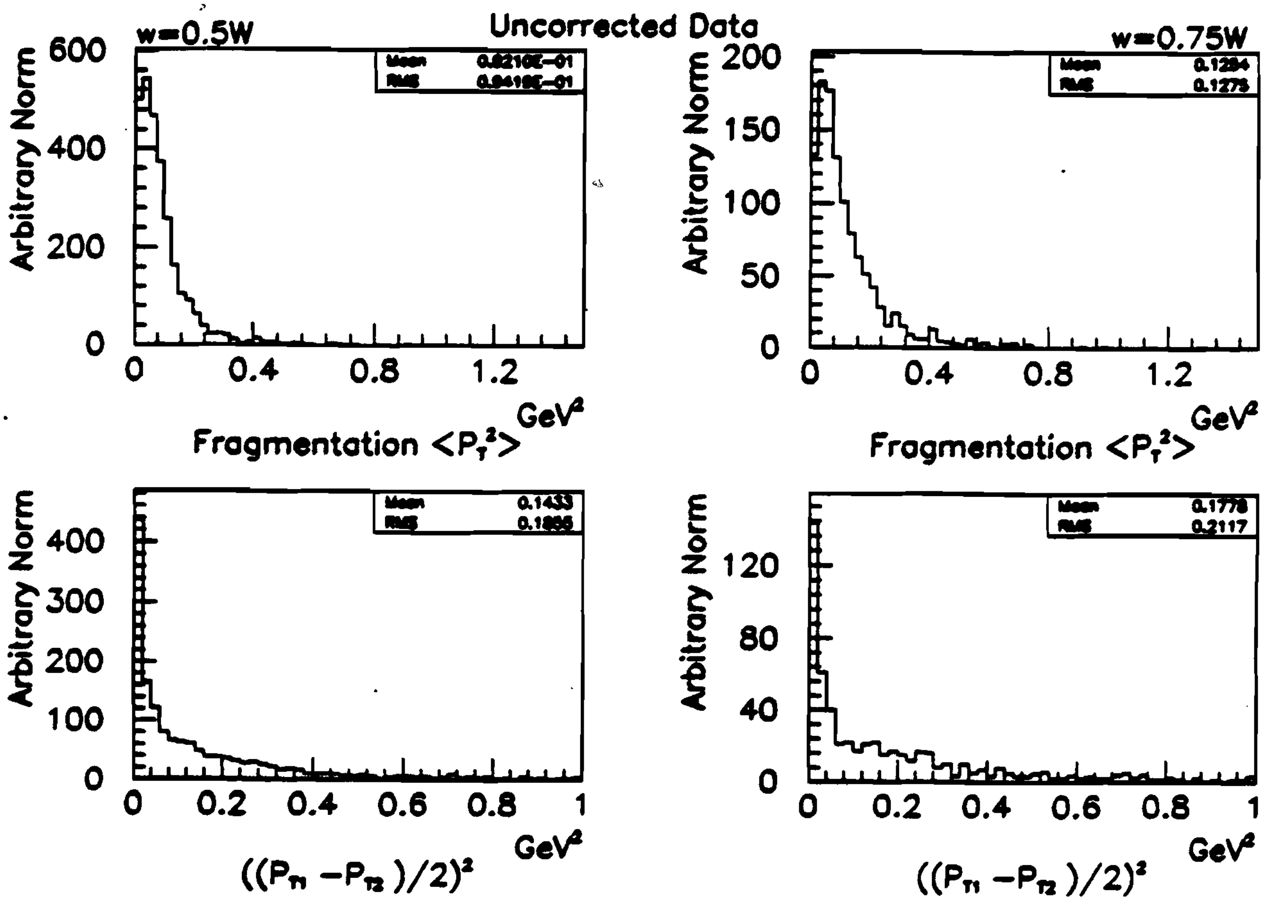

Figure 6.9. For 2+1 jets, at $y_{cut} = 0.04$ with $\bar{w} = 0.5W$ (column 1) and $\bar{w} = 0.75W$ (column 2) **a)** and **b)** The $\langle P^2_{Tpcl} \rangle$ of particles within the jet, measured with respect to the jet axis, expected to be equal to the transverse momentum from fragmentation; **c)** and **d)** The difference between the transverse momenta of the 2 jets, expected to be due to both fragmentation and intrinsic transverse momentum effects.

While the JADE Jet Algorithm was under development in e^+e^- experiments, hadron collider experiments created a different favorite algorithm[63] based on a two-dimensional space defined by pseudorapidity, $\eta = -\ln(tan\theta/2)$, and ϕ, the azimuthal angle about the incoming beam axis. In this algorithm, a jet consists of the particles within a cone of radius $R = \sqrt{\Delta\eta^2 + \Delta\phi^2}$, about an axis determined by weighted transverse energy observed in the calorimetry of the experiment. R is the jet defining parameter (similar in function to y_{cut} in the JADE Jet Algorithm) and the theoretically favored choice is $R = 0.7$ (for analogous reasons to the choice of $y_{cut} = 0.04$ in the JADE Algorithm, described in sections

2.4, 2.5, 3.5 and below). For an E665 jet identified using the JADE Algorithm to have been observed using the hadron collider algorithm, the particles must be in a cone of $R < 0.7$ about the jet axis.

Figure 6.8a shows the R of the jet cones in the 2+1 events defined at $y_{cut} = 0.04$ with $\bar{w} = 0.5W$. Two differences between the collider application of this algorithm and the R presented here should be noted: 1) the lower CMS momentum particles observed in E665 might not be observed in the collider experiment calorimetry and 2) the jet axis is defined by the 4-vector of the particles in the cone, not the the center of gravity of an energy deposit in a calorimeter. Approximately two thirds of the E665 2+1 jet events pass the hadron collider jet definition. Figure 6.8b shows the separation between the two jet axes, identified using the JADE Jet Algorithm, in units of R.

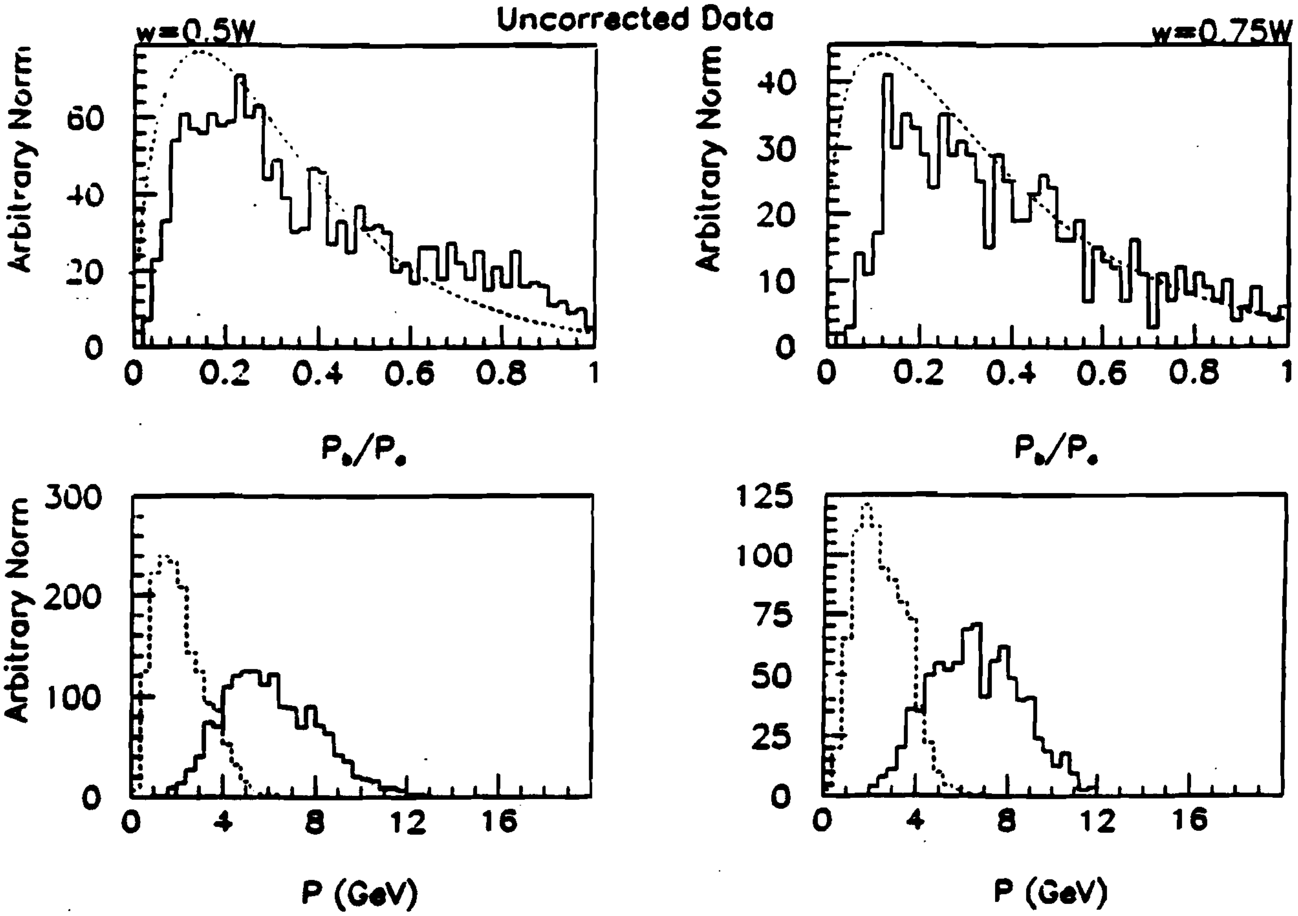

Figure 6.10. a) and b) The ratio of lowest to highest momentum jet in 2+1 events. Dashed curve: the parton level prediction. If jets reflect an underlying 2+1 parton event, there should be agreement for the larger values of the ratio, where acceptance is flat. c) and d)The momentum distributions: Solid— E665 Uncorrected Data, Dash— Parton Level Prediction

Recall that the JADE Jet Algorithm was introduced at the parton level to regulate the divergences in the 2+1 cross section. One such divergence is due to the 2+1 parton cases having one parton with very low energy compared to the other. The result is that production of 2+1 parton events with highly asymmetric momenta is favored. The analogy to this at the hadronic level is expected to be an asymmetry in the momenta of the two nonremnant jets in 2+1 jet events. If jet a is defined to be the highest momentum jet, then the ratio of the momenta of the two jets, P_b/P_a, is shown in figure 6.10 by the solid line. If one assumes that the momentum acceptance correction is flat for reasonably large values of P_b, then the correction factor would cancel in the ratio, allowing direct comparison to the expectation at the parton level. The parton-level prediction, shown by the dashed curve on figure 6.10, has a similar shape to the data except at small values of P_b/P_a where deviations are expected due to acceptance. Also shown in figure 6.10 are the momentum distributions of the jets, with jet a shown by the solid and jet b shown by the dashed lines.

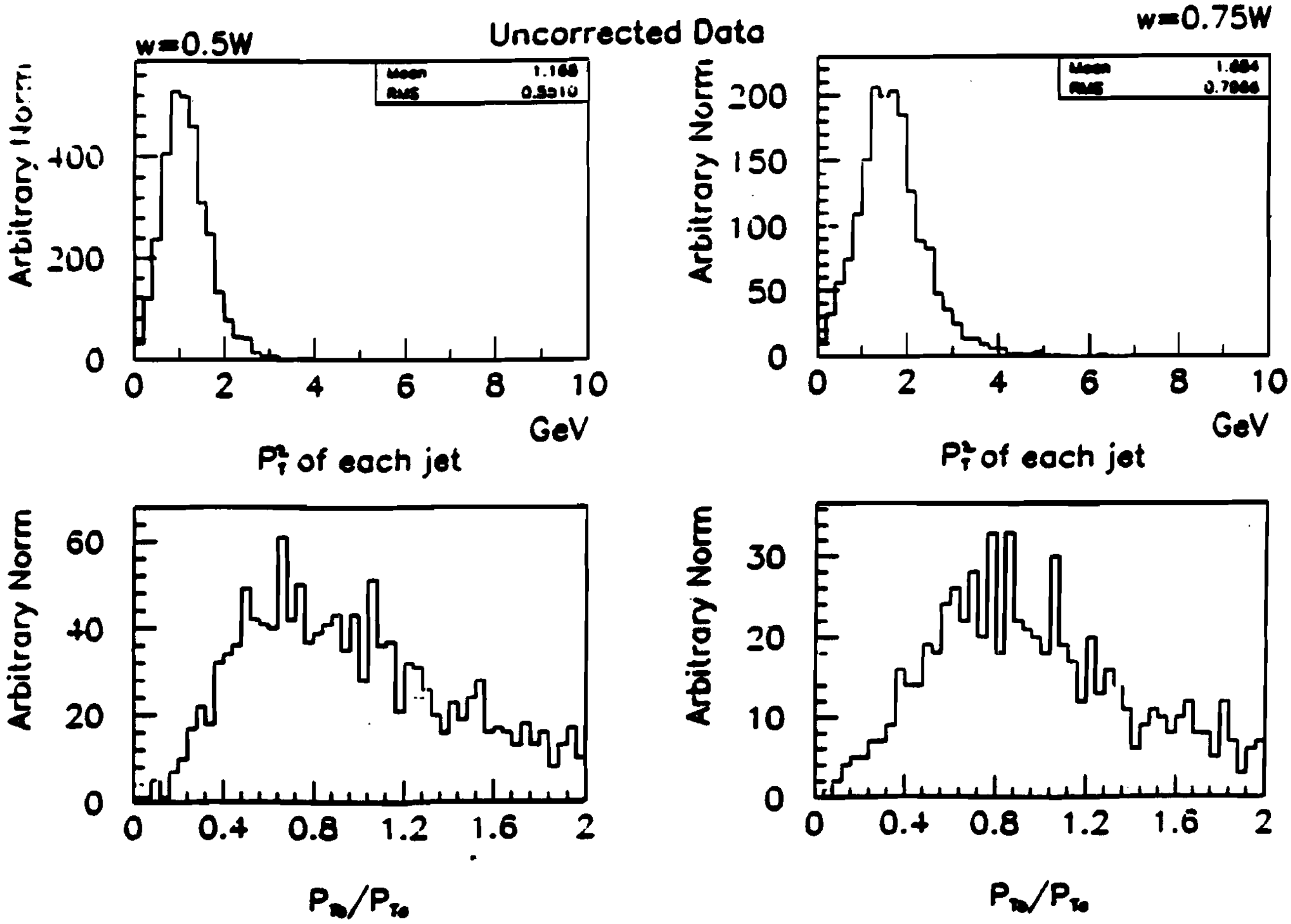

Figure 6.11. a) and b) The uncorrected squared transverse momentum distributions of the jets measured with respect to the virtual photon axis. One entry for each jet. c) and d) Ratio $P_{T\ jet\ b}/P_{T\ jet\ a}$.

The transverse momentum of particles within the jets with respect to the jet axis is predicted to result from fragmentation. In figures 6.9a and b; the $\langle P_T^2 \rangle$ with respect to the jet axis is shown for each jet in each event for the two energy scales. Below, the corrected values of this distribution will be compared to the e^+e^- measurements.

The transverse momentum of the jet vector magnitudes, $P_{T\ jet\ a}$ and $P_{T\ jet\ b}$ measured with respect to the jet axis in 2+1 jet events, at $y_{cut} = 0.04$, for the two energy scales are shown in figure 6.11. The ratio of $P_{T\ jet\ b}/P_{T\ jet\ a}$, where jet a has the highest momentum, is also shown. If the jet momentum were only due to the underlying PQCD processes, then the ratio would be expected to be one. The fact that the ratio is not sharply peaked at one may be attributed mainly to fragmentation, intrinsic momentum and acceptance effects, since the angular separation at $y_{cut} = 0.04$ appears to be sufficient to prevent significant misassignment of particles ("cross-talk") between the jets (see section 3.3).

The difference between the transverse momta of the two jets is expected to be due to fragmentation and intrinsic transverse momentum in the event in the acceptance corrected data. The crux of the argument, presented in section 3.3, is that one expects:

$$\frac{\frac{\pi}{4}(\langle P_{T\ frag}^2 \rangle + \langle k_T^2 \rangle)}{2} = \langle (\frac{P_{T\ jet\ a} - P_{T\ jet\ b}}{2})^2 \rangle \qquad (3.8)$$

The uncorrected distribution of $((P_{T\ jet\ a} - P_{T\ jet\ b})/2)^2$ is shown in figure 6.9c and d. After acceptance corrections, this distribution, combined with the measurement of $\langle P_{T\ frag}^2 \rangle$ permits evaluation of $\langle k_T^2 \rangle$. This will be presented below.

In chapter 7, the transverse momentum of the jets due to PQCD processes as a function of Q^2 is used. Recall the definition from section 3.3,

$$P_{T\ 2\ jet} = \frac{P_{T\ jet\ a} + P_{T\ jet\ b}}{2},$$

where for each jet (a and b) the transverse momentum is measured with respect to the virtual photon axis. This is expected to be the jet-level analog to the parton-level variable $P_{T\ QCD}$ of section 3.3, which approximates the PQCD contribution to the transverse momentum of 2+1 events (P_T of chapter 1). Figures 6.11a and b show the squared transverse momentum distributions for the two energy scales. The average values are 1.6 GeV^2 and 2.9 GeV^2, respectively. The difference between the average values is a reflection of the fact that $\langle P_{T\ 2\ jet}^2 \rangle$ depends on the choice of y_{cut} as shown in figures 6.11c and d. This dependence is an effect of the algorithm, not the acceptance, so it remains in the corrected data. Therefore, one can only discuss $\langle P_{T\ 2\ jet}^2 \rangle$ as related to a specific y_{cut}. In fact, as will be shown in the next chapter, the y_{cut} dependence of the transverse momentum is well described by the y_{cut} dependence of the integral in equation 2.9, therefore the y_{cut} dependence will cancel when equation 3.10 is evaluated. Finally, figures 6.11e and f show the variation of $\langle P_{T\ 2\ jet}^2 \rangle$ as a function of Q^2 for $y_{cut} = 0.04$.

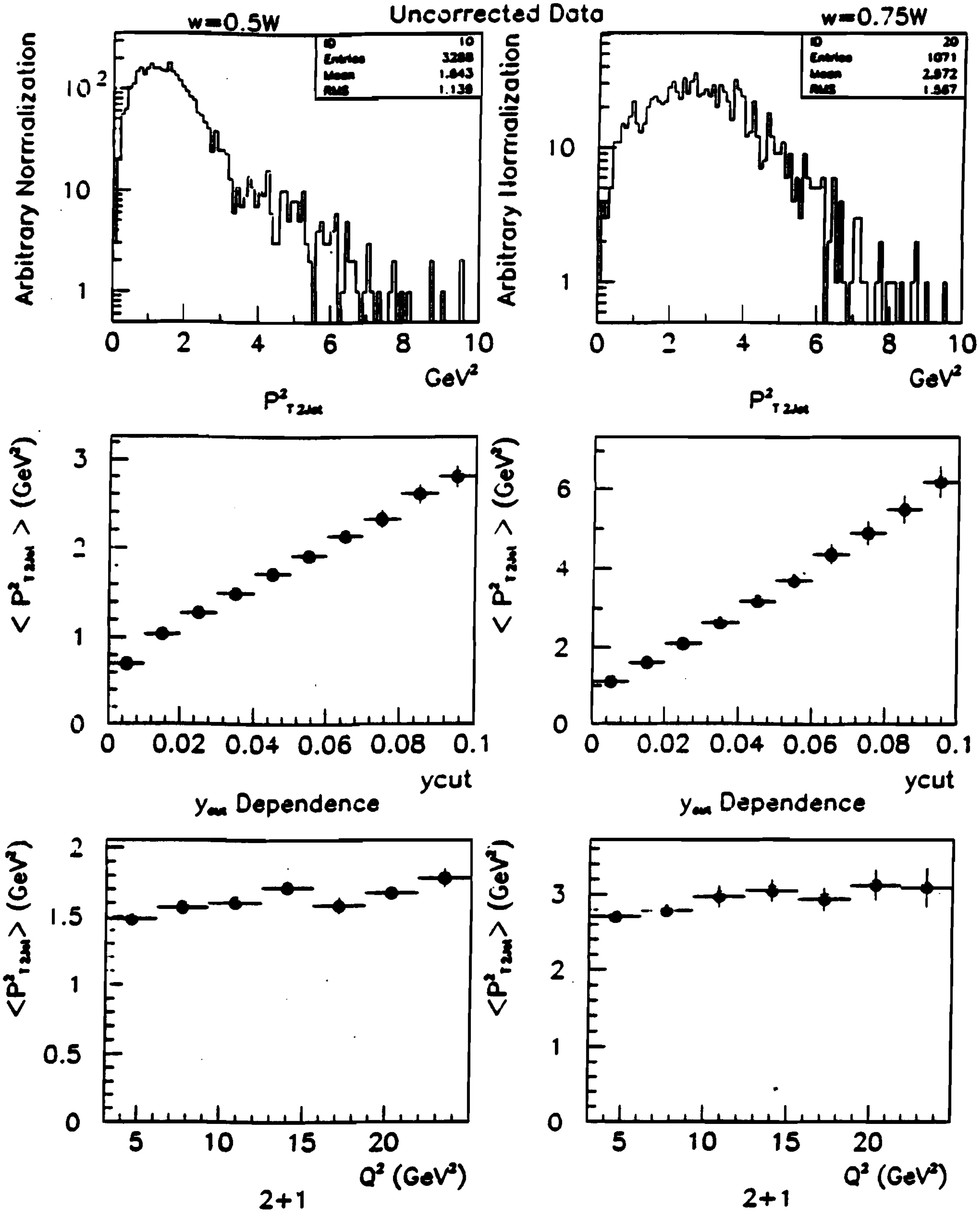

Figure 6.12. $P_{T\ 2\ jet}^2$ distributions of jets in 2+1 events. **a)** and **b)** Event distribution, **c)** and **d)** $\langle P_{T\ 2\ jet}^2 \rangle$ vs. y_{cut}, **e)** and **f)** $\langle P_{T\ 2\ jet}^2 \rangle$ vs. Q^2

6.3 The Acceptance Correction and Its Uncertainty

This section describes the method for determining the acceptance corrections to the distributions shown in the following analysis and the uncertainties which result. Specific applications will be shown in the section on the corrected data, below.

Monte Carlo data generated by Lepto 5.2 (Matrix Element), Jetset 6.3, and Gamrad, with full detector simulation, as described in chapters 3 and 4, were used for performing the acceptance corrections. These data sets had various values of Λ_{QCD} and exponents of the gluon distribution, but the acceptance correction from each set agreed within errors. Therefore the sets were combined in order to obtain high statistics.

Two types of corrections will be considered. First, corrections which cause migrations of events between bins along the x-axis of the plots. Second, corrections to the y-axis variables which change the normalization within a bin.

For x-axis corrections, the following correction function was determined using Monte Carlo:

$$C = 1 + \frac{\langle T - R \rangle}{R}$$

where T is the true variable value and R is the reconstructed value. C is determined as a function of R. Therefore, if D is the uncorrected value of the x-axis variable, and C is the value of the correction function evaluated at D, then the entry at D migrates to bin CD in the corrected histogram.

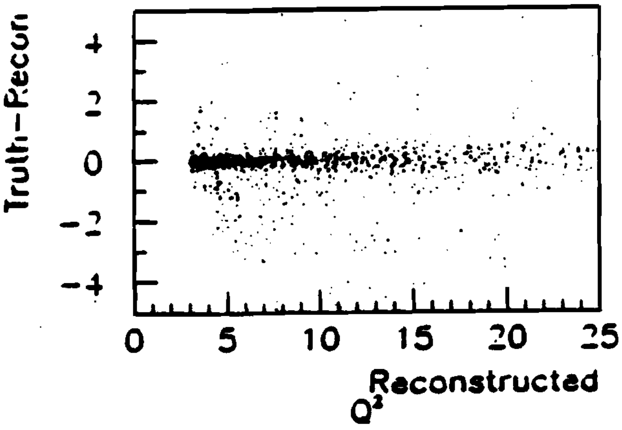

Figure 6.13. $T - R$ vs. R for Q^2.

In the case of distributions plotted versus Q^2, the x-axis correction is very small. Figure 6.13 shows the difference between T and R values as a function of R for Q^2. The correction function is negligible because the spectrometer has full acceptance for the muon in the kinematic range of this analysis and because, due to the event cuts in the previous chapter, radiative events represent only ~ 10% of the total event sample. Although the value of $\langle T-R \rangle$ is negligible, there is a significant spread. In light of this, no correction will be made to Q^2, however, the effect of systematic shifts of $Q^2 \pm 0.5$ GeV^2 will be considered in the determination of the systematic error.

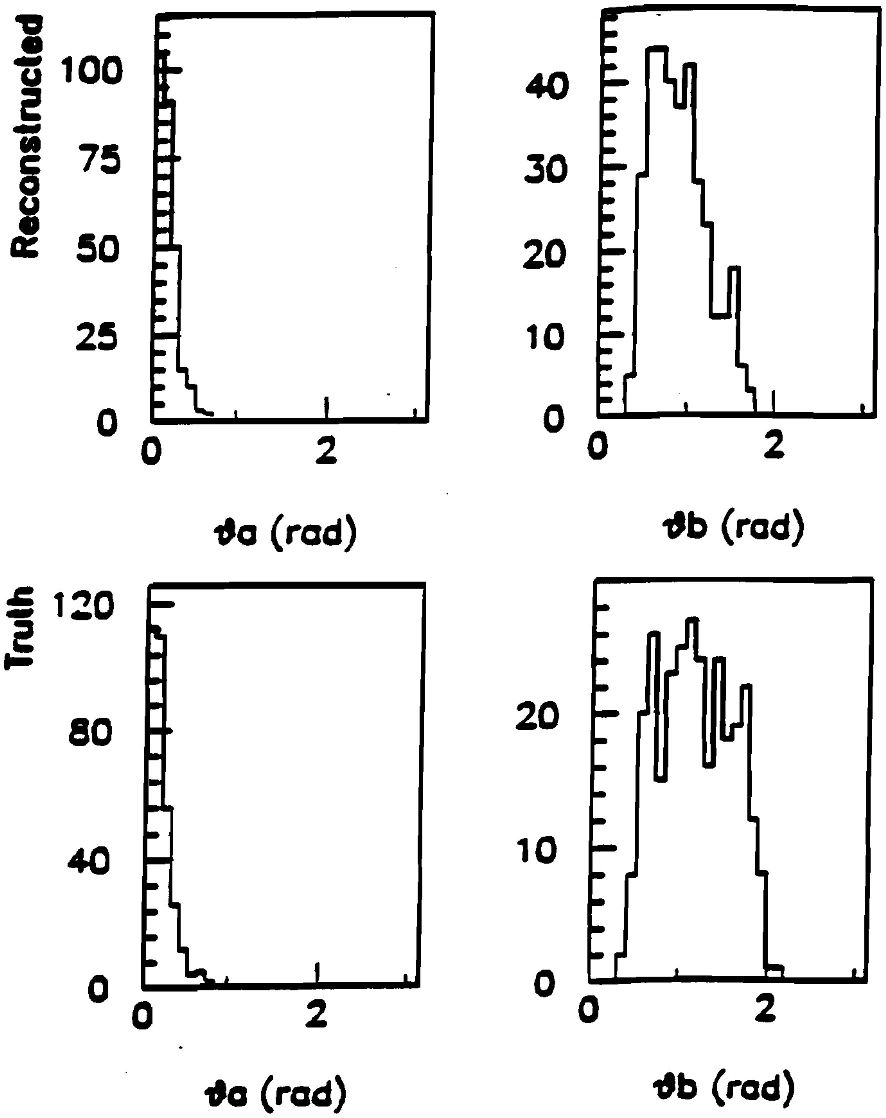

Figure 6.14. Comparison of the angle between jet vector and virtual photon axis in Truth and Reconstructed Monte Carlo (see figure 3.2). The highest momentum jet is a. Upper row is Monte Carlo Reconstructed, lower is Truth. For reconstructed data $\bar{w} = 0.5W$ is shown.

For corrections to the y-axis variables, if D is the y-axis value to be corrected, T is the same y-axis expectation from Monte Carlo Truth, R is the same from Monte Carlo

Reconstructed, and C is the correction function, then

$$\frac{T}{R}D = CD = Corrected\ Data.$$

The correction C is applied x-bin-by-x-bin to the data.

It is important to note that due to detector acceptance the jets in the reconstructed distribution have a maximum angle with respect to the virtual photon axis of 1.85 *rad*, while jets in the Truth data are found to have maximum angle of 2.05 *rad*. Figure 6.14 illustrates this point.

For the "final" distributions presented in this analysis, jets were identified at $y_{cut} = 0.04$ with $\tilde{w} = 0.5W$ and were corrected using the standard E665 Monte Carlo with experimentally measured efficiencies for chambers and the Matrix Element Physics generator. Data corrected in this way are called the "standard" data below.

The acceptance correction uncertainties in these distributions are due to the fitting procedure, the choice of $\tilde{w}$ in the reconstructed jet algorithm, the quality of the model of the chambers in the reconstructed data, and the residual effects of the underlying physics generator in the Monte Carlo. The sources and method for evaluating each uncertainty are discussed here and the magnitude of these uncertainties for the physics distribution is presented in association with each plot.

- *Uncertainty in the fit*

In some cases, the acceptance correction will be obtained from fits to the function $C = T/R$. These fits will have an associated statistical error. The associated error will be assigned as a systematic uncertainty in the analysis.

- *Choice of* $\tilde{w}$

In the previous section the uncorrected jet characteristics were presented for two possible choices of $\tilde{w}$: $\tilde{w} = 0.5W$, which was found to minimize the acceptance corrections to the jet rates; and $\tilde{w} = 0.75W$, where 0.75 is approximately the fraction of the total energy that is observed by the E665 detector in the regions of flat acceptance, and which minimizes the correction to $\langle P_{T\ 2\ jet}\rangle$. $\tilde{w} = 0.5W$ is used for the "final" results. The systematic uncertainty assigned due to "energy scale" or $\tilde{w}$, in the analysis below is the difference between the corrected results for $\tilde{w} = 0.5W$ and $\tilde{w} = 0.75W$.

As discussed above, using $\tilde{w} = 0.75W$ at $y_{cut} = 0.04$ is equivalent to doing the $\tilde{w} = 0.5$ analysis at $y_{cut} = 0.09$. So the uncertainty on the acceptance correction from doing the same analysis at a very different y_{cut} is identical to the "energy scale" uncertainty.

- *Model of the Detectors*

Careful studies of the model for chamber and calorimeter efficiencies used in the Reconstructed Monte Carlo have been presented in references 96 and 119. The efficiency of the chambers were modeled at approximately one month intervals. Between intervals the change in the measured efficiency of the chambers was ~ 2.5%. Individual dead wires were included in the model. The model is expected to represent the efficiency of each

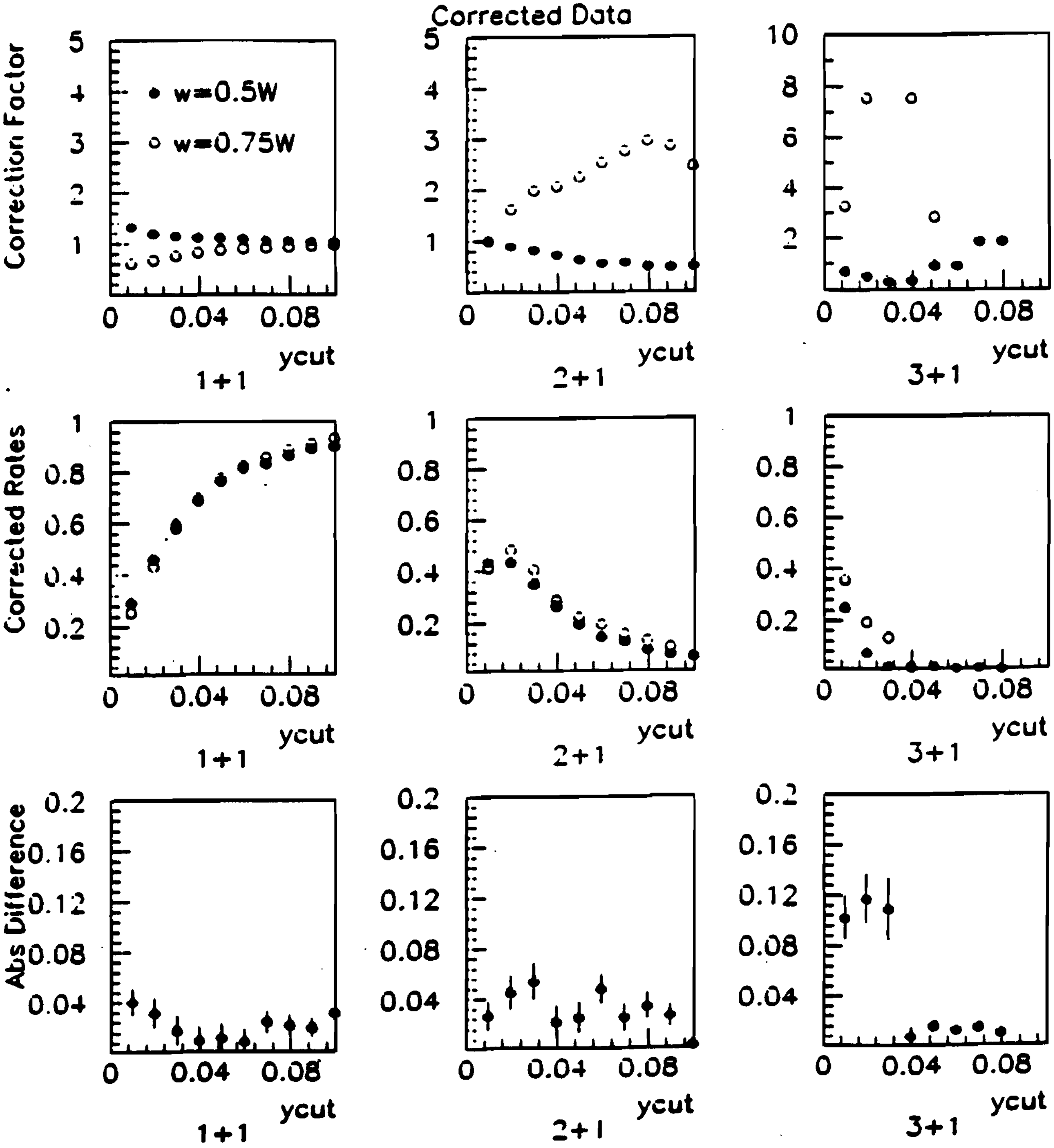

Figure 6.15. The Corrected Jet Rates: Uncertainty due to energy scale.

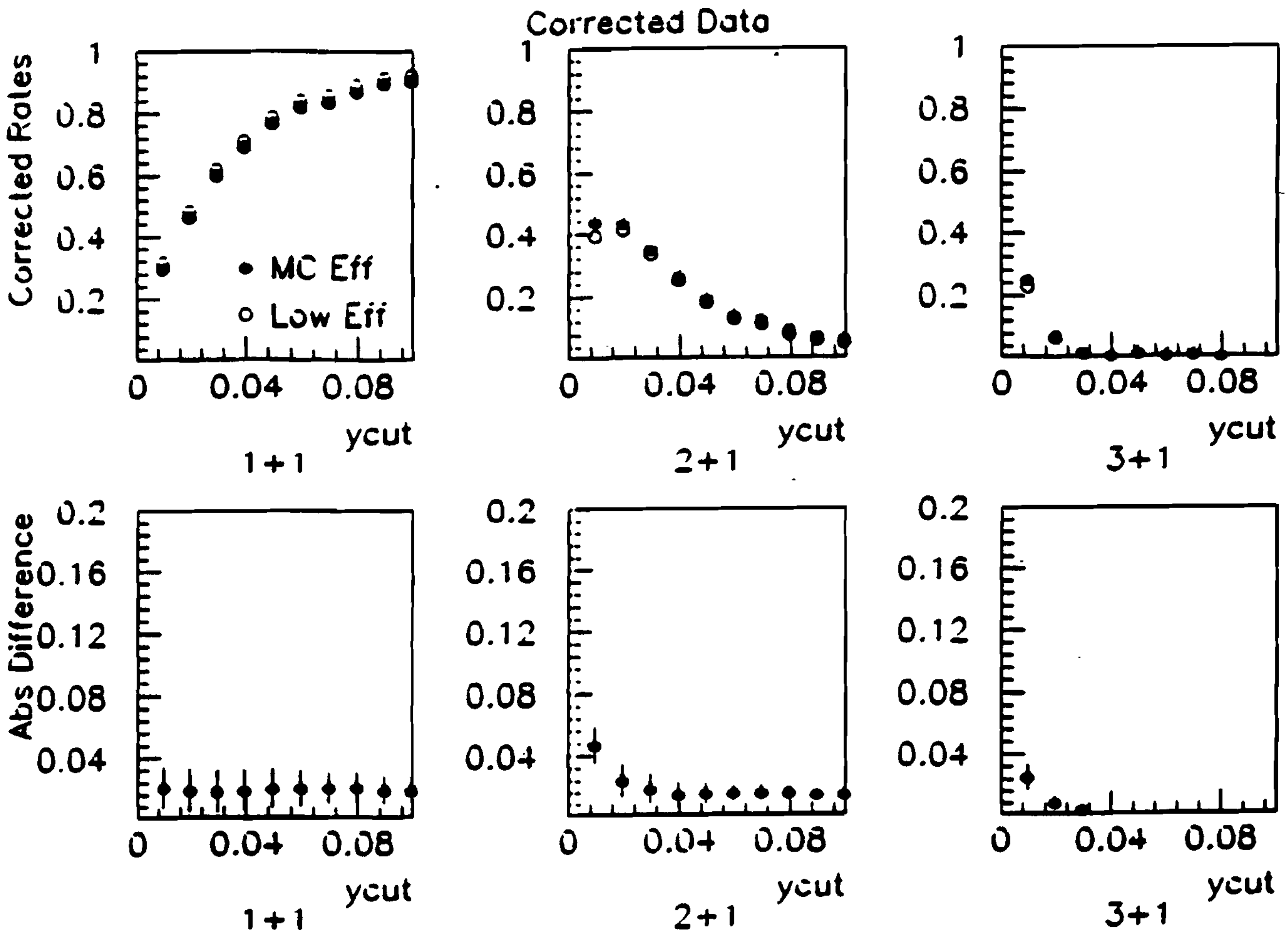

Figure 6.16. The Corrected Jet Rates: Uncertainty due to chamber model.

chambers to better than 5%. The global efficiency of the calorimeter was modeled, but individual dead regions were not. The quality of the chamber modelling is reflected in the agreement between reconstructed Monte Carlo and data physics distributions in the previous chapter.

Incorrect modelling of the detector will lead to an incorrect determination of C. In order to study the sensitivity of C to inefficiencies that were incorrectly simulated, two tests were performed. First, 5% of the particles (charged and neutral) were randomly dropped from the Reconstructed Monte Carlo data sample. Second, all tracks with hits within $-0.16 < Y < -0.08$ m and $-0.2 < Z < 0.0$ m at the second set of drift chambers were eliminated for the reconstructed sample. This simulates a correlated inefficiency observed in a portion of the data set used in this analysis and described in reference 99. This inefficiency was not observed in this analysis (see section 4.5 for further discussion). However, on the principle that it is best to be conservative, this study was included. The variation in C due to these changes in chamber modelling is quoted as the uncertainty due to "chamber model," below.

- *Physics Generator in the Monte Carlo*

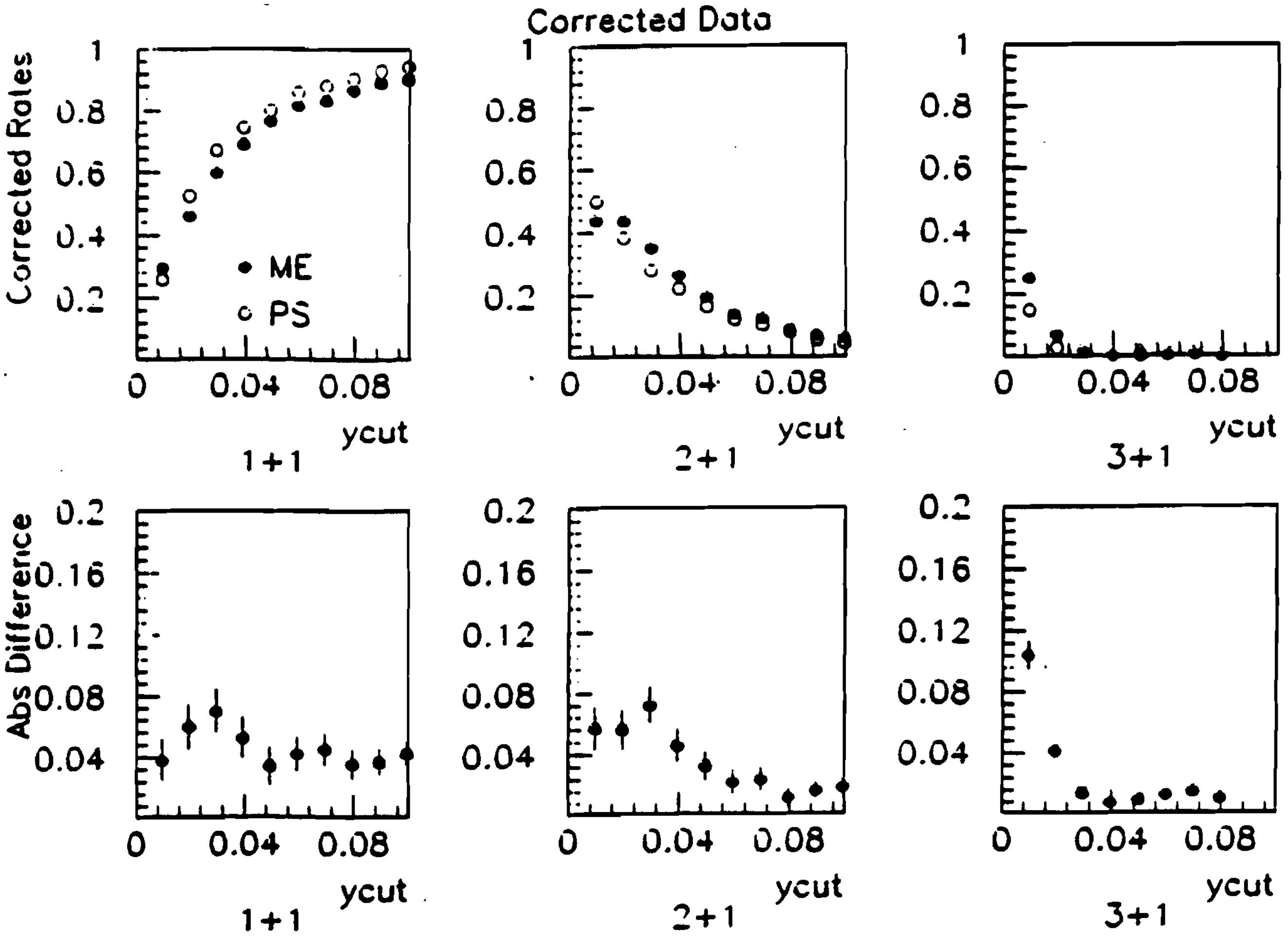

Figure 6.17. The Corrected Jet Rates: Uncertainty due to physics generator.

In principle, any underlying physics generator may be used in the Monte Carlo to the extent that residual effects from the generator cancel in the ratio. In practice, this may not be true, and the residual effects could bias the corrected data toward agreement with the Monte Carlo Generator. This study is designed to estimate the magnitude of any residual effects.

The exact matrix element calculation through terms proportional to α_s is used in the "standard" correction of the data. In order to test the sensitivity to the underlying physics in the Monte Carlo, the acceptance correction using the standard physics generator will be compared to corrections from a second physics generator available in the Lund Monte Carlo (Jetset 6.3), called the "Parton Shower" model. This uses a leading logarithm approximation to simulate higher order effects: outgoing partons bremsstrahlung or split into a $q\bar{q}$ pair if there is sufficient energy for the newly created parton pair to have $y_{cut} > 0.0025$ and $m_{ij}^2 > 2\ GeV^2$. This showering process is iterated until no outgoing partons can produce pairs which pass the cut. Then the Lund string fragmentation is applied. The Parton Shower generator is thought to be sufficiently different from the first order matrix element calculation in the standard E665 Monte Carlo to be used to test whether the acceptance correction, C, depends on the underlying physics generator. The variation due to using different physics generators is quoted as the uncertainty from the "generator," below.

6.4 The Corrected Jets

In this section, the acceptance corrected jet characteristics are presented. Corrections to the rates and transverse momenta of the jets are discussed in detail. The fragmentation transverse momentum is measured. The transverse momentum from the combined effects of fragmentation and intrinsic transverse momentum is extracted. With these two pieces of information, a value of intrinsic transverse momentum is obtained.

- *The Corrected Jet Rates*

As a first example of the acceptance correction procedure and determination of the uncertainty due to this method, consider the jet rates. The top row of figure 6.15 shows the acceptance corrections, C, to the jet rates for $\tilde{w} = 0.5W$ and $\tilde{w} = 0.75W$. Note that using $\tilde{w} = 0.5W$ results in correction factors which are almost unity. The correction factors are applied to the uncorrected data y_{cut}-bin-by- y_{cut}-bin, without first fitting the Monte Carlo, giving the corrected jet rates shown in the second row of figure 6.15. The third row shows the absolute difference between the corrected rates for the two cases — the uncertainty due to energy scale.

Using the case $\tilde{w} = 0.5W$, now consider the effect of the chamber modelling. In figure 6.16, data with the standard Monte Carlo correction are compared to the result with varied chamber efficiencies in the top row of plots. The absolute difference between the corrected rates is shown in the bottom row of plots. The change in the rate is caused mainly by the correlated inefficiency. Finally, the corrected rates determined using the standard "Matrix Element" physics generator and the "Parton Shower" physics generator are shown on the top row of figure 6.17. The absolute difference between the corrected results from the two generators is shown in the bottom row of figure 6.17.

The final 1+1 and 2+1 corrected rates are shown in figure 6.18 as a function of the algorithm parameter y_{cut}. The statistical error, barely visible on the data points, is binomial: $\sqrt{p(1-p)/N_{entries}}$. The shaded area at the bottom of the plots shows the total

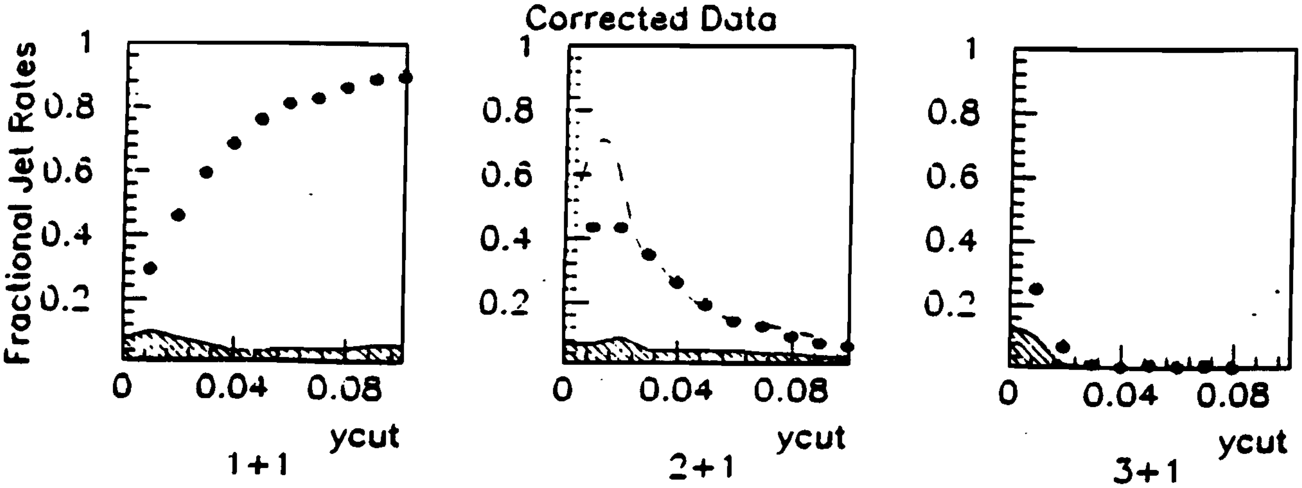

Figure 6.18. The Corrected Jet Rates

uncertainty obtained by adding the individual uncertainties in quadrature. The dashed curve on the 2+1 jet plot shows the PQCD predicted 2+1 parton rates. The shape is similar to the jet distribution except at low values of y_{cut}, where the algorithm is unreliable at both the parton and the jet level, as discussed in section 1.12.

In order to determine the corrected rate distribution as a function of Q^2 for $y_{cut} = 0.04$, the acceptance corrections shown in figure 6.19 were used. As an example of this correction technique, the T, R and $C = T/R$ distributions are shown. A linear fit to the C distribution provides the acceptance correction function. This correction factor is applied to the data shown in figure 6.4.

Figure 6.20 shows the corrected jet rates as a function of Q^2. The associated systematic errors are shown by the shaded region at the bottom of the plot. The line shows a fit to the parton-level output of the Monte Carlo, with α_s varied to fit the first data point. As discussed in section 3.4, the Monte Carlo parton-level output has been shown to be in agreement with the PQCD calculations used in chapter 2. The line lies systematically below the data, however the difference is within the estimated systematic uncertainty. This will be discussed further below.

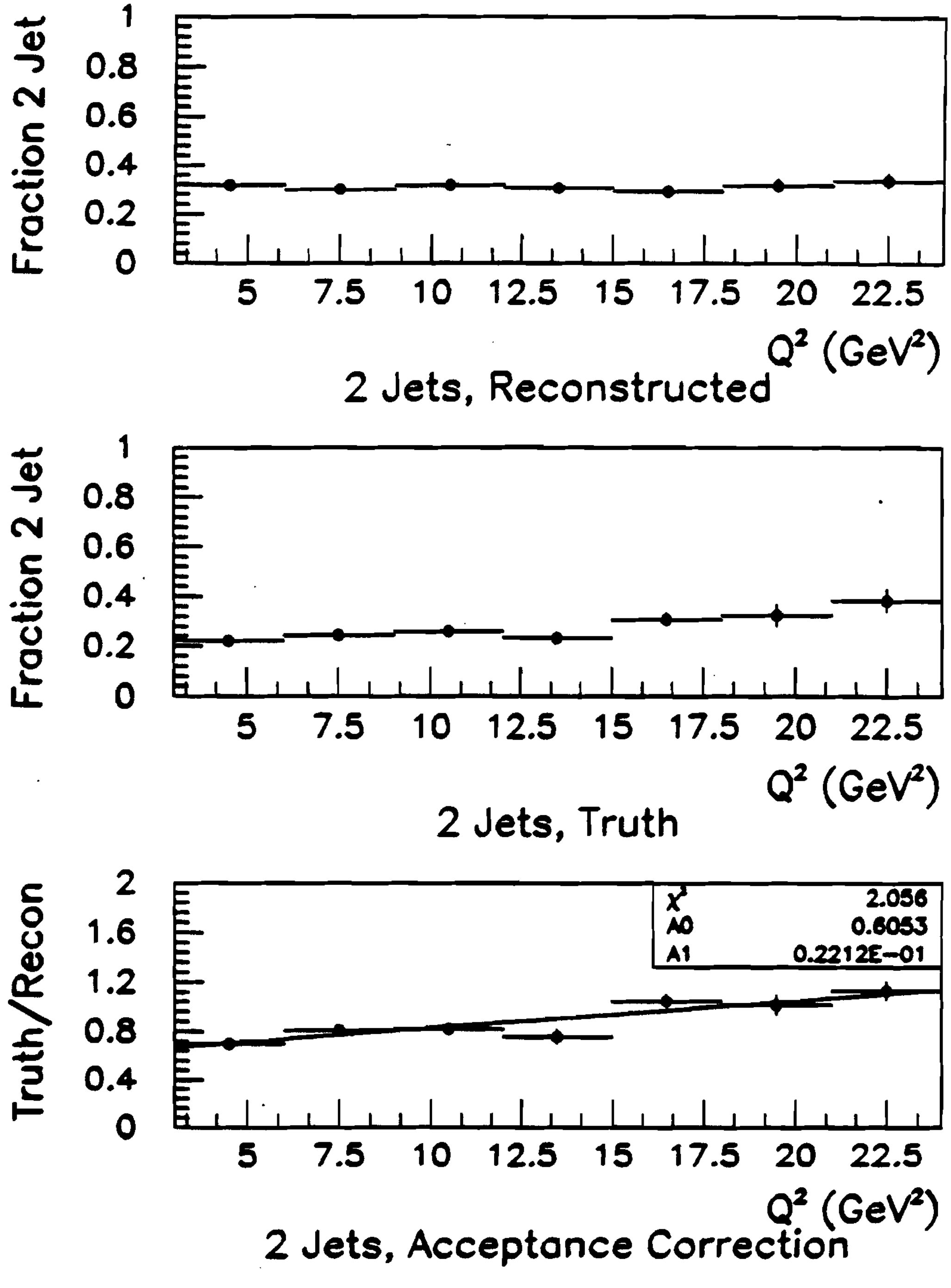

Figure 6.19. The acceptance corrections factors for the jet rates as a function of Q^2. $y_{cut} = 0.04$. As an example of the correction procedure, the T, R and $C = T/R$ distributions are shown. The distributions are fit to obtain the acceptance correction function.

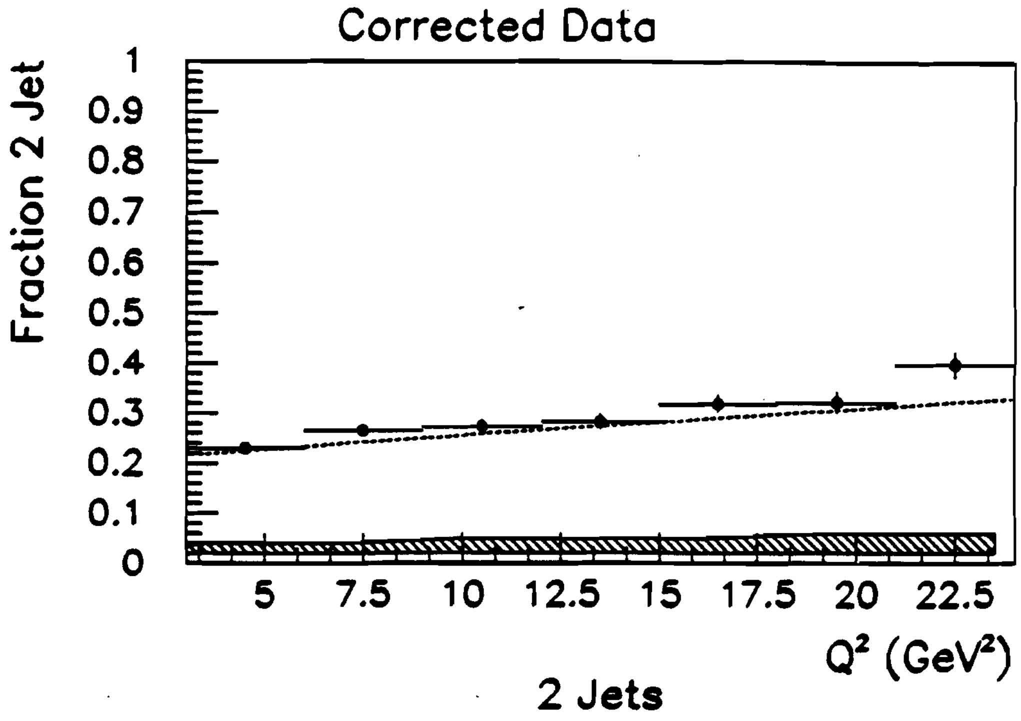

Figure 6.20. The corrected 2−1 jet rates versus Q^2. The line shows the PQCD prediction. See Text.

- *The Corrected Jet Transverse Momenta*

Figure 6.21 shows the correction distribution for $\langle P_{T\ 2\ jet}^2\rangle$ *vs.* Q^2 for the "Standard" corrected data. A very small negative correction to the Q^2 dependence is expected since radiative corrections lead to an effective rotation of the virtual photon axis. Using the derivation in reference 120, one expects:

$$\langle P_{T\ rad}^2\rangle \approx 0.25\frac{\alpha}{\pi}Q^2[\ln(Q^2/m_\mu^2) - 1],$$

which is, within error, the observed dependence. The systematic effects which were found to cause significant variation to the corrected $\langle P_{T\ 2\ jet}\rangle$ were: the energy scale (~ 5%), the physics generator (~ 5%) and shifts in Q^2 of $\pm 0.5\ GeV^2$ (~ 2%). These are shown in figure 6.22a. Although it is likely that most of the variations in Q^2 shown in figure 6.22a are due to insufficient statistics in the data and the Monte Carlo, this cannot be proved, therefore these uncertainties will be assumed to be Q^2-dependent.

For each source of Q^2 uncertainty listed above, a linear fit was made to the distribution. The difference between the linear fit and the data points was considered to be the magnitude of the uncertainty. The uncertainties from the sources were added in quadrature. This reduced random fluctuations from poor statistics. Finally, the uncertainty from the statistical error from the linear fit from the acceptance correction was also added in quadrature.

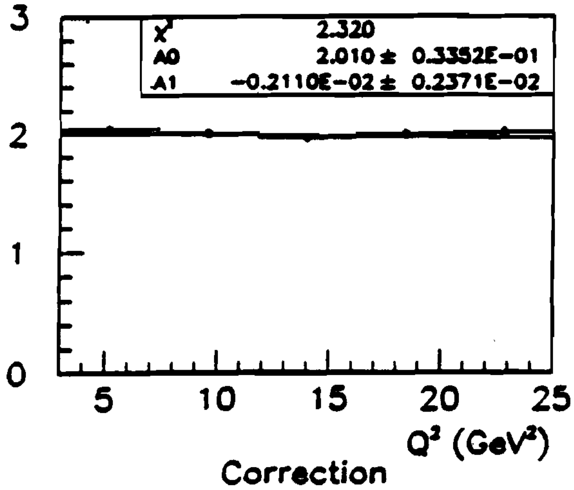

Figure 6.21. The acceptance corrections factor for the transverse momentum of the 2+1 jet events using the Standard Monte Carlo.

Imprecise calibration of the spectrometer could lead to two further systematic mismeasurements. First, an uncertainty of 4% is assigned for a maximum possible 2% miscalibration of the magnetic fields of the forward spectrometer. Second, an uncertainty must be assigned for a possible systematic mismeasurement of the momentum of the incoming muon. This manifests itself as a difference in the incoming and outgoing measured muon energies in events where the muon did not interact. Evidence for a ~ 10 *GeV* offset is documented in references 99 and 97. If the reconstructed incoming muon energy is increased by 10 *GeV* in the Monte Carlo and the event variables are changed accordingly, the $\langle P_{T\ 2\ jet}^2\rangle$ is changed by 1%. Both of these systematic uncertainties affect only the overall normalization of the data points. These uncertainties are added in quadrature.

Figure 6.22b shows the corrected measurement of $\langle P_{T\ 2\ jet}^2\rangle$ as a function of Q^2 for the E665 data. The statistical error shown on the data points is defined as $\sigma/\sqrt{N_{entries}}$, where σ is the standard deviation of the distribution from the mean. The total Q^2-dependent uncertainty is shown in the shaded region at the bottom of the figure. The magnitude of the normalization uncertainty is indicated by the double-arrow at the right side of the figure. The PQCD expectation is shown by the curve. The value of α_s has been set by the 2+1 jet rate (figure 6.20). The data lie systematically below the curve. This may be due to cross-talk between the jets (see section 3.3), which is expected to systematically lower $\langle P_{T\ 2\ jet}^2\rangle$. Or this may indicate an effect which systematically increases the 2+1 jet rate and decreases $\langle P_{T\ 2\ jet}^2\rangle$, such as higher order corrections (see section 2.5). Because the deviations lie within the systematic uncertainty, no conclusions can be drawn.

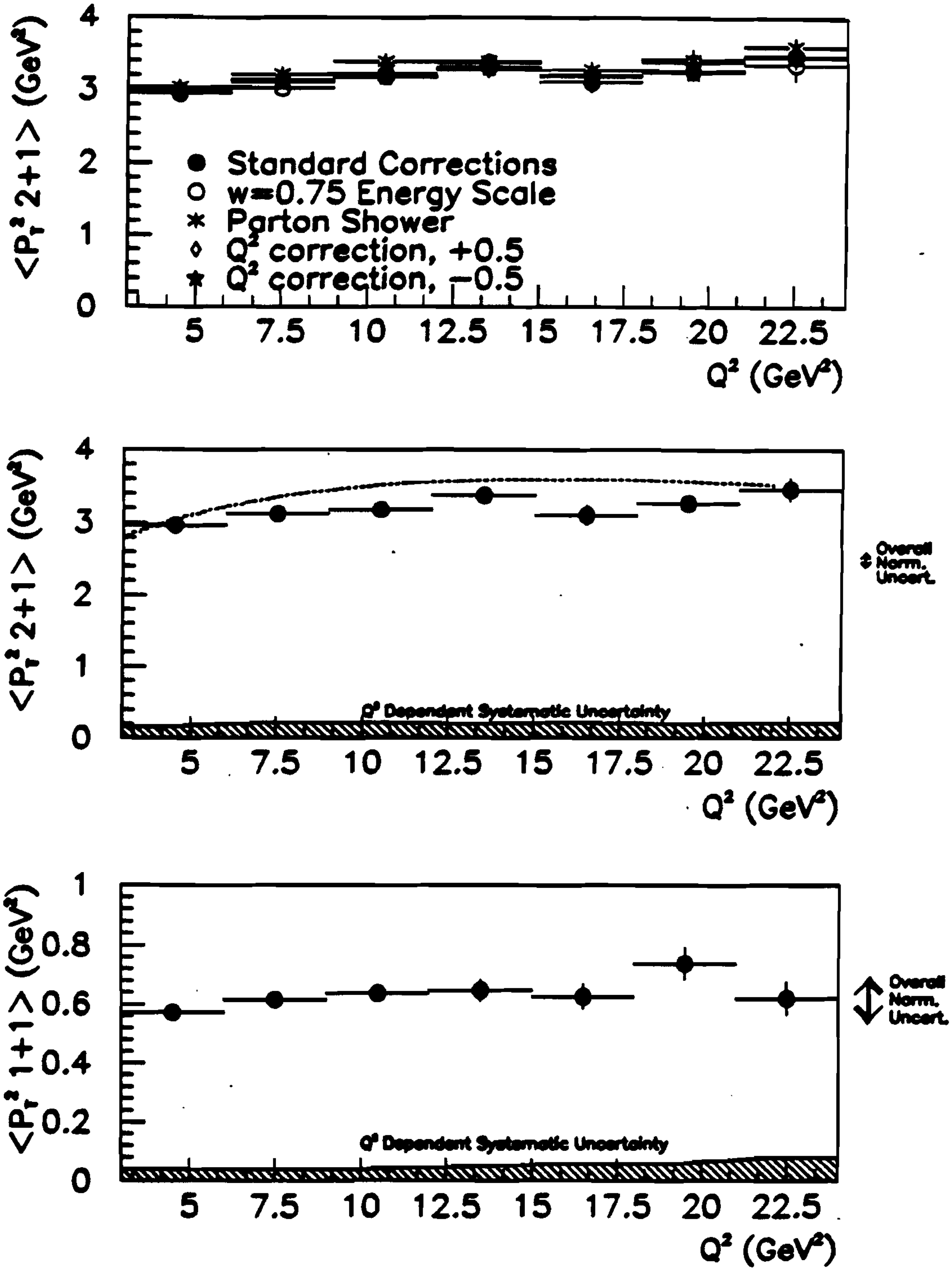

Figure 6.22. $\langle P_T^2 \rangle$ *vs.* Q^2 : **a)** For 2−1 events, the standard corrections and those used to estimate systematic uncertainty. **b)** 2−1 jet events with systematic uncertainty shown by shaded regions. The curve shows the PQCD expectation. See text. **c)** 1−1 jet events with systematic uncertainty.

The corrected 1+1 event jet transverse momentum squared is significantly smaller than for the 2+1 jet events. This is shown in figure 6.22c. The expectations for 1+1 jet events were described in section 3.3.

As discussed above and in section 3.3, $P_{T\ 2\ jet}$ is defined so as to minimize effects from sources of transverse momentum other than PQCD. Therefore, from figure 6.22, the E665 data predict that the average transverse momentum squared due to PQCD in the identified 2+1 jet events is approximately 2.8 GeV^2. It is now important to demonstrate that the squared transverse momentum from other sources is significantly smaller than this.

- *The Corrected Fragmentation and Intrinsic Transverse Momentum*

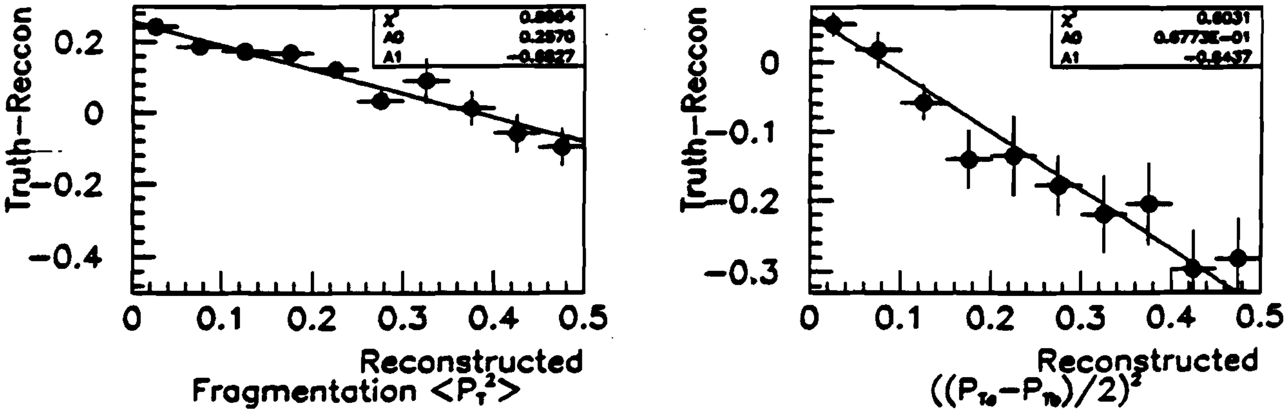

Figure 6.23. The correction functions for the fragmentation and the combined intrinsic transverse momenta.

The purpose of this section is to determine the magnitude of the non-QCD contributions to the transverse momenta.

As discussed above, the $\langle P_T^2 \rangle$ of the particles within a jet, measured with respect to the jet axis, is expected to be equal to the average squared fragmentation transverse momentum. The uncorrected distribution was shown in figure 6.9a. The acceptance correction involves migration between bins in $\langle P_{T\ frag}^2 \rangle$. The correction function used in this analysis is shown in figure 6.23a. Each $\langle P_{T\ frag}^2 \rangle_{uncor}$ is multiplied by $1.25 - 0.66\langle P_{T\ frag}^2 \rangle_{uncor}$ to obtain $\langle P_{T\ frag}^2 \rangle_{cor}$. The resulting distribution is shown in figure 6.24a. The mean is $(0.28\ GeV)^2 = 0.08\ GeV^2$. The variations in the mean value of this distribution due to acceptance corrections were 3% for chamber modelling and 7% for the physics generator and those due to spectrometer calibration were 4% for the forward spectrometer uncertainty and 1% for the beam spectrometer offset. Adding these in quadrature gives an overall measurement of

$$\langle P_T^2{}_{frag} \rangle = 0.0820 \pm 0.003(stat) \pm 0.007(sys)\ GeV^2$$

Within three sigma, this agrees with the e^+e^- data: $(0.33\ GeV)^2 = 0.11\ GeV^2$.[69] Using Monte Carlo fits, a higher value, $\langle P_T^2{}_{frag} \rangle = 0.20\ GeV^2$, has been extracted from the E665 $cos\phi$ asymmetry analysis.[12] From the histograms shown in the $cos\phi$ analysis, the error on the fragmentation transverse momentum from the fit is approximately ±0.05. Hence, within three sigma, the results agree with the analysis presented here.

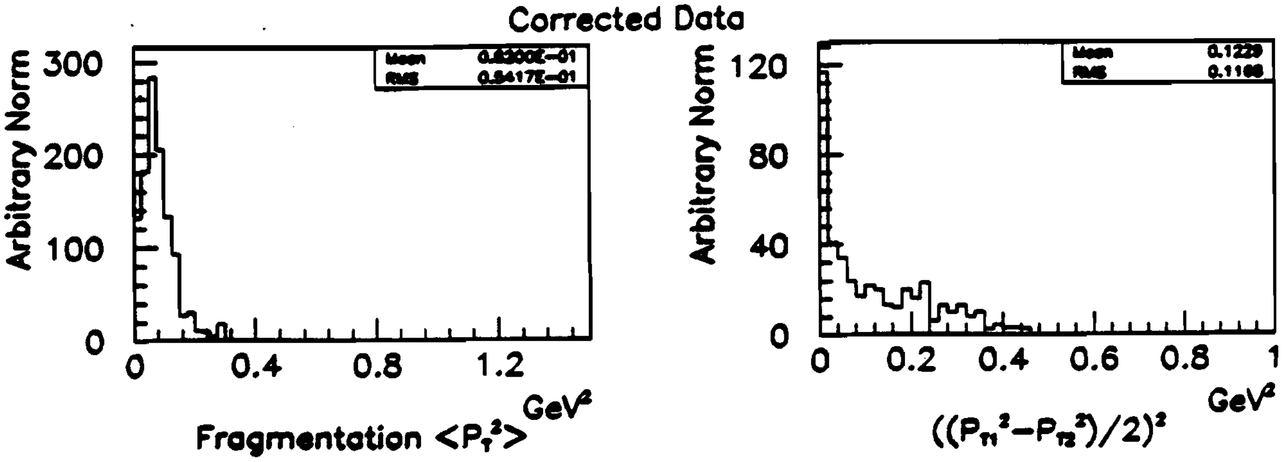

Figure 6.24. The corrected distributions for fragmentation transverse momentum and combined fragmentation and intrinsic transverse momentum.

As described in section 3.3 and above, $((P_{T\ jet\ a} - P_{T\ jet\ b})/2)^2$ is expected to be equivalent to $\frac{\pi}{4}(\langle P_T^2{}_{frag}\rangle + \langle k_T^2 \rangle)/2$. The uncorrected distribution was shown in figure 6.9b. The acceptance correction is applied in the same way as for the fragmentation case. The correction function is shown in figure 6.23b. The corrected distribution is shown in figure 6.24b. The mean is 0.123 GeV^2. The magnitudes of the uncertainties are 3%, 5% and 5% for energy scale, chamber model and physics generator, respectively, and 5% and 1% for forward spectrometer and beam magnet calibrations. Adding in quadrature this represents a total uncertainty of 9%. Solving for the average squared intrinsic transverse momentum gives:

$$\langle k_T^2 \rangle = 0.23 \pm 0.01\ (stat) \pm 0.02\ (sys)\ GeV^2.$$

This argument was based on naive assumptions about the jets, and according to the Monte Carlo study in section 3.5, $((P_{T\ jet\ a} - P_{T\ jet\ b})/2)^2$ may underestimate it the true values by up to 20%, or 0.04 GeV^2. Assuming one should make this correction, this gives:

$$\langle k_T^2 \rangle = 0.27 \pm 0.01\ (stat) \pm 0.03\ (sys)\ GeV^2.$$

This result is in agreement with the value obtained from Monte Carlo fits to the hadronic transverse momenta and $cos\phi$ asymmetry data from EMC: $(0.44\ GeV)^2 = 0.19\ GeV^2$.[69] This may also be compared to the preferred value from Monte Carlo fits to the E665 $cos\phi$ asymmetry analysis:[12] 0.16 GeV^2, with an error estimated by this author of $\pm 0.04\ GeV^2$.

In conclusion, the E665 Jet data indicate that the transverse momentum due to fragmentation and intrinsic motion within the nucleon are an order of magnitude smaller than the QCD transverse momenta. The measured values are consistent with those extracted through other methods using the same and different data sets.

6.5 Summary

In this chapter the characteristics of the uncorrected and the corrected jets were presented. Several important points demonstrated in this chapter should be noted for the final analysis presented in the next chapter.

- *Choice of* $y_{cut} = 0.04$

At $y_{cut} = 0.04$ for either value of $\tilde{w}$, there are virtually no (3+)+1 jet events in the sample and the jets are well resolved. The former is important since the theory which will be compared to the jet analysis is leading order and, therefore, has no (3+)+1 parton events. The latter means that there is little effect from "cross talk," where a particle from one jet is misassigned to the other. Cross talk would reduce the apparent transverse momentum of both jets.

- ***Indications of Parton-Jet Duality***

The α_s analysis is based on the hypothesis of parton-jet duality, that *on average* the jets reflect the behavior of the underlying partons in the event. Throughout this chapter comparisons to the parton-level expectations were made and agreement was observed. The systematic uncertainty from biases toward agreement due to the acceptance corrections were estimated.

- ***Agreement with Previous Measurements***

Measurements of $\langle P_{T\ frag}^2 \rangle = (0.29\ GeV)^2$ and $\langle k_T^2 \rangle = (0.52 GeV)^2$ were obtained through simple arguments concerning the jets. The agreement between these and the previous experimental measurements of these values indicates that, in these cases at least, the interpretations concerning the jets which are have been presented in chapter 3 appear to be meaningful.

- *Magnitude of Non-perturbative Effects*

The α_s analysis requires that the transverse momenta due to fragmentation and intrinsic momentum be small compared to the PQCD transverse momentum and that $\langle P^2_{T\ non-PQCD} \rangle \ll Q^2$. In principle, using $P_{T\ 2\ jet} = (P_{T\ jet\ a} + P_{T\ jet\ b})/2$ removes most of the contribution from intrinsic transverse momentum. Any residual effects are expected to be negligible because the combined non-PQCD effects have been measured to be an order of magnitude smaller than the PQCD transverse momentum.

Chapter 7

The Variation of the QCD Coupling Constant

This chapter follows the blueprint developed in sections 2.4 and 3.6 to study the variation of α_s with Q^2. From section 3.6

$$\langle P_{T\ all}^2 \rangle = \langle P_{T\ 2\ jet}^2 \rangle \frac{N_{2+1\ jet}}{N_{1+1\ jet} + N_{2+1\ jet}}. \tag{3.10}$$

This may be used to evaluate the equation

$$A = \frac{\langle P_{T\ all}^2 \rangle}{Q^2} \frac{2\pi F_2}{x_{Bj}} \frac{1}{\int_x f(\chi, y_{Bj}, F_2, G, \bar{p}) dx}. \tag{3.11}$$

According to the arguments presented in chapters 1-3, PQCD predicts

1. $\langle P_{T\ 2\ jet}^2 \rangle$ divided by the integral in equation 2.9 will be independent of y_{cut}.
2. A will be equal to α_s with the dependence predicted in equation 1.7.

The discussion of chapters 1—3 relied on the assumption that the nonperturbative effects were small compared to the PQCD effects and that the jet algorithm was of reasonably good quality, so that the jets reflected the character of the underlying partons. These issues were addressed in the data in chapter 6.

In order to test these predictions, in this chapter:

- $\langle P_{T\ all}^2 \rangle$ is studied as a function of y_{cut}.
- The acceptance corrected $\langle P_{T\ all}^2 \rangle$ is studied as a function of Q^2.
- A is evaluated as a function of Q^2.

Also, the y_{cut} dependence of $\langle P_{T\ all}^2 \rangle$ is used to extrapolate to $\langle P_{T\ all\ y=0}^2 \rangle$, which can then be compared to $\langle P_T \rangle$ as a cross-check of the first technique.

The data will be compared to the calculations presented in chapter 2. These calculations are evaluated directly, *not* through the Monte Carlo. These calculations require F_2, xG and R as inputs, discussed in sections 1.8 and 2.2. The Morfin-Tung B2 NLO DIS-scheme parton distributions[42] are used. Therefore, if A is equivalent to α_s, then $\Lambda = \Lambda_{DIS}$ is the PQCD scale.

Documentation of this analysis is available in reference 118.

7.1 Dependence of the Data on the Jet Parameter

In this section, the dependence of $\langle P_{T\ all}^2 \rangle$ on $y_{cut_{jet}}$ and the uncertainty associated with assuming $y_{cut_{jet}} = y_{cut_{parton}}$ are examined. The data presented in chapter 6 showed agreement with calculations assuming $y_{cut_{jet}} = y_{cut_{parton}}$. Recalling the discussion in section 3.5, the Monte Carlo Truth favored $y_{cut_{jet}} - 0.01 = y_{cut_{parton}}$. In this section, it will be shown that agreement can be achieved for $y_{cut_{jet}} \pm 0.01 = y_{cut_{parton}}$, if the parton distributions are varied. The data were divided into Q^2 bins for use in the $\langle P_{T\ all\ y=0}^2 \rangle$ cross-check in section 7.5. This section will consider only $3 < Q^2 \leq 6\ GeV^2$, but the conclusions have been found to be applicable for all Q^2 bins in this analysis, within statistical errors.

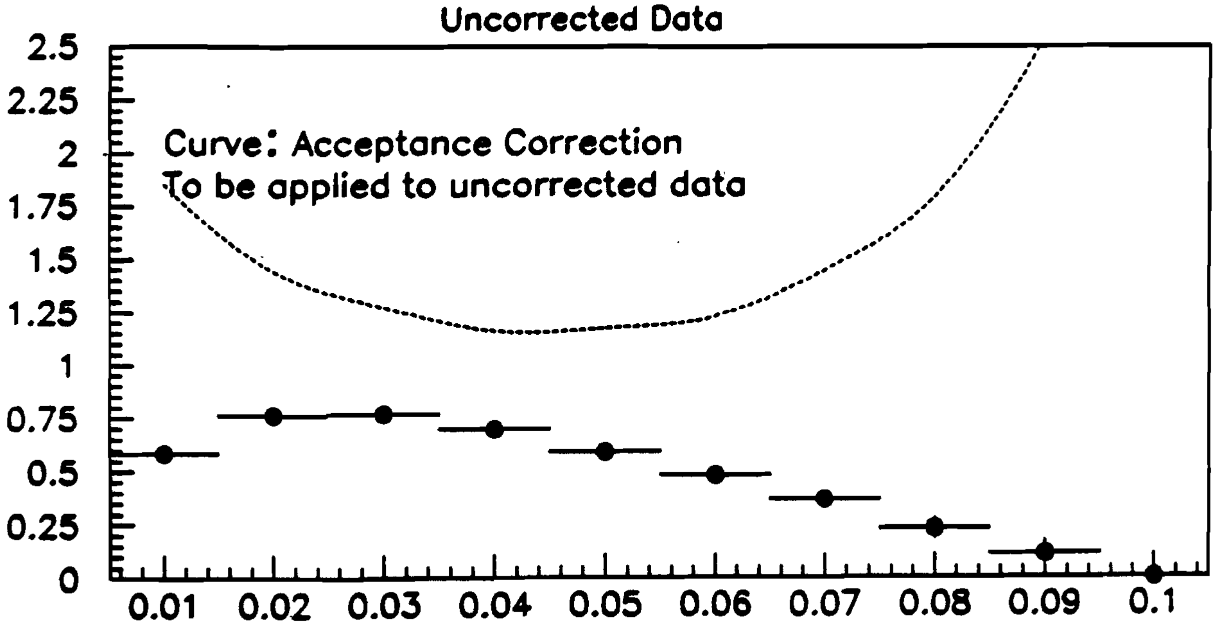

Figure 7.1. The data points show the uncorrected distribution for $\langle P_{T all}^2 \rangle$ as a function of y_{cut}. The curve shows the bin-by-bin acceptance correction which will be applied to the uncorrected data.

Figure 7.1 shows $\langle P_{T\ all}^2 \rangle$ for the uncorrected data as a function of y_{cut} for $\bar{w} = 0.5W$. $\langle P_{T\ all}^2 \rangle$ is evaluated in the following way: for every 1+1 jet event, 0 GeV^2 was added to the total, while for every 2+1 jet event $P_{T\ 2\ jet}^2$ was added; the resulting sum was divided by the total number of events; *ie,*

$$\langle P_{T\ all}^2\rangle = \frac{1}{N_{1+1}+N_{2+1}}\sum P_{T\ 2\ jet}^2 + (P_{T\ 1\ jet}^2 \equiv 0).$$

Note that for $y_{cut} < 0.03$, events with (3+)+1 jets were identified, but these do not contribute to $\langle P_{T\ all}^2\rangle$. The acceptance correction is applied bin-by-bin to this distribution, and is shown by the curve on figure 7.1.

Both plots in figure 7.2 show the corrected data point. The variation with y_{cut} is expected to be given by equation 2.9:

$$\langle \bar{P}_T^2\rangle = \frac{\alpha_s(Q^2)}{2\pi}\frac{Q^2 x_{Bj}}{F_2(x_{Bj},Q^2)}\frac{1-y+y^2/2}{1-y+y^2/2(1+R_{QCD})}$$
$$\int_{y_{cut}+x_{Bj}}^{1-2(1-x)y_{cut}} f(\chi, y_{Bj}, F_2(\chi,Q^2), G(\chi,Q^2), \bar{p}(\frac{x_{Bj}}{\chi}, y_{cut}))dx.$$

The central curve on both plots shows equation 2.9 evaluated with the Morfin-Tung B2 parton distributions (see sections 2.2-2.3) and with Λ in α_s varied to obtain the best agreement at $y_{cut} = 0.04$. The resulting curve agrees well with the data over the range $0.02 < y_{cut} < 0.09$. This indicates that the data is described by the y_{cut} dependence of equation 2.9.

Figure 7.2a shows equation 2.9 evaluated assuming $y_{cut_{jet}} - 0.01 = y_{cut_{parton}}$ by the upper curve and $y_{cut_{jet}} + 0.01 = y_{cut_{parton}}$ by the lower curve, with the same choices for α_s and the parton distributions as the central curve. The discrepancy between the calculation and the data is approximately ±10%. However, if the parton distributions are varied within the uncertainties determined in section 2.2, then better agreement for $y_{cut_{jet}} \pm 0.01 = y_{cut_{parton}}$ can be obtained, as shown in figure 7.2b. The discrepancy in figure 7.2b between the data and the curves is approximately ±5%. The functional value for α_s can then be varied by changing Λ to make the $y_{cut_{jet}} \pm 0.01 = y_{cut_{parton}}$ curves agree with the data. In conclusion, when evaluating α_s using equation 2.9, with the uncertainty in the structure functions considered separately, a 5% uncertainty must be included for the unknown correspondence between $y_{cut_{jet}}$ and $y_{cut_{parton}}$.

7.2 Study of the Acceptance Correction to $\langle P_{T\,All}^2\rangle$

$\langle P_{T\ all}^2\rangle$, defined at $y_{cut} = 0.04$ with $\bar{w} = 0.5W$, was corrected using the standard technique discussed in chapter 6. This choice of $\bar{w}$ represents a shallow minimum in the magnitude of the acceptance correction. This is equivalent to the saying that $y_{cut} = 0.04$ is approximately the minimum in figure 7.1. Defining

$$y_{ij}^{recon} = a^2 y_{ij}^{jet} \tag{7.1}$$

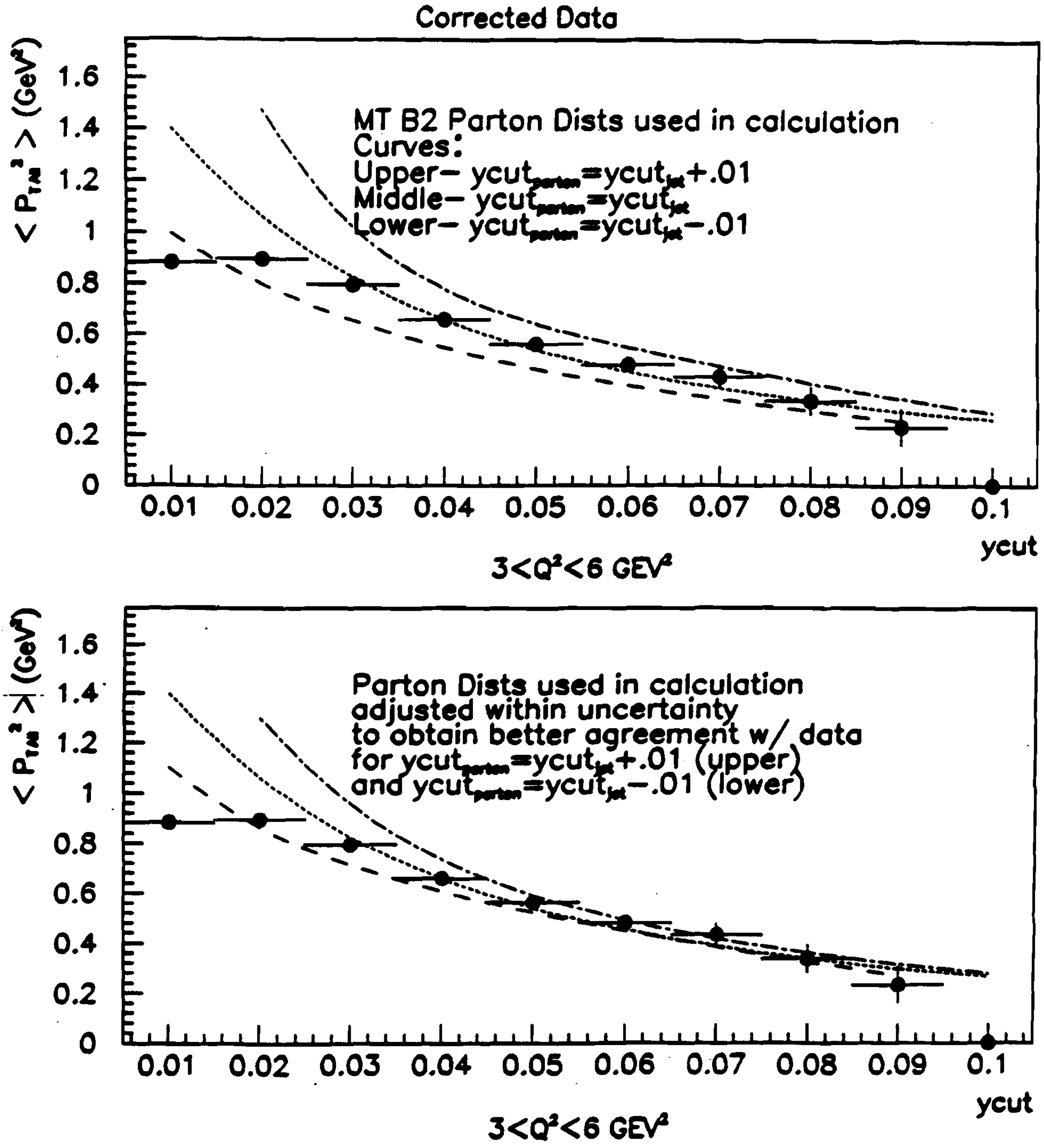

Figure 7.2. The data on both plots show the corrected $\langle P^2_{T\,All} \rangle$ as a function of y_{cut}. The central curve on both plots is from evaluation of equation 2.9 as a function of y_{cut}. The value of α_s was varied to obtain the best agreement for the $y_{cut\,jet} = y_{cut\,parton}$ (center) curve. **a)** The upper and lower curves show the calculated values if $y_{cut\,jet} \pm 0.01 = y_{cut\,parton}$. **b)** The upper and lower curves show the calculated values if $y_{cut\,jet} \pm 0.01 = y_{cut\,parton}$ and the structure functions are varied within the allowed uncertainties (see section 2.3) to obtain best agreement with the data.

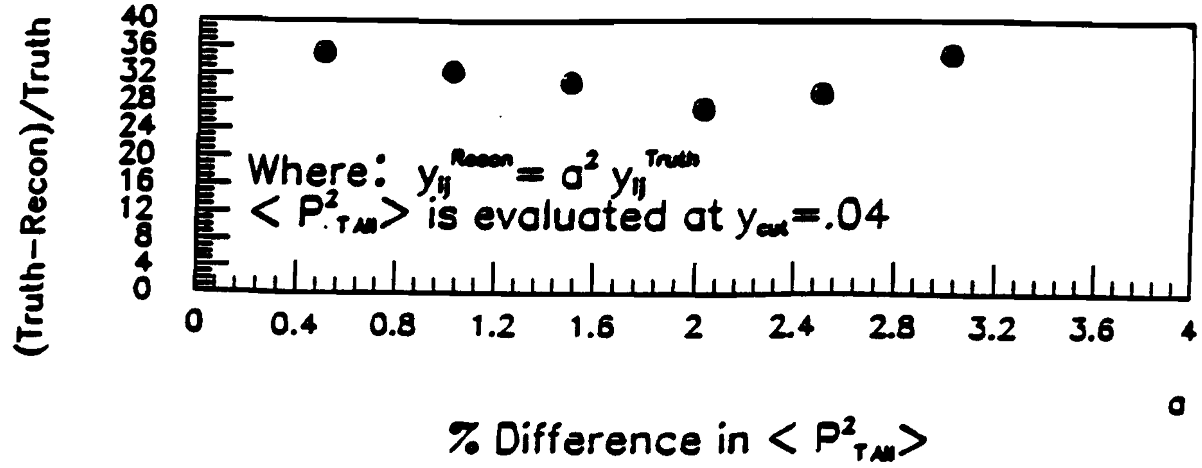

Figure 7.3. Using $a^2 y_{ij}^{Truth}$ to define jets, the percentage difference between $\langle P^2_{T All} \rangle$ in reconstructed data and truth at $y_{cut} = 0.04$ as a function of a.

is equivalent to considering $\tilde{w} = (1/a)W$, as discussed in section 6.2. Using $y_{cut} = 0.04$, varying a in the Monte Carlo Reconstructed data, and comparing to $\langle P^2_{T\ all} \rangle$ in Truth indicated that the magnitude of the correction was not strongly dependent on a, but that $a = 2$ gave the minimum correction. Figure 7.3a shows the variation of the percentage difference between Truth and Reconstructed Monte Carlo for $\langle P^2_{T\ all} \rangle$ at $y_{cut} = 0.04$ as a function of a.

The shape of the function shown in figure 7.3a can be explained by recalling that at small a, many events are found to be 1+1 jet, but the 2+1 jet events which remain have high transverse momentum, while at large a, a high percentage of events are found to be 2+1 jet, but most of these events have transverse momenta with small magnitudes. Thus extreme values of a result in similar values for $\langle P^2_{T\ all} \rangle$.

Figure 7.4 shows the C function for $\langle P^2_{T\ all} \rangle$ as a function of Q^2 for $y_{cut} = 0.04$ and $\tilde{w} = 0.5W$. The straight-line fit has slope $P1$ and offset $P0$.

Of the sources of uncertainty to C, discussed in chapter 6, the contribution of most concern is from the choice of physics generator. Residual effects from the physics generator in the acceptance correction could bias the data toward the PQCD result. The Parton Shower generator was used as an alternative to the Matrix Element generator in order to test for this systematic effect. Corrected data using the parton shower generator were fit to line and the deviation of the fit from the "standard" data points was taken to to be the systematic uncertainty. The percentage difference beyond the one sigma statistical errors, which are included as a separate systematic error, was regarded as the uncertainty due to the physics generator. The effect varied from -3% at $Q^2 = 3\ GeV^{-2}$ to 6% at $Q^2 = 24\ GeV^{-2}$, with the parton shower model giving the larger slope.

The other sources of systematic uncertainty discussed in chapter 6 were also considered. For the Q^2 dependent studies, the maximum observed deviations were: statistical error on linear fit to acceptance correction: ~ 3%; energy scale: ~ 1%; chamber model:

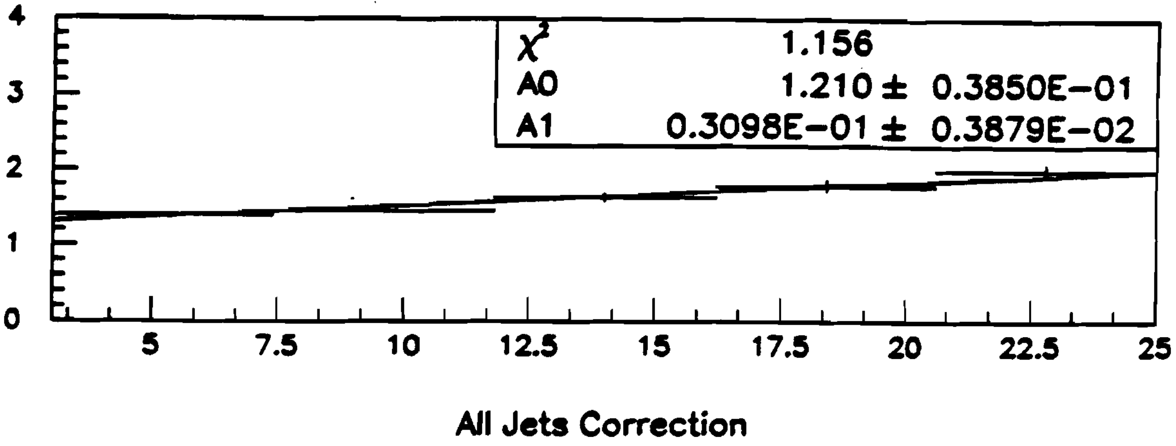

Figure 7.4. The Standard acceptance corrections to $\langle P_{TAll}\rangle$.

$\sim$ 1%; and Q^2 and x_{Bj} bin migrations: $\sim$ 2%. It should be noted that these overall uncertainties are slightly lower than the uncertainty associated with the rates and transverse momentum evaluated individually. This is because the systematic shifts of the two components tend to be in opposite directions, and therefore compensate when $\langle P_T^2{}_{all}\rangle$ is evaluated. The overall normalization uncertainties are due to forward spectrometer magnetic field (4%) and a possible beam momentum offset (1%). The uncertainties with Q^2 dependence, added in quadrature, are shown along the bottom of the plot. The normalization uncertainties (all data points multiplied by same value), added in quadrature, will be indicated by the magnitude of the double-arrow to the right of the plot.

7.3 The Variation $\langle P_{TAll}^2\rangle$ with Q^2

The corrected $\langle P_T^2{}_{all}\rangle$ is shown as a function of Q^2 in figure 7.5. The theoretical expectation for $\Lambda = 400\ MeV$ is shown by the solid curve. If α_s did not run, an expected value would be 0.135, the average of the AMY and LEP values, as discussed in chapter 2. The dotted line shows the $\alpha_s = 0.135$ expectation. A second possibility is to choose α_s constant and equal to a typical value predicted by PQCD in the Q^2 range of this analysis: 0.27. This is shown by the dashed line in figure 6.22. As discussed in section 2.2

Q^2 (GeV^2)	$<P^2_{T\,All}>$ (GeV^2)	Stat Error (GeV^2)	Sys Error (GeV^2)
4	0.701	0.018	0.072
7	0.887	0.035	0.069
10	0.924	0.047	0.054
13	0.983	0.064	0.051
16	1.050	0.080	0.059
19	1.167	0.094	0.075
21	1.376	0.118	0.084

Overall Normalization Uncertainty: 4%

Table 7.1. Table of values for $\langle P_{T\ all}^2 \rangle$

there is a 7% normalization uncertainty on the theoretical curves from the uncertainties in the parton distributions. However, the Q^2 dependence of this "PDF" uncertainty is negligible. The $\langle P_{T\ all}^2 \rangle$ corrected distribution clearly favors the assumption that α_s runs according to PQCD expectations. The values of the data points, the statistical errors, and the systematic uncertainties, are given in table 7.1.

7.4 The Varying Coupling Constant

Before evaluating equation 3.11, the sources of systematic uncertainty and its expression on the plots must be reviewed. The uncertainties fall into three categories: those related to the experimental measurement; those related to the application of the formalism of sections 2.4 and 3.5; and those related to dropping terms proportional to α_s^2 (see section 2.5). These have two types: the Q^2 dependent and overall normalization. Table 7.2 provides a list of the systematic uncertainties. For the plot of A shown below, the Q^2 dependent sources from all three categories are added in quadrature point-by-point.

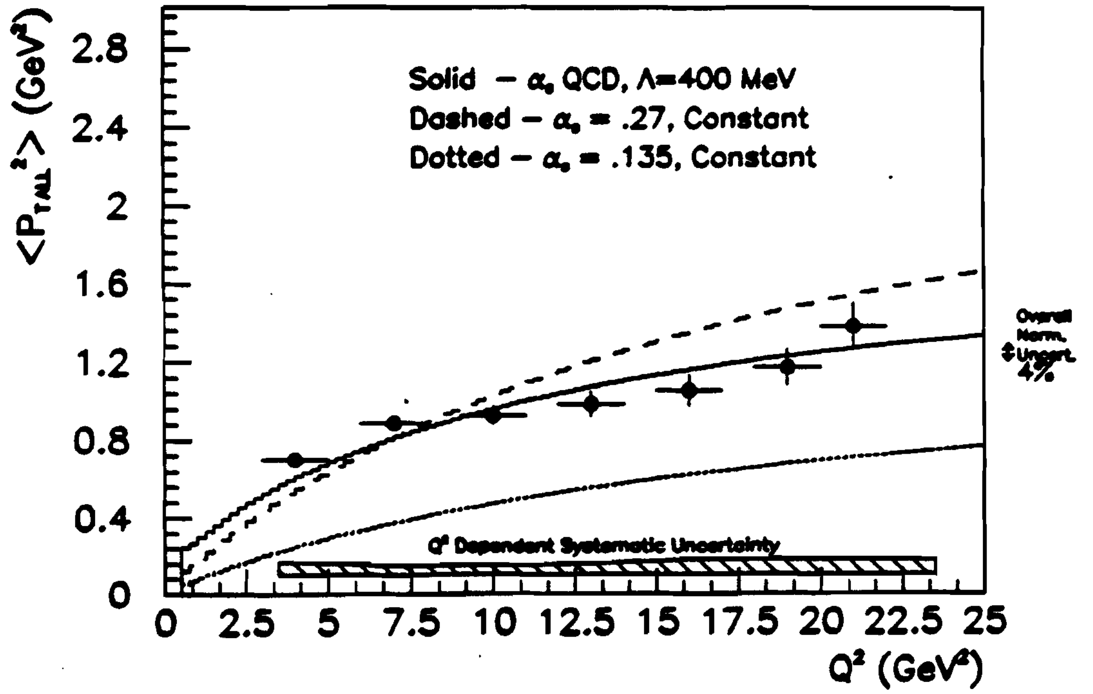

Figure 7.5. The acceptance corrected $\langle P^2_{T\,All} \rangle$ distributions. Solid line shows the theoretical evaluation with parton distributions in the DIS scheme, and α_s with 4 flavors and $\Lambda = 400\ MeV$. Dotted line shows the theoretical expectation if α_s is constant and equal to 0.135, the AMY/LEP average. Dashed line shows α_s constant and equal to 0.27.

These are shown by the shaded region at the bottom of the plot. The overall normalization uncertainties from all three categories are added in quadrature and are shown at the right side of the plot.

The evaluation of

$$A = \frac{\langle P^2_{T\ 2\ jet} \rangle}{Q^2} \frac{2\pi F_2}{x_{Bj}} \frac{1}{\int_x f(\chi, y_{Bj}, F_2, G, \bar{p}) dx} \tag{3.11}$$

is shown in figure 7.6. The shape of the data is consistent with the PQCD expectation for the variation of α_s. A best fit to the data with the form of equation 1.7, with only the statistical errors on the data considered, is given by $\Lambda = 359 \pm 31$ (*stat*) MeV, with $\chi^2 = 1.31$ for 6 degrees or freedom, or $\chi^2_{prob} = 97\%$. Changing the normalization by 20%

Systematic uncertainty (category) exp = from experimental measurement app = from application of theory ord = from order of calculation	Type	Magnitude (Range if Q2 dependent)	Chap & Sect
Error on Fit to Correction (exp)	Q2 dependent	0-3%	7.2
Physics Generator (exp)	Q2 dependent	0-6%	7.2
Chamber Model (exp)	Q2 dependent	0-1%	7.2
Energy Scale (exp)	Q2 dependent	0-1%	7.2
Bin Migration (Q^2 and x_{BJ}) (exp)	Q2 dependent	0-2%	7.2
Spectrometer Magnet Calibration (exp)	normalization	4%	7.2
Beam Momentum Offset	normalization	1%	7.2
Structure Functions (app)	negligible Q2 dependence	7%	2.2
"Massless Jets" (app)	normalization	7%	3.5
y_{cut} dependences (app)	normalization	5%	7.1
Dropping the α_s^2 terms (ord) (independent+dependent term)	normal + Q2 dependent	3.7% + 0-.3%	2.3

Table 7.2. Uncertainties in α_s analysis

changes the best value of Λ to 508 MeV. Therefore the E665 data indicate:

$$\Lambda_{DIS}^{n_f=4} = 359 \pm 31\,(stat) \pm 149\,(sys)\ MeV$$

Note: this measurement may have a large theoretical error due to the higher order corrections!. The curve on figure 7.6 shows α_s evaluated with $\Lambda_{DIS}^{n_f=4} = 359\ MeV$. This is a higher value than $\Lambda_{DIS}^{n_f=4}$ from the Morfin-Tung 1990 analysis of deep inelastic scattering and Drell-Yan data: 191 MeV.[42] A fit using only the statistical error requiring α_s to be constant found the best choice to be 0.267, with $\chi^2_{prob} = 0.4\%$. Fits made when the statistical and systematic errors were added in quadrature found the χ^2_{prob} to be 24.3% for a flat distribution and 99.6% for the QCD form.

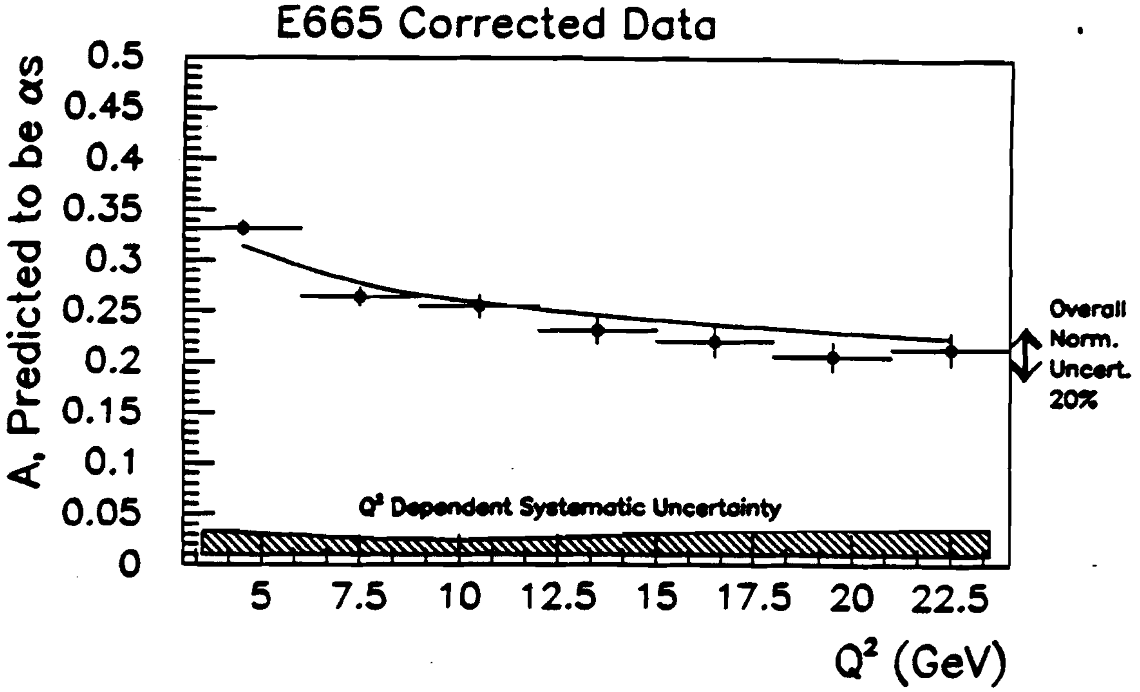

Figure 7.6. The evaluation of A, which is expected to be equal to α_s^{Lo}. Statistical errors are shown on the points. The shaded regions indicates the systematic uncertainties as described in the text. Curve shows the best-fitting PQCD α_s.

In conclusion, the data from jet production at Experiment 665 strongly support the PQCD prediction of the variation of α_s with Q^2.

7.5 A Cross-Check: Evaluating $\langle {P_{T\,All}}^2{}_{y=0} \rangle$

In this section, the second technique for obtaining α_s from the jet transverse momenta is applied. The results presented here are the first application of a technique which is still under development.[54] Because of the limitations of the data, the jet algorithm and the theoretical calculation, this method is used only as a cross-check of the results presented above.

In this method, the y_{cut} dependence of $\langle P_T^2{}_{all} \rangle$ is used to extrapolate to $\langle P_T^2{}_{all\ y=0} \rangle$, which should be equivalent to equation 2.4, if the higher order contributions are small.

Considered in bins in Q^2, the experimental analogy to equation 2.4 is obtained. The data can be used to determine the form of the fit which should be extrapolated to $y_{cut} = 0$, thus reducing the uncertainty due to y_{cut} dependence in the result.

The conclusions which can be drawn from this technique are limited by statistical errors in the E665 Run87 data set. This method requires high statistics over a wide range of y_{cut} values in order to extrapolate to $y_{cut} = 0$ with statistical significance. Even at low Q^2 values in the E665 Run87 data, there are low statistics for 2+1 jet events beyond $y_{cut} = 0.09$. For example, for $3 < Q^2 \leq 6\ GeV^2$ there are only $\sim$ 100 2+1 jet events in the $y_{cut} = 0.09$ bin. Figure 7.7 shows the distributions in four Q^2 bins. The fit shown in the figure is given by: $(P1 - P2y_{cut} + P3y_{cut}^2)e^{-P4y_{cut}}$, a general form which was found to fit the data and equation 2.9well (see section 2.4). Hence, $P1 = \langle P_{T\ all\ y=0}^2 \rangle$. The fit is applied to $y_{cut} \geq 0.03$, where there is negligible contribution from (3+)+1 jet events. For $Q^2 > 15\ GeV^2$ bins, the χ^2 of the fits becomes very small because of the large statistical errors.

Furthermore, a jet algorithm which better represents the underlying partons at lower values than $y_{cut} = 0.03$, assuring the proper extrapolation to $y_{cut} = 0$, is desirable. A possible algorithm which is under study by members of the E665 Collaboration is a variation on the JADE Algorithm, called the "k$_T$ algorithm," by Catani, Dokshitzer and Webber.[31] However, any algorithm will be strongly affected by fragmentation at very low values of y_{cut}. The standard JADE algorithm applied thoughout this analysis is applied to the data presented in this section.

The higher order corrections to $\langle P_{T\ all}^2 \rangle$ are not known as a function of y_{cut}. Because the higher order corrections to the cross section may be increasing rapidly as $y_{cut} \rightarrow 0$, the corrections to $\langle P_{T\ all}^2 \rangle$ may also be increasing steeply. Because these fits rely heavily on the $y_{cut} = 0.03$ data point, for which the higher order correction is unknown, the results should be regarded skeptically.

$P1 = \langle P_{T\ all\ y=0}^2 \rangle$ is shown for the first four Q^2 bins in figure 7.8. The curve shows equation 2.4 evaluated at $\Lambda = 400\ MeV^2$. The statistical errors on the points are the statistical error on parameter $P1$ from the fit. The systematic error associated with the data shown in figure 7.8 has not been calculated. The higher order corrections are unknown. However, the agreement with the theoretical prediction from equation 2.4 supports the results of the previous two sections.

7.6 Future Improvements to this Analysis

Because this is the first application of this analysis technique to deep inelastic scattering, it is worthwhile to consider future expectations and possible improvements for this analysis. Future analyses could be pursued using the E665 Run90 and Run91 data sets and the HERA data set. The E665 Run90-91 data set is over an order of magnitude larger

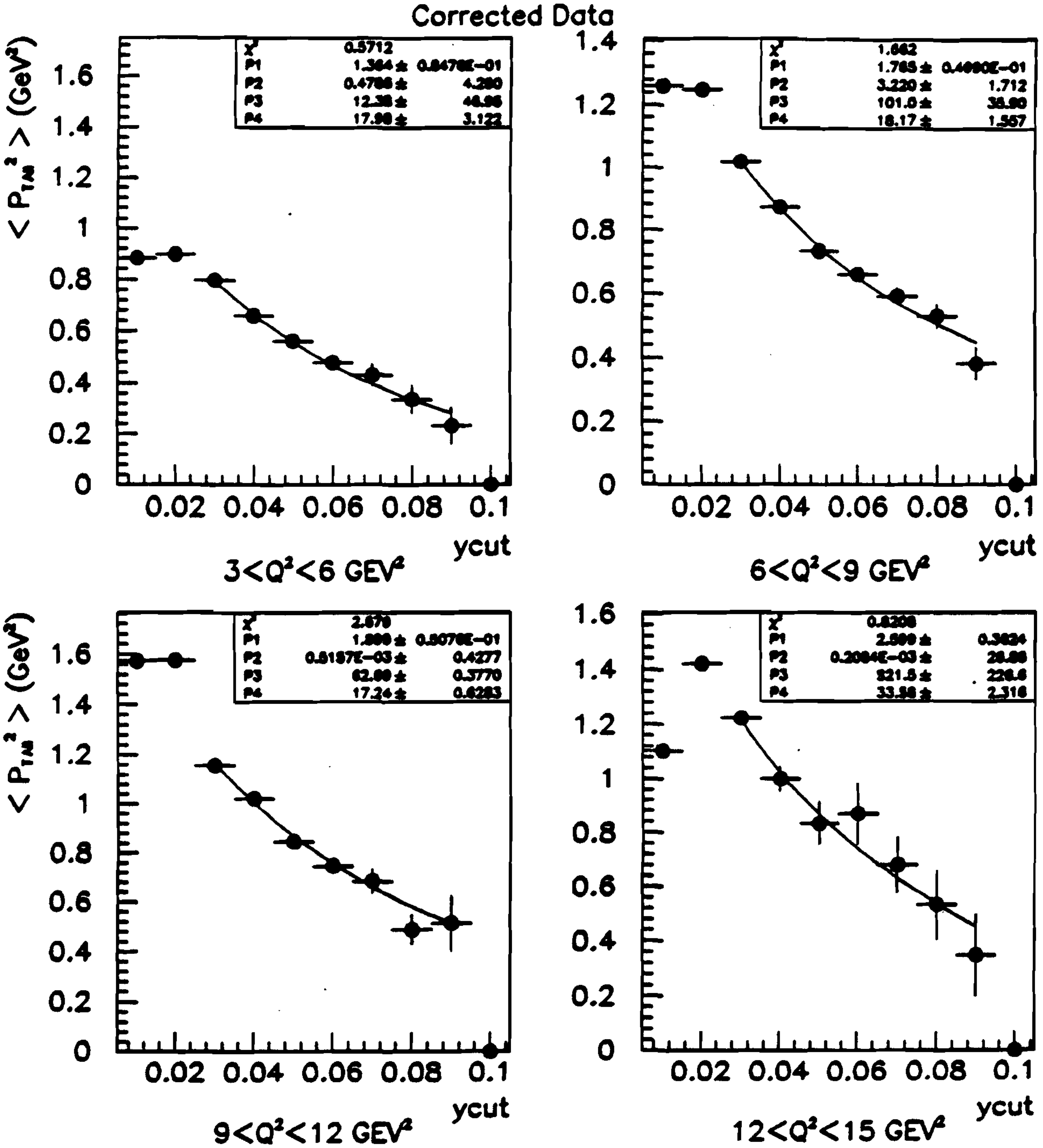

Figure 7.7. Corrected $\langle {P_{Tall}}^2 \rangle$ as a function of y_{cut} in four Q^2 bins.

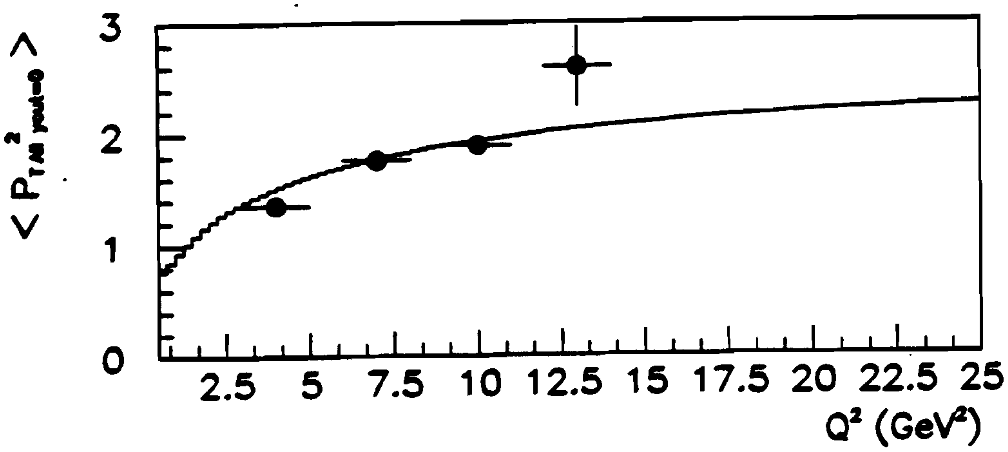

Figure 7.8. $\langle {P_{T_{all_{y=0}}}}^2 \rangle$ as a function of Q^2. The curve shows equation 2.4, evaluated for $\Lambda = 400\ MeV$.

than the Run87 data sample. The HERA experiments expect very high statistics over a much larger Q^2 range than is available to E665. Reduction of the errors listed in table 7.2 are considered in detail.

The most important problem is the lack of a complete calculation of the higher order corrections. Although these have been estimated to be small, this was based on an incomplete calculation and on an imprecise method for extracting the value. The complete calculation is necessary in order to extract a precise value of Λ. Several theoreticians have expressed interest in performing these calculations, but it is unclear when they will be available for use. Any future analysis should use these calculations.

Further development of the extrapolation technique may reduce the uncertainty due to jet-parton y_{cut} correspondence. The E665 Run90-91 data set should have sufficient statistics for application of this method over a broader range of Q^2 values. The higher order corrections may be available. Also, an improved jet algorithm for application of this technique may be found.

A significant source of systematic error is due to the structure functions. In the near future, one may expect global fits to the recent data sets[121] as well as new measurements from HERA.[122] With these new results, the variation on the structure functions used to obtain this uncertainty may be regarded as generous and could possibly be reduced. In the far future, Λ may be better measured than the gluon distribution, and it is possible that this technique could be used to extract the structure functions rather than α_s.

Another large source of systematic uncertainty is from assuming "massless jets." In this analysis, the jet momentum is 7% lower on average than the jet energy. The momentum components were scaled such that the momentum and energy of the jets were equal and this full difference was assigned as the systematic error due to this assumption. The average difference between the momentum and energy of the jets decreases with increasing W. The higher statistics of the E665 Run90-91 data sets permits a higher minimum W cut in the analysis, reducing this uncertainty. For jets at much higher energies, such as those observed at HERA, the difference between the energy and the momentum of the jets will be negligible, removing this source of uncertainty.

A major concern is that the Monte Carlo acceptance corrections may bias the data towards better agreement with the parton-level calculations. In this analysis, careful study using various physics generators, chamber models, and energy scales in the Monte Carlo have been used to estimate the magnitude of this effect. However, the best solution is to use data which has better acceptance. The E665 Run90-91 data will have better acceptance in the backward x_F region, due to improvements in the detector.

The uncertainty in fits to acceptance corrections could also be improved. This includes the statistical error on the fits using the Standard Monte Carlo as well as the uncertainty from using a different physics generator in the Monte Carlo. These uncertainties were Q^2 dependent, which is especially worrisome for this analysis. Higher Monte Carlo statistics may reduce these errors.

The other systematic uncertainties described in table 7.2 are related specifically to the E665 Run87 data set. Most of these uncertainties are better understood in the Run90-91 data set.

Conclusions

This thesis reports:

- The observation of clear three-lobed (2+1 jet) event structures in deep inelastic scattering using the data from Experiment 665 at Fermilab.
- The characteristics of the 2+1 jet events, including the rate of production and the momentum distributions.

The characteristics of the jets were consistent with the predictions of PQCD. Measurements have been made of:

- The transverse momentum within the jets due to fragmentation: $\langle P_{T\ frag}^2 \rangle = 0.0820 \pm 0.002(stat) \pm 0.005(sys)\ GeV^2$.
- The intrinsic transverse momentum in the nucleon: $\langle k_T^2 \rangle = 0.27 \pm 0.01\ (stat) \pm 0.03\ (sys)\ GeV^2$.
- The average squared transverse momentum of the 2+1 jet events as a function of Q^2 (see figure 7.5).

Using the average squared transverse momentum of the jets, a variable can be obtained which PQCD predicts to be independent of the jet defining parameter and equal to α_s, the PQCD strong coupling constant. The data are consistent with the predictions. This variable can then be studied as a function of the energy scale. This thesis presents

- The first evidence from a single data set using a single analysis method for the PQCD predicted variation of α_s.
- A fit to obtain Λ gives: $\Lambda_{DIS}^{n_f=4} = 359 \pm 31\ (stat) \pm 149\ (sys)\ MeV$.

  Note that although the higher order corrections to this analysis were estimated to be approximately 4% it is possible that these are much larger.
- Adding statistical and systematic errors in quadrature, the data are consistent with α_s constant with a 24.3% confidence level and consistent with the QCD form with a 99.6% confidence level.

Evidence for the variation of α_s from previous experiments comes from a combination of processes and a combination of data sets from different accelerators for each process. To date, the most internally consistent analysis at two energy scales comes from MARK II, which uses the same analysis procedure, the study of multijet production in e^+e^- collisions, on two data sets from PEP (29 GeV) and SLC (91 GeV) using a detector which was almost the same for the two sets. A new method[124] for extracting α_s at the mass of the τ was hotly debated at the 1992 *Rencontres de Moriond.*[125,126] This method, which uses the ratio $R = \Gamma(\tau^- \rightarrow \nu_\tau + hadrons)/\Gamma(\tau^- \rightarrow \nu_\tau + e^- + \overline{\nu_e})$ in combination with the standard e^-e^- jet shape analyses (see for example reference 65), allows the LEP experiments to measure α_s at $\sim$ 3 GeV and 91 GeV, but through two different physics processes. The structure function experiments should, in principle, be able to measure the α_s variation with Q^2 through the scaling violations. However, an order of magnitude more statistics than are presently available, are needed.[127]

It is interesting to compare the E665 results with measurements of α_s from other experiments. Figure C.1 shows the recent measurements of α_s presented at the 1992 *Rencontres de Moriond.*[126] Results from deep inelastic scattering, e^+e^- and hadron collider experiments are presented. In comparing different experiments, many theoretical and experimental caveats should be borne in mind. For example, the processes and orders which contribute to each measurement vary between the experimental values shown. Furthermore, experiments of one type, for example e^-e^-, have correlated systematic errors since the data were corrected using the same Monte Carlo and theoretical calculations. Keeping these concerns in mind, note that the E665 data are compatible with a smooth transition between the measurements from other experiments at lower and higher Q^2 values.

In conclusion, the data from jet production at Experiment 665 support the PQCD prediction of the variation of α_s with Q^2.

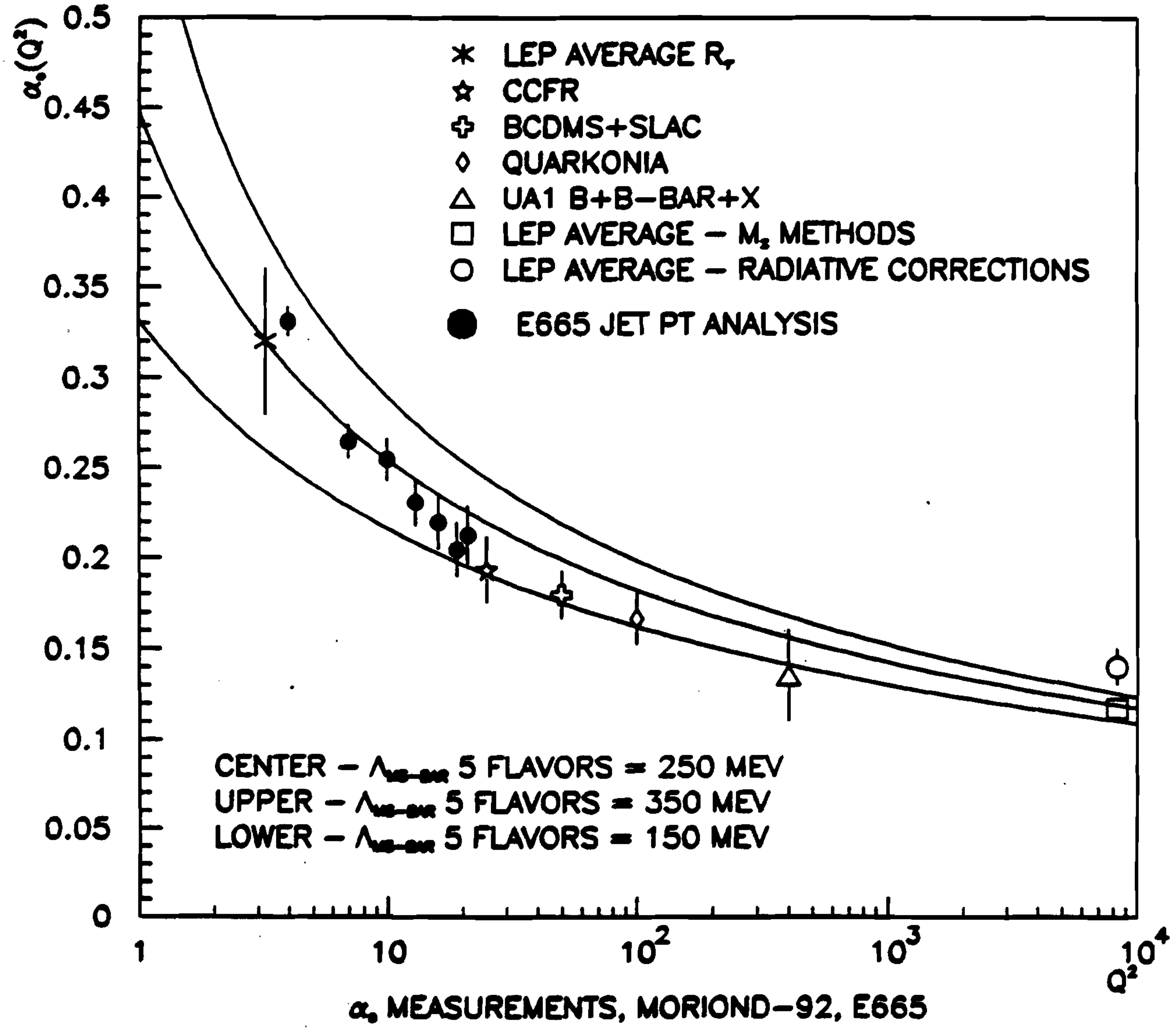

Figure C.1. E665 measurement of α_s compared to measurements of α_s from scaling violation studies (deep inelastic scattering), hadron collider experiments, and e^+e^- experiments. It is interesting to note the smooth transition between the results. There are many theoretical and experimental caveats associated with this plot! See text.

Appendix A

Definitions of Variables

Event Kinematic Variables (see section 1.1):

$p_\mu \equiv (E_\mu, \overrightarrow{p_\mu})$ The 4-vector of the incoming muon in the lab.

$p'_\mu = (E'_\mu \overrightarrow{p_\mu}')$ The 4-vector of the outgoing muons in the lab.

$T \equiv (M, \overrightarrow{0})$ The 4-vector of the target nucleon in the lab, where M is the mass of the nucleon.

$q \equiv (\nu, \overrightarrow{q})$ The 4-vector of the virtual photon in the lab.

$$\overrightarrow{q} = \overrightarrow{p_\mu} - \overrightarrow{p'_\mu}.$$

$$\nu = E - E' = (q \cdot T)/M.$$

$\overrightarrow{q}$ The three vector of the virtual photon in the lab:

Q^2 The negative square 4-momentum of the virtual photon:

$x_{Bj} = Q^2/2M\nu = (q \cdot q)/(2q \cdot T)$.

$W^2 = 2M\nu - Q^2 + M^2 = Q^2(1 - x_{Bj})/x_{Bj}$.

$y = \nu/E_\mu$

Parton-level Kinematic Variables (see section 1.3):

k the incident parton 4-vector.

p, r the 4-vectors of the outgoing partons.

θ_p, θ_r the angles between the outgoing partons and the axis formed by $\overrightarrow{q}$.

$u = k \cdot p/k \cdot (q + k) = k \cdot p/k \cdot q$

χ the fraction of the proton momentum carried by the incoming parton.

$z = q \cdot q/2q \cdot k = x_{Bj}/\chi$.

Transverse Momenta (see sections 1.3, 3.3, introduction to chapter 5:

NOTE An arrow (→) over any of the quantities below indicates the vector, while the absense of an arrow indicates the magnitude of the vector.

P_T^2	$= Q^2\frac{(1-z)}{z}u(1-u)$, transverse momentum of the parton measured with respect to *the virtual photon axis.*
$P_{T\ pcl}$	The transverse momentum of the particles in the jet with respect to *the jet axis.*
$P_{T\ jet\ i}$	For the $i-th$ jet, the transverse momentum measured from *the virtual photon axis* to the jet vector.
$P_{T\ frag}$	The transverse momentum introduced by fragmentation processes.
k_T	The intrinsic transverse momentum due to fermi motion of the quarks, measured with respect to *the virtual photon axis.*
$P_{T\ QCD}$	The transverse momentum with respect to *the virtual photon axis* of the partons due to the QCD process (photon-gluon fusion or gluon bremsstrahlung). It applies at the parton level to events which have k_T also.
$P_{T\ crosstalk}$	The transverse momentum with respect to *the virtual photon axis* introduced by misassigning particles between the jets.
$P_{T\ 2\ jet}$	$\frac{(P_{T\ jet\ a}+P_{T\ jet\ b})}{2} \approx P_{T\ QCD}$, measured with respect to *the virtual photon axis.*
$P_{T\ 1\ jet}$	Transverse momentum of the identified 1+1 jet events, measured with respect to *the virtual photon axis.*
p_T	Transverse momentum of the particles in an event measured with respect to *the virtual photon axis.*

Structure Functions and Parton Distributions (see sections 1.2, 1.8, 2.3):

F_L,F_2	The structure functions.
R	$= F_L/(F_2 - F_L)$, the ratio of longitudinal to transverse cross sections.
R_{QCD}	R defined in NLO QCD.
R_{SLAC}	The experimentally measured R.
$xG(x, Q^2)$	The gluon distribution weighted by x.
$xq(x, Q^2)$	The quark distributions weighted by x.
$x\overline{q}(x, Q^2)$	The antiquark distributions weighted by x.
DIS	A renormalization scheme in which parton distributions are defined. See reference 33 for details beyond what is in chapter 2.
$\overline{MS}$	A renomalization scheme in which parton distributions are defined. See reference 35 for details beyond what is in chapter 2.

Variables Describing the Experiment (see chapter 4):

X, Y, Z	The E665 coordinate system, right-handed with X along the beam.
x_{vertex}	X position of the vertex of the event.

References

[1] . G. Hanson, *et al. Phys. Rev. Lett. 35* (1975) 1609.

[2] . D. Barber, *et al.*, *Phys. ReV. Lett. 43:12* (1979) 830.

[3] . Ch. Berger, *et al.*, *Phys. Lett. 86b:3,4* (1979) 418.

[4] . W. Bartel, *et al.*, *Phys. Lett. 91b:1* (1990) 142.

[5] . R. Brandelik, *et al.*, *Phys. Lett. 86b:2* (1979) 243.

[6] . D. Saxon, *Jet Fragmentation*, Proc of the European Physical Soc., Bari, Italy, 1985.

[7] . M. Berggren, *The Transverse Momentum of Hadrons in Deep Inelastic Neutrino Scattering*, U. of Stockholm, Sweden, 1990.

[8] . H. Georgi and H. Politzer, *Phys. Rev. Lett. 40:1* (1978) 3.

[9] . J. Ranft and G. Ranft, *Phys. Lett. 82B:1* (1979) 129.

[10] . C. Salgado, *Proceedings of the International Conference on High Energy Physics,* Dallas, 1992.

[11] . P. Stevenson, *Nucl. Phys. B150* (1979) 357.

[12] . D. Jansen *Transverse Momentum and Energy Flow of Charged Hadrons Produced in 490 GeV deep inelastic Muon scattering* U. of Washington, 1991.

[13] . D. Michael, *A Study of Transverse Momentum and Jets* Harvard University, 1990.

[14] . U. Ecker *Longitudinal and Transverse Momentum Distributions of Hadrons in the Final State of deep inelastic Muon-Nucleon scattering* Bergische Universitat Gesamthochschule Wuppertal, 1991.

[15] . M. Adams, *et al.Phys. Rev. Lett. 69:7* (1992) 1026.

[16] . F. Close, *An Introduction to Quarks & Partons* Academic Press (1979) *chapter 9.*

[17] . L. Whitlow, *deep inelastic Structure Functions from Electron scattering on Hydrogen, Deuterium and Iron* Stanford Univ. (1990)

[18] . J. Friedman, I. Kendall, *Ann Rev. Nucl. Part. Sci. 22* (1972) 203. *(review).*

[19] . E. Reya, *Phys. Rep. 69:3* (1981) 195.

[20] . J. Körner, E. Mirkes, and G. Schüler, *Int. Jou. Mod. Physics. A4* (1989) 1781.

[21] . G. Altarelli and G. Martinelli, *Phys. Lett. 76B:1* (1978) 89

[22] . C. Quigg, *Gauge Theories of the Strong, Weak and Electromagnetic Interactions*, Benjamin/Cummings Pub. Co., Inc,. (1983) *chapter 8.*

[23] . F. Halzen and A. Martin, *Quarks & Leptons* John Wiley & Sons, Inc. (1984) *chapter 7.*

[24] . P. Ramond, *Field Theory: A Modern Primer* Benjamin/Cummings Pub. Co., Inc, (1986), *chapters IV.5-IV.7.*

[25] . G. Altarelli, *Phys. Rep., 81:1* (1982) 1

[26] . A. Peterman, *Phys. Rep. 53:3* (1979) 157.

[27] . H. Georgi, H. Politzer *Phys. Rev. D9* (1974) 416.

[28] . D. Gross, F. Wilczek *Phys. Rev. D9* (1974) 980.

[29] . G. Altarelli, G. Parisi *Nucl. Phys., B126* (1977) 298.

[30] . L. Pondrom, notes from the *FNAL Academic Lecture Series*, Hadron Collider Physics, 1991

[31] . S. Catani, Yu. Dokshitzer, B. Webber, *The Kt Clustering Algorithm for Jets in deep inelastic scattering and Hadron Colliders CERN-TH*6473/92

[32] . D. Gross and F. Wilczek, Phys. Rev. Lett. 30 (1973) 1343, and H. Politzer, *ibid*, 1346.

[33] . J. Owens and W. Tung, Parton Distribution Functions *FERMILAB-PUB-92/59-T*

[34] . W. Tung, *Overview of Parton Distributions and the QCD Framework FNAL-Conf-90/172-T*, published in *Proc. of the Wkshp. on Hadron Structure Functions* Fermilab (1990) 18.

[35] . G. Altarelli, R.K. Ellis, G. Martinelli, Nucl. Phys. B157 (1979) 461.

[36] . C. Weizacker, *Z. Phys. 88* (1934) 612; E. Williams, *Phys. Rev. 45* (1934) 729.

[37] . This tabular format was first presented by C. Salgado in an unnumbered memo.

[38] . S. Mishra and F. Sciulli, *Ann. Rev. of Nucl. and Part. Sc., 39* (1989) 259.

[39] . I. Bird, *Measurement of the Nucleon Structure Functions in deep inelastic Muon scattering*, Vrije Universiteit te Amsterdam, (1992).

[40] . M. Jong, *Muoproduction of J/psi Mesons and the Gluon Distribution in Nucleons*, Vrije Universiteit te Amsterdam, 1991.

[41] . M. Werlen, *Gluon Structure Function from Direct Photon Experiments* IPNL -1989/3 (1989).

[42] . J.Morfin and W. Tung, *Z Phys. C 52*, (1991) 13.

[43] . A. Martin, R. Roberts and W. Sterling, *Parton Distributions, the Gottfried Sum Rule and the W Charge Asymmetry* DTP/90/62 (1990).

[44] . M. Gluck,E. Reya, Vogt *Z. Phys. C. 48* (1990) 471.

[45] . P. Quintas, *Measurement of Structure Functions* Columbia University (1992)

[46] . Talk given by Wuki Tung at the International Conference on High Energy Physics, Dallas, 1992. Slides are available through SSC labs and are in the E665 library.

[47] . The PDF Library is part of the CERNLIB Program Library.

[48] . M. Adams *et al*, *Measurement of the Cross section Ratio n/p in inelastic Muon-Nucleon scattering at Very Low x and Q-squared*, to be submitted to Physics Letters.

[49] . Park, *QCD Studies from Multi-jet Events Produced in Electron Positron Annihilations at Tristan*, Rutgers University, 1989

[50] . S. Bethke and S. Catani, *Moriond Conference* 1992 *taken from copy of transparencies, see E665 library*

[51] . Suggested by J. Morfin, private communication, form used in Morfin-Tung set 9, LO, Low Q^2

[52] . *see, for example,* Brodkorb, Körner, Mirkes and Schuler *Z. Phys. C* (1989) 415.

[53] . H. Schellman, *Check of Calculation of* $\langle P_T^2 \rangle$ *for resolved 3-jet events*, 3 June 1992.

[54] . This technique was first suggested by H. Melanson in October, 1992. The application is under development by members of the E665 Collaboration at this time.

[55] . D. Graudenz, *The Three Jet Cross section to Order alpha-s squared in deep inelastic Electron Proton scattering* DESY T-90-01.

[56] . D. Graudenz, N. Magnussen, *Physics at HERA, vol 1.* Hamburg (1991) 261

[57] . K. Charcula, *DESY-91-093* (1991).

[58] . As noted by C. Salgado, *QCD Analysis of Final States in Deep Inelastic Muon-Proton Scattering*, unnumbered internal memo, E665 library, α_s notebook, see p. 20.

[59] . R. Feynman, R. Field, *Nucl Phys B:136* (1978) 1.

[60] . B. Andersson, G. Gustafson, C. Peterson, *Phys. Scr. 19* (1979) 184.

[61] . P. Burrows, G. Ingelman, Ros *Jet Reconstruction and Jet Properties at HERA* Z. Phys. C39 (1988) 257.

[62] . Altarelli, *Experimental Tests of Perturbative QCD* Ann. Rev. of Nucl. and Part. Science, v39 (1989) 357.

[63] . S. Ellis, *"On Defining the Undefinable:Jets,"* Proc. of Workshop on Jet Studies, U. of Durham, 1990.

[64] . TASSO Collaboration, *Global Jet Properties at 14 GeV to 44 GeV Center-of-Mass Energies in e+e- annihilation* Z./ Phys. C47 (1990) 187.

[65] . L3 Collaboration, *Studies of Event Structure and Comparisons with QCD Models at the Z0 Resonance* CERN-PPE/92-50.

[66] . B. Flaugher, *QCD and Jets at CDF* Proc. of the 21st Int. Symp. on Multi. Dynamics, Wuhan, China, 1991.

[67] . S. Brandt, *et al*, *Z. Phys. C1* (1979) 61

[68] . M. Fleischer, *et al.*, *The Hadronic Final State in ep-scattering"* fill this in

[69] . Combined documentation of programs by M. Bengtsson, G. Ingelman, T. Sjostrand, A. Weigend *Manual for The Lund Monte Carlo for Jet Fragmentation*, Fermilab PM0050

[70] . G. Ingelman, B. Andersson, G. Gustafson, T. Sjostrand *Nucl. Phys. B206* (1982) 239.

[71] . M. Baker *Azimuthal Asymmetry and Transverse Momentum of Hadrons in deep inelastic Muon scattering at 490 GeV* M.I.T., 1992.

[72] . M. Adams *et al.*, *Phys. Lett. B279* (1991) 163.

[73] . B. Webber, *Nucl. Phys. B:238* (1984) 492.

[74] . R. Odorico, *Comput.*, *Phys. Commun. 32* (1984) 139.

[75] . M. Bengtsson, G. Ingelman, T. Sjostrand, *"Parton Cascade Evolution and Event Structure at HERA*, Proc. of the HERA Workshop, 1987

[76] . B. Andersson, G. Gustafson, G. Ingelman, T. Sjostrand *Physics Reports, 97:2,3* (1983) 31.

[77] . N. Geddes, *Properties of Jet Fragmentation in deep inelastic Muon scattering at 280 GeV* Oxford Univ. (1985)

[78] . R. Peccei and R. Ruckl, *Nucl. Physics, B162* (1980) 125.

[79] . D. Jaffe *Real Beam for the E665 Monte Carlo* E665 Internal Memo ST116

[80] . L. Mo and Y. Tsai, *Rev. Mod. Phys. 41* (1969) 205.

[81] . Melanson, *Comparisons between Lepto 5.2 and Exact* $O(\alpha_s)$ *Calculations of deep inelastic scattering Cross Sections* E665 Internal Memo

[82] . Corrected in version 6.1: G. Ingelman, *Lepto v. 6.1 - The Lund Monte Carlo for deep inelastic Lepton-Nucleon scattering* TSL/ISV-92-0065 (Uppsalla U. Preprint), *see page 7.*

[83] . Private Communication between H. Melanson, of FNAL, and the authors of reference 20.

[84] . S. Oday, *Charged Hadron Multiplicities in 490 GeV Deep Inelastic Muon Scattering* U. of Maryland (1990).

[85] . S. Rembold and the E665 Collaboration, paper circulating in draft form.

[86] . D. Hantke, slides from the summer 1992 collaboration meeting, E665 library.

[87] . The importance of using massless jets was shown to me by Prof. Marj Corcoran of Rice University.

[88] . D. Lincoln, " *On determining xbj from Jet Measurements,* ", Talk presented at the DPF Conference, Batavia, 1992.

[89] . P. Burrows, G. Ingelman, E. Ros, *Jet Reconstruction and Jet properties*, Proc. of the HERA Workshop, 1987.

[90] . From discussion with Gunnar Ingelman of Lund University

[91] . E. Ramberg *Neutral Pion and Eta Production in Deep Inelastic Muon Scattering at 480 GeV* U. of Maryland, 1989.

[92] . P. Anthony, *Bose-Einstein Correlations in Deep-Inelastic Muon Scattering,* MIT, 1990.

[93] . M. Erdmann, *Lifetime of the Coloured Proton in Muon-Proton Scattering,* University of Freiburg i.Br.,1990.

[94] . S. Magill, *Xe/D_2 Cross Section Ratio from Muon Scattering at 490 GeV/c,* University of Illinois-Chicago, 1990.

[95] . A. Röser, *Hadronmultiplizitäten in tief-inelastichen Müon-Nukleon-Streuung bei einer maximalen Schwerpunktenergie von 30 GeV* University of Wuppertal, 1991.

[96] . J. Ryan *Particle Production in Deep Inelastic Muon Scattering* M.I.T., 1991.

[97] . A. Salvarani, *Forward Hadron Production in Deep Inelastic Muon Scattering at 490 GeV from Deuterium and Xenon* U.C.S.D., 1991.

[98] . A. Bhatti, *The Ratio of the Proton and Neutron Structure Functions in 490 GeV/c Deep Inelastic Muon Scattering,* University of Washington, 1991.

[99] . M. Schmitt *Deep Inelastic Exclusive Rho Production Using 485 GeV Muons* Harvard, 1991.

[100] . S. Aïd, *Measurement of the Ratio of Neutron Cross-section to Proton Cross-section in Muon Deep Inelastic Scattering at 490 GeV/c,* University of Maryland, 1991.

[101] . Documentation of the Level 2 trigger and the overall Run90-91 Triggering systems may be found in E665 Library Memos: BT053,64,72,73,75-80,86,94.

[102] . M. Adams *et al., Nucl. Instr. Meth. A291,* (1990) 533.

[103] . S. Kunori, *Plan for LAT filter* E665 Internal Memo (1989) ST0186.

[104] . A. Bhatti, U. Ecker, D. Jansen, M. Schmitt, S. Wolbers, *The DR (Data Reduction) Program,* E665 Internal Memo (1990) SW113.

[105] . A. Malensek, J. Morfin, *The Tevatron Muon Beam,* Fermilab-TM-1193, 1983.

[106] . H. Fenker, *A Standard Beam PWC for Fermilab* TM-1179, E665 Internal Memo BT005.

[107] . H. Montgomery, *Status of Beam Tagging and Veto System* E665 Internal Memo (1985) BT011.

[108] . Albanese *et. al, Nucl. Inst. and Meth. 212* (1983) 111.

[109] . H. Venkataramania, *Particle Id at High Lum.* FNAL, 1989.

[110] . J.Conrad,*A Recommendation for a New Counter for the WAM2 Trigger,* E665 Internal Memo BT077.

[111] . H. Melanson, *Pattern Recognition Update,* E665 Internal Memo ST0114.

[112] . R. Brun, *et al., GEANT Manual* CERN-DD/EE/84-1, 1987.

[113] . H. Melanson, *"Simulating hadron showers in the E665 Calorimeter for Run 87 data,"* E665 Internal Memo, AN103.

[114] . J. Drees, *Radiative Corrections and Hadron Distributions in Deep Inelastic Scattering,* Wu-B78-16 (University of Wuppertal Pre-print) 1978.

[115] . R. Kennedy, *The Neutron to Proton Cross Section Ration at Very Low xbj* U.C.S.D., 1992.

[116] . A. Kotwal – writeup of calorimeter studies is in progress.

[117] . B. Pawlik, H. Schellman, the TRAGEN package in the UAPAM, code is self-documented.

[118] . *Alpha-s Running Measured Using Jet Pt* Binder of Internal Memos related to the thesis of J. Conrad, in the E665 Library.

[119] . H. Melanson, *Comparisons of general event characteristics between Run 87 H2 data and Lund* E665 Internal Memo AN104.

[120] . W. Loomis, *et al.Phys. Rev. D:19,9* (1979) 2543.

[121] . For example, the CTEQ collaboration will be publishing global fits to the recent data in the near future. From J. Morfin, private communication.

[122] . For example, Bernardi and Hildescheim *A Detailed Simulation of the Measurability of F_2 at HERA.* Proceedings of the Physics at Here Workshop, Hamburg (1991) 79.

[123] . S. Komamiya *et al.*, *Phys. Rev. Lett. 64* (1987) 26.

[124] . E. Braaten, S. Narison, A. Pich, *Nucl. Phys. B373* (1992) 581.

[125] . Summarized in the Slides of the Moriond Presentations on Alpha-s by Catani. Available from the conference organizers and in the E665 library.

[126] . S. Bethke and S. Catani, *Summary of Round Table Disc. at Ren. Mor.* CERN-TH-6484-92.

[127] . K. Bazizi, *et. al.*, *High Luminosity Muon Scattering at FNAL*, (Report of the DIS Muon Group at the Breckenridge Workshop), FERMILAB-CONF-90/139 (1990).